Università di Roma “La Sapienza”
Dipartimento di ingegneria dell'Informazione, Elettronica e Telecomunicazioni
(DIET)

Ph.D thesis

Giovanni GILARDI

December 2011

Lightwave planar circuits based on organic materials for filtering and sensing

First Supervisor
Professor Antonio d'ALESSANDRO

Second Supervisor
Dr. Romeo BECCHERELLI

Controtutore
Professor Renato CICCHETTI

Dottorato di ricerca XXIV ciclo

ABSTRACT

To communicate, at least three elements are necessary: the *transmitter*, the *receiver* and a *medium/channel* in which the information/communication travels from the transmitter to the receiver. In an oral communication between two persons the transmitter is "*who speaks*", the receiver is "*who listens*" while *air* is the communication channel. In an optical communication system, the transmitter is in general represented by a laser while the receiver is a photodetector made by proper materials that properly absorb light and convert it in electronic signals. There are several considerations to improve the communication channel. If we consider, for example, a long distance optical communication system, the optical fiber is the best candidate to link the transmitter and the receiver. With regarding integrated optics the transmitter, the receiver and the channel are ideally integrated on the same substrate. In any case the transmitted information needs to be elaborated so that the receiver collects just the data of interest. Typical elaboration blocks are amplifiers, modulators, switches, multiplexers, demultiplexers and filters.

This thesis investigates in detail optical filters based on two phenomena and their applicability in photonics devices.

The first phenomenon is called *Whispering gallery modes*. In 1912, Lord Rayleigh published *The problem of the whispering gallery* in which he demonstrated the very efficient propagation of acoustic waves along the internal surface of the dome of St. Paul's Cathedral in London. The characteristic wavelength of the acoustic wave is in the order of *meters* and also the diameter of the cap is in the order of *meters*. Let us imagine a "compression" of 10^6 to both wavelength of the acoustic wave and cap. In that case we can consider *light* instead of *acoustic wave* and a dielectric *microresonator* instead of the spherical cap. Whispering gallery modes resonators are based on the principle of total internal reflection. The elevate spatial confinement of the whispering gallery modes renders such a device of great interest for possible applications in various fields of photonic. They are mainly investigated to develop optical filters and chemical or optofluidic sensors. One aim of this thesis is to introduce a novel mechanism to obtain the tuning of the spectral response introducing *liquid crystals* as tuning medium.

The second phenomenon investigated in this thesis is the Braggs's law, to develop optical filters. Bragg diffraction occurs when an electromagnetic radiation hits a periodic structure and it is scattered to achieve a constructive interference in accordance to Bragg's law. For a periodic solid structure, with period d the scattered waves interfere constructively, they remain in phase since the path length of each wave is equal to an integer multiple of the wavelength. The path difference between two waves undergoing constructive interference is given by $2d\sin\vartheta$ where ϑ is the scattering angle. This leads to Bragg's law, which describes the condition for constructive interference from successive planes of crystalline lattice $2d\sin\vartheta = n\lambda$ where n is an integer and λ is the wavelength. In particular we investigate Bragg's law to develop all-optical Bragg's filter. In order to do that, we consider mixtures of liquid crystals and azo-compounds, able to modify their shape and optical properties if stimulated with a pump light with proper wavelength and power.

Chapter 1 outlines the basic integrated optical filter based on resonant structures and periodic structures. It analyzes the materials adopted, the geometrical solution proposed in the years and the

tuning mechanisms available to modify the spectral response of the device. *Chapter* 2 focuses its attention on liquid crystals and composite materials used in the photonic devices developed in this thesis. They represent an innovative and low cost solution to obtain electro-optical and all-optical low power devices for optical communication systems. *Chapter 3* and *Chapter 4* are to consider the core of this thesis. *Chapter 3* presents an integrated optoelectronic device based on sapphire microsphere integrated with a liquid crystal tuning medium. The great potentiality of microsphere resonators as optofluidic sensors is also reported in the same chapter. *Chapter 4* deals with Bragg's law based filters. We propose an easy way to fabricate electro-optical Bragg's filter based on liquid crystal and a comb-shape configuration of electrodes. In the same chapter we report the fabrication and the optical characterization of an all-optical Bragg's filter.

All devices discussed in *Chapter 3* and *Chapter 4* reports are resonant structures or periodic structures in which $\lambda < g$, where λ is the operating wavelength of the devices and g is the minimal characteristic dimension for the optical structure.

During my Ph.D activity I was also a visiting student at the DTU (Danmarks Tekniske Universitet) in which I studied periodic structures based on *surface plasmons resonance*. In this kind of structures result $\lambda > g$. *Chapter 5* is completely devoted to report and analyze my research results obtained in the field of plasmonics.

To my parents

I tre anni di dottorato hanno rappresentato un momento indimenticabile della mia vita. Per questo mi sento nel dovere di ringraziare delle persone.
Ringrazio Rita, Romeo e Antonio per avermi permesso di lavorare con loro.
Un ringraziamento speciale a mio fratello Marco Trotta: per tutti i momenti vissuti insieme.
Least but not last I want to thank my Thai friend Pilly to help me with my "Italian-English ": ขอบคุณครับ and สวัสดีครับ

LIST OF PUBLICATIONS

[1] R. Asquini, D. Donisi, M. Trotta, A. d'Alessandro, B. Bellini, **G. Gilardi** and R. Beccherelli "*Realization of a liquid crystal electrically controlled optical waveguide on micromachined silicon*", Molecular Crystals and Liquid Crystals, 500, pp 23-30 (2009).

[2] **G. Gilardi**, D. Donisi, A.Serpenguezel and R. Beccherelli, "*Liquid crystal tunable filter based on microsphere resonators*", Optics Letters, 34, 21, pp 3253-3255 (2009).

[3] D. Donisi, B. Bellini, R. Beccherelli, R. Asquini, **G. Gilardi**, M. Trotta and A. d'Alessandro, "*A switchable liquid crystal optical channel waveguide on channel*", Journal of Quantum Electronics, 46, 15, pp 762-768 (2010).

[4] **G. Gilardi**, R. Asquini, A. d'Alessandro and G. Assanto, "*A Widely tunable electro-optic distributed Bragg reflector in liquid crystal waveguide*", Optics Express, 18, 11, PP 11524-11529 (2010).

[5] A. d'Alessandro, R. Asquini, M. Trotta, **G. Gilardi**, R. Beccherelli and I.C. Khoo, "*All-optical intensity modulation of near infrared light in a liquid crystal channel waveguide*", Applied Physics Letters, 97, pp 093302 1 - 3 (2010).

[6] R. Asquini, **G. Gilardi**, A. d'Alessandro and G. Assanto, "*Integrated Bragg reflector in low media: enabling strategies for wavelength tenability in electro-optic liquid crystal*", Optical Engineering, 50, 7, pp 071108 1 – 13 (2011).

[7] **G. Gilardi**, R. Asquini, A. d'Alessandro and G. Assanto, "*An electro-optically tunable Bragg reflector based on liquid crystals*", Molecular Crystals and Liquid Crystals, 549, 1, pp 62-68 (2011).

[8] **G. Gilardi**, L. de Sio, R. Beccherelli, R. Asquini, A. d'Alessandro and C. Umeton, "*Observation of tuneable optical filtering in photosensitive composite structures containing liquid crystals*", Optics Letters, 36, 24, pp 4755-4757 (2011).

[9] **G. Gilardi**, S. Xiao, R. Beccherelli, A. d'Alessandro and N. A. Mortensen, "*Geometrical and fluidic tuning of periodically modulated thin metal films*", Photonics and Nanostructures, (in press 2012).

[10] **G. Gilardi**, L. De Sio, R. Beccherelli, R. Asquini, A. d'Alessandro and C. Umeton, "*All-optical and thermal tuning of a Bragg grating based on photosensitive composite structures containing liquid crystals*", Molecular Crystals and Liquid Crystals (in press 2012).

Papers [2] [4] [6] [7] [8] [9] [10] are included in the thesis.

List of contents

1. Integrated optical structures for filtering and sensing

1.1. Introduction

Since the discovery of the basic interaction mechanisms between light and matter, the fields of optoelectronics and photonics have great advantages that made the enormous success of the fiber optic communications possible. Many types of photonic devices have been designed and investigated in many laboratories. A key role is represented by devices like lasers, optical amplifiers and guiding devices made of glass, silicon and III-V materials. In the development of the modern photonic devices, and then the optical communication systems, there are some crucial stages to remark:

- In the late 1960s, the concept of *integrated optics* emerged. Conventional electrical integrated circuits were replaced by miniaturized optical integrated circuits (OICs), also known as photonic integrated circuits (PICs);
- In the late 1970s, low loss optical fibers and connectors, GaAlAs and GaInAsP laser diodes, and photolithographic micro-fabrication techniques were developed;
- In the 1980s, optical fiber largely replaced metallic wires in telecommunications and a number of manufacturers began the production of optical integrated circuits for several applications;
- In the 1990s, the use of optical fibers for telecommunications and data-transmission networks has been extended to the subscriber loop in many systems. This provides an enormous bandwidth from multichannel transmission of data signals. The increase of the available bandwidth has provided continuing impetus to the development of new integrated optic devices and systems at the beginning of the 21st century;
- In recent years fabrication techniques evolved from micro-technology to nano-technology.

Optical integrated circuits have several advantages when compared to its electrical counterpart, i.e. the electronic integrated circuits. They have the same characteristic bandwidth as the optical fibers because, in both cases, the carrier signal is a light wave rather than an electrical current. Thus, the frequency limiting effects of capacitances and inductances can be avoided.
The design and fabrication of a large scale OIC with a bandwidth to match that of an optical fiber is feasible in principle. It should be possible to multiplex hundreds of signals onto one optical waveguide channel by using the wavelength division multiplexing. The coupling of many optical signals into one waveguide can be conveniently and efficiently accomplished in the optical integrated circuit. In addition, to facilitate the coupling of many signals onto a single waveguide, an optical integrated circuit also lends itself to convenient switching of signal from one waveguide to another. For example, a deposited metal plate on top of the channel of a dual channel directional coupler can be used to control the transfer of optical power [1]. Other advantages of OICs include smaller size, weight and lower power consumption, as well as improved reliability and batch fabrication economy. Optical alignment and vibration sensitivity, which are difficult problems in discrete components, are conveniently controlled in OIC.

1.2. Materials for integrated optic

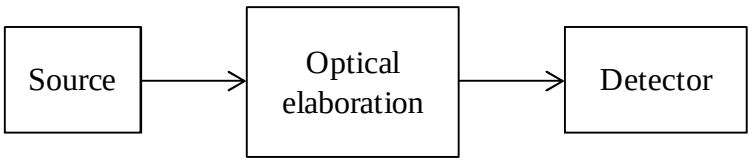

Figure 1.1: General scheme of a complete OIC.

Figure 1.1 shows the general scheme of a complete OIC. The word *complete* means that the OIC provides all functions of generation, detection and elaboration of light. The elaboration block does the common operations like switching, amplification, filtering, etc. In general it is not easy to obtain an OIC, as represented in Figure 1.1, because there is not a substrate material which can considered optimum for all desired functions. The choice of a substrate material on which to fabricate an optical integrated circuit depends mainly on the functions to be implemented in the circuit. There are two basic approaches to fabricate an OIC:

- Hybrid approach: two or more substrate materials are bonded together to optimize performance for different devices,
- Monolithic approach: a single substrate material is used for all devices.

The scheme of Figure 1.1 is to be considered like the union of many OICs, in which each OIC is developed to achieve a particular function. The following Table 1.1 indicates the typical substrate materials used for optical integrated circuits.

Materials for passive devices	**Materials for active devices**
Glass	Gallium arsenide
Quartz	Gallium aluminium arsenide
Lithium niobate	Gallium indium arsenide
Lithium tantalate	Other III – V semiconductors
Silicon	Other II – VI semiconductors
Polymers	

Table 1.1: Common used substrate materials for optical integrated circuits.

Materials for passive devices like glass, silicon, lithium niobate are useful as substrate but generally an external light source, such as semiconductor laser, must be optically and mechanically coupled to the substrate. However, in recent years significant progress has been made in producing light emitters and amplifiers by incorporating erbium and other atoms into substrate materials such as glasses and polymers. While silicon is a material for passive devices, it can be modified applying the techniques of nanophotonics to make it capable of light generation and even laser action as proposed by Intel [2]. The major advantage of the hybrid approach is that the OIC can be fabricated using existing technologies, piercing together devices which have been substantially optimized in a given material. The major disadvantage is that the bonded elements are subject to misalignment, or

even failure, because of vibration and thermal expansion. Also, the monolithic approach is ultimately cheaper if mass production of the circuits is desired.
The ideal material is one based on silicon, since that can leverage the considerable knowledge accumulated by the electronics industry in the mass-production of silicon microprocessors. The disadvantage of silicon is its intrinsic indirect gap that makes the silicon not suitable to generate light. III–V semiconductors are available to generate light, and therefore they are suitable for monolithic integration. Their limit is that the processing of III–V semiconductors is an expensive proposition, because the raw material is expensive, fragile, and requires much more careful processing than glasses and polymers.

1.3. Integrated devices for filtering

The capacity of optical communication systems can exceed 10 Tb/s. The dispersive and nonlinear effects in the optical fiber and the speed of electronic components represent the main limitations for optical communications. Wavelength division multiplexing (WDM) permits to extend the system capacity to beyond 1 TB/s.
In WDM systems multiple optical carriers at different wavelengths are modulated by using independent optical electrical bit streams and they are transmitted over the same fiber. The optical signal at the receiver is demultiplexed into separate channels by using an optical technique. The ultimate capacity of WDM fiber links depends on how closely channels can be packed in the wavelength domain. The minimum channel spacing is limited by interchannel crosstalk. High capacity WDM fiber links require many high performance components, such as integrated lasers, wavelength de(multiplexers), amplifiers and optical filters. Tunable optical filters select one channel at a specific wavelength that can be changed by tuning the passband of the optical filter. Tunable optical filters represent the building blocks of more complex WDM components. The selection mechanism with the most important parameters is reported in Figure 1.2.

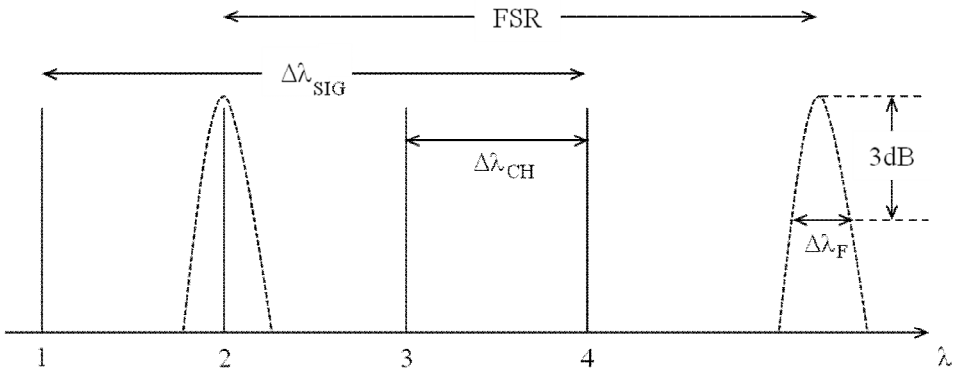

Figure 1.2: Channel selection by mean of a band pass filter.

The filter bandwidth ($\Delta\lambda_F$) must be large enough to transmit the desired channel but, at the same time, small enough to block the neighboring channels ($\Delta\lambda_{CH}$). In other words the filter needs to be designed so that $\Delta\lambda_F < \Delta\lambda_{CH}$. In Figure 1.2, $\Delta\lambda_{SIG}$ represent the bandwidth of the signal.
Tunable optical filters are primarily characterized by their *tuning range* and *tuning time*. The tuning range specifies the range of wavelengths, which can be accessed by a filter. A wide tuning range allows systems to utilize a greater number of channels. The tuning time specifies the time required to tune a filter from one wavelength to another. Fast tunable filters are required for many WDM

network architectures. Other desirable properties of an optical filter are, negligible crosstalk to avoid interference from adjacent channels, small insertion loss, polarization insensitivity, stability against environmental changes and, of course, low cost.
In some pass-band filters the transfer function repeats itself after a certain period, as shown in Figure 1.2. The period of such transfer function is referred to as the *Free Spectral Range* (*FSR*) while the *finesse* (*F*) of a filter measures of the transfer function width. It is the ratio of *FSR* to channel bandwidth, where the channel bandwidth, also called *Full Wave Half Maximum* (*FWHM*) is defined as the -3dB bandwidth of a channel. The number of channels in an optical filter is limited by the *FSR* and *F*. If *F* is high, the transfer functions (pass-band peaks) are narrower, resulting in more channels being able to fit into one *FSR*. With a low *F*, the channels would need to be spaced further apart to avoid crosstalk, resulting in fewer channels. Another important parameter to characterize an optical filter, also related with *F*, is called *Quality factor* (*Q-factor*, or simply *Q*). In the context of resonators, *Q* is defined in terms of the ratio of the energy stored in the resonator to the energy supplied by a generator, per cycle, to keep signal amplitude constant, at a resonant frequency ($f_R=c/\lambda_R$). The stored energy is constant with time:

$$Q = 2\pi \frac{\text{Energy stored}}{\text{Energy dissipated per cycle}} = 2\pi f_R \frac{\text{Energy stored}}{\text{Power loss}} \tag{1.1}$$

The factor 2π makes *Q* expressible in simpler terms.
The following sections are focused on integrated tunable optical filters. In particular in this thesis two categories of integrated optical filters are investigated:

- Optical filters based on resonant structures,
- Optical filters based on periodic structures.

1.3.1. Resonant structures

The Fabry - Perot is the simplest resonant structure. In the years several geometries like microrings, microdisks, microtoroids have been explored. Waveguide based structures like rings and disks, which can be microfabricated onto wafer substrates using conventional integrated circuit deposition and etching techniques, have been demonstrated as channel-dropping filters, switches, and even add-drop multiplexers [3]. Microspheres are another kind of interesting resonant structures due the ease of fabrication. The resonance structure of a microsphere differs considerably from that of a planar waveguide ring resonator. Indeed, a spherical cavity can support very complicated modes with equatorial, radial, as well as polar field dependencies. The total optical loss in such resonators can be extremely low, and the resulting extraordinary high *Q* values of 10^8–10^9 leads to high energy density and narrow resonant wavelength lines. The following pages of this thesis report the basic properties of the resonant structures mentioned above. The microsphere resonators are extensively studied in *Chapter 3*.

The *Fabry - Perot* (*FP*) [4] can be considered as the archetype of the optical resonators. It consists of two parallel mirrors plates with distance *L* that sandwich a material of refractive index n_1. The entire system is immersed in a medium of refractive index n_2.

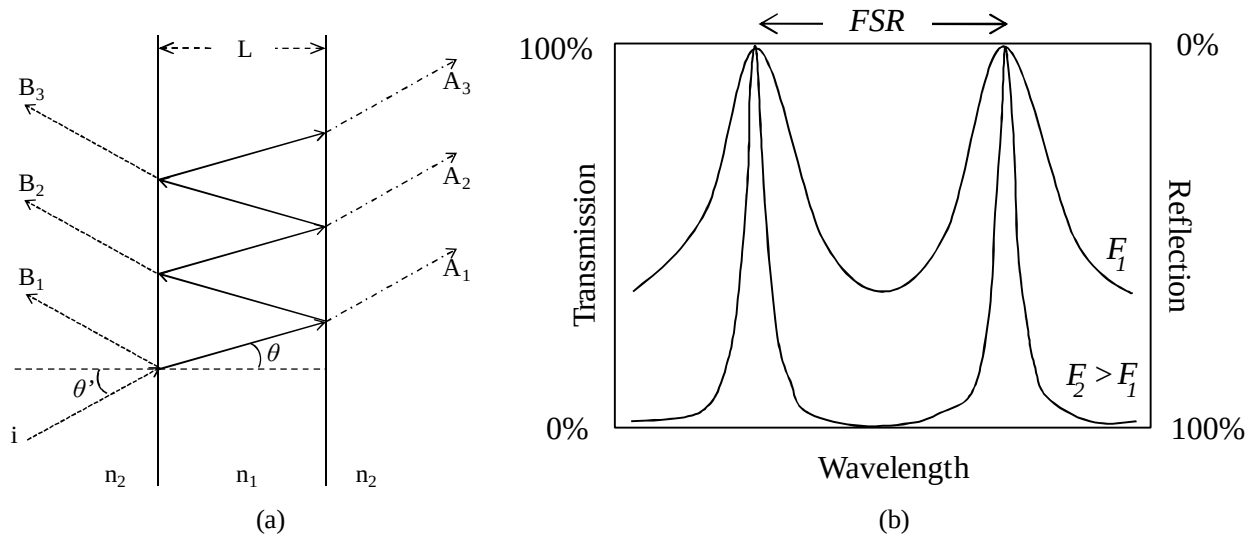

Figure 1.3: (a) Fabry - Perot model with multiple reflections and (b) Ttransmission spectrum for a Fabry - Perot resonator.

The wavelength spacing between two successive transmission peaks, known as the *FSR* is given by:

$$FSR = \frac{\lambda_R^2}{2n_{eff}L} \tag{1.2}$$

n_{eff} is the effective index of the optical mode and L is the *FP* length. The *FSR* is the distance between two consecutive suppressed wavelengths. If the internal losses are neglected, F is given by:

$$F = \frac{FSR}{\Delta\lambda_F} = F = \pi\sqrt{\frac{R}{1-R}} \tag{1.3}$$

It depends only on the mirror reflectivity R, assumed to be the same for both mirrors [5]. There are several technological solutions to fabricate *FP* cavities. Tunable *FP* filters can also be made using several materials such as liquid crystals and semiconductor waveguides [6][7][8][9][10]. Liquid crystal based filters make using of their anisotropic nature to change the refractive index electrically. The tuning is obtained by changing the refractive index rather than the cavity length. Such *FP* filters can provide high finesse (F~300) with a *FWHM* of about 0.2 nm [6]. They can be tuned electrically over 50 nm and the switching time is typically in the order of milliseconds. There are several approaches to fabricate integrated *FP* and to provide their tuning. In one approach an InGaAsP/InP waveguide permits electronic tuning, based on charge injection [9]. Silicon based *FP* filters can be tuned using thermo-optical effect [10]. Micromechanical tuning has also been used for InAlGaAs based *FP* filters [11]. Such filters exhibited a tuning range of 40 nm with <0.35 nm *FWHM* in the 1.55-μm region.

Optical ring resonators consist of a waveguide in a closed loop coupled to one or more input/output (or bus) waveguides. When a proper wavelength is coupled to the loop by the input waveguide, it builds up in intensity over multiple round-trips due to constructive interference. It can be picked up

by a detector waveguide. The response from coupled ring resonators can be custom designed by the using of different coupling configurations.
Integrated ring resonators have emerged in the last few years in integrated optics and have found their way into many applications. They do not require facets or gratings for optical feedback and are thus particularly suited for monolithic integration with other components in a common substrate.

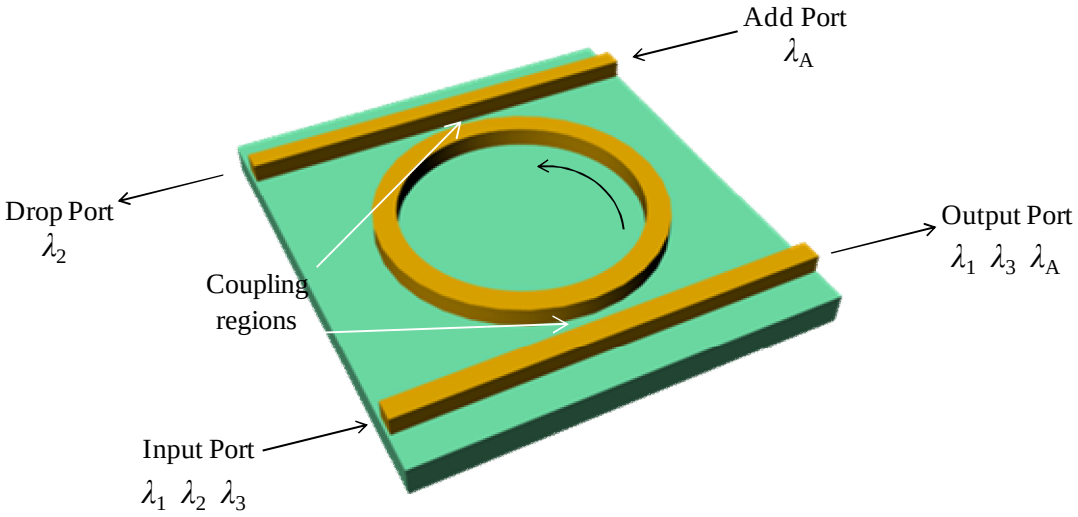

Figure 1.4: Ring resonator channel dropping filter with resonant wavelengths λ_A and λ_2.

A typical configuration is described in Figure 1.4 [12]. Since only some wavelengths resonate within the loop, it works as a filter. Recently, two sets of coupled waveguides have been used to form an add/drop optical filter [13]. Component wavelengths of an optical signal channeled in a waveguide are resonant with the cavity if its effective circumference supports an integer number of wavelengths. For these spectral components, an increased circulation of intensity can build up in the resonator. The presence of a second waveguide coupled to the ring enables extraction of the resonant circulating signal. Thus, at their most fundamental level, ring resonators act as a spectral filter. Also a ring resonator filter can be described by certain figures of merit. The *FSR* and the finesse *F* are respectively:

$$FSR \approx \frac{\lambda^2}{n_{eff} L} \tag{1.4}$$

$$F = \frac{FSR}{\Delta\lambda_F} \tag{1.5}$$

L is the light path length. For high order mode number $L=2\pi R$. For a circularly symmetric ring resonator, the location inside the resonator where we measure the circulating intensity is arbitrary. The intensity after the n^{th} round-trips is:

$$\left|E_n\right|^2 = \exp(-\alpha_{dis} L)\left|E_{n-1}\right|^2 = \exp(-n\alpha_{dis} L)\left|E_0\right|^2 \tag{1.6}$$

Where $\alpha_{dis} = \alpha_{ring} + \alpha_{through} + \alpha_{drop}$. It is a way to take into account all loss terms in a ring resonator. α_{ring} represents the losses due to material absorption, scattering and imperfections in the ring

resonator surfaces. $\alpha_{through}$ and α_{drop} represent the insertion losses when a wavelength is respectively extracted and added. If the number of rounds-trips is large, it can be treated as a continuous variable:

$$\frac{\left|dE_n\right|^2}{dn} = -\alpha_{dis} L \left|E_n\right|^2 \tag{1.7}$$

Each round-trip takes time T_R, then the energy lost per unit time is $\frac{\left|dE_n\right|^2}{dt} = \frac{1}{T_R}\frac{d\left|E_n\right|^2}{dn}$, therefore,

$$Q = \omega_0 \frac{\left|E_n\right|^2}{d\left|E_n\right|^2 / dt} = \frac{\omega_0 T_R}{\alpha_{dis} L} \tag{1.8}$$

From Eqs. (1.6), (1.7) and (1.8):

$$Q = \frac{\omega}{\Delta\omega} \approx \frac{\lambda_R}{\Delta\lambda_F} \tag{1.9}$$

where λ_R is the filter resonant wavelength and $\Delta\lambda_F$ is the bandwidth of the filter as defined in Figure 1.2. For an optical filter the last definition is also mathematically accurate and of practical applicability. Q can be expressed as a function of F. From Equations (1.1) and (1.3) the relationship between the Q and F became:

$$Q = \frac{\omega_0 T_R}{2\pi} F = \frac{\omega_0 L n_{eff}}{2\pi c} F \approx \frac{n_{eff} L}{\lambda_R} F = mF \tag{1.10}$$

For most optical resonators of interest the optical path length is typically many wavelengths long. The *order* (azimuthal number) of a particular resonance is a measure of the number of wavelengths within the circumference, $m = n_{\text{eff}}L/\lambda_{\text{R}}$. The order is also indicative of the m^{th}-peak in the spectrum and it is directly related with Q and F. If N is the number of round-trips required to reduce the energy to $1/e$ of its initial value, from Equation (1.6):

$$\exp\left(-\alpha_{dis} NL\right) = \frac{1}{e} \Rightarrow N = \frac{1}{\alpha_{dis} L} \Rightarrow F = 2\pi N \tag{1.11}$$

Equation (1.11) means that F represents, within a factor of 2π, the number of round-trips made by light in the ring. Similarly,

$$Q = \omega_0 T_R N \tag{1.12}$$

Equation (1.12) means that Q represents the number of oscillations of the field before the circulating energy is depleted to $1/e$ of the initial energy.

The *finesse* and the *Quality factor* are metrics for the intensity buildup and effective interaction time, respectively, in a microresonator. Light interacts with the coupling interface for an F number of times while interacting with the cavity interior for a Q number of cycles.
Ring resonators and disk resonators offer several advantages respect to the *FP*. First, their planar nature is compatible with monolithic micro-fabrication technologies. Second, high finesse operation does not require multilayer or distributed Bragg reflectors but is rather achieved by increasing the gap widths of evanescent couplers. The fabrication of small size ring resonator is important for many reasons:

- The propagation velocity of light is of the order of a few hundred μm per ps in most optical materials of interest, high bandwidths (GHz to THz) are naturally attainable.
- Their small dimensions allow the integration of many devices on the same chip, enabling high–level functionalities.

Several technologies and materials have been investigated for the realization of integrated ring and disk resonators. Most commonly used materials include glass [14], polymers [15], silicon on silica [16], gallium arsenide [17] and indium [18]. III–V semiconductors have high refractive indices (>3) compared with competing material systems such as glass/silica and polymers (~1.5), silicon oxy-nitride (1.45 – 2.1) and LiNbO3 (~2.2) in C-band wavelengths. This allows the fabrication of very high index contrast waveguides that allows the bend radius to be as small as 1 μm before bending losses cause deterioration in performance.
Wavelength tuning is essential for realizing optical filters to be implemented in optical network. There are several techniques to obtain the wavelength tuning in a ring and disk resonator. In general it depends by the material used for the fabrication of the ring. The basic mechanisms adopted to obtain the tuning are:

- *Thermo-optic tuning*. Thermo-optic tuning [19] is realized by heating the component for example by fabricating a metal heater on top of the waveguide in the ring resonator. The refractive index of the material depends on the temperature, and then a resonance shift is achievable. The wavelength shift depends by the termo-optic coefficients of the materials involved in the structure. Limits of the thermo-optic tuning are: slow tuning and reduced density of the device because the heaters and significant power consumption to maintain the tuned status.
- *Electro-optic tuning*. An electric field is applied to change the properties of the material, which means either the refractive index or the absorption. This effect is quite small compared to the effect produced by the heating elements. The change in the refractive index by using the electro-optic effect is weak in III–V materials like InP, but it has the advantage of being fast compared to the thermo-optic effect described before.
- *Carrier injection* is another way to change the refractive index, absorption or gain.
- *Other methods* to obtain the wavelength tuning are mechanically [20], by means of organic materials [21] and opto-optically [22].

A loop can take the form of other closed shapes, such as a disk and toroid. In the case of a ring, the resonator is simply a closed curved waveguide forming a resonant cavity that supports both transverse and longitudinal modes. The confinement and channeling of light in this closed geometry, however, do not require an inner dielectric boundary. The equations used to describe the ring resonator properties have applicability also for disk resonators. The main difference between a ring and a disk is that a disk support optical modes called whispering gallery modes (WGMs).

WGMs occur at particular resonant wavelengths depending on the size of the resonator. At these particular wavelengths, light undergoes total internal reflection at the surface of the resonator creating resonances in the transmission spectrum of the resonator. Whispering gallery resonators (WGRs) are dielectric structures in which light waves are confined by continuous total internal reflection. Extremely high values of *Q* can be achieved in WGMs of very small volume with appropriately designed high precision dielectric interface, and with use of highly transparent materials. When the reflecting boundary has high index contrast, and radius of curvature exceeds several wavelengths, the radiative losses, similar to bending losses of a waveguide, become very small, and the *Q* becomes limited only by material attenuation and scattering caused by geometrical imperfections (e.g., surface roughness). Fabrication of the open dielectric resonators can be very simple and inexpensive, and they lend themselves very well to either hybrid or on-chip integration. Unique combination of very high *Q* and very small volume has attracted interest to applications of the resonators in numerous fundamental science and engineering applications. Small size also results in excellent mechanical stability and easy control of the resonator parameters. The resonators can be easily tuned, stabilized, and integrated into optical networks. All considerations about coupling and fabrication of ring resonators are applicable also for disk resonators.

Among the different types of WGMs resonators, the spherical ones represent a very important category, due to their simplicity, easy fabrication, and very high *Q*. This kind of resonator has unique properties because of their ability to store light in microscopically small volumes for long periods of time. Generalized properties of electromagnetic resonances in dielectric spheres, including their *Q*, will be extensively discussed in the third chapter of this thesis.

1.3.2. Periodic structures

A separate class of tunable optical filters makes use of the wavelength selectivity provided by a Bragg grating. A Bragg grating [23] acts as an optical filter because of the existence of a *stop band*, the frequency region in which most of the incident light is reflected back [24]. The stop band is centred at the Bragg wavelength $\lambda_B = 2n_{eff}\Lambda / m$ where Λ is the grating period, n_{eff} is the average mode index and m is the diffraction order. Bragg gratings play important functions in integrated optics. They can be used in various applications including tunable lasers [25] [26] polarization dispersion compensation and manipulation [27] spectrometry [28] multi/demultiplexing [29] sensing [30] [31] and spectral filtering [32]. Different technologies have been investigated for the realization of integrated optical Bragg gratings. They have been demonstrated by employing waveguides made of different materials and structures such as polymers [25] [26] [33], silicon-on-insulator (SOI) [29] [32], hollow capillaries [27], lithium niobate [34], metal-insulator-metal, [35] silica [36] and liquid crystals [37] [38]. Tuning can be implemented thermo-optically [25] [26], mechanically [33], electrically [36], acusto-optically [34], electro-optically [37] [38] and opto-optically [39].

The largest thermo-optic tuning obtained in a SOI rib waveguide has been 18 nm with an applied voltage of 6 V and a wide bandwidth of about 4 nm [40]. Wavelength shifts between 20 and 30 nm have been also obtained through a thermo-optic effect in polymeric Bragg gratings [25] [26] considering that the wavelength shift obtainable in polymer tunable filters is limited by the polymer thermo-optic coefficient being between 2×10−4 and 4×10−4/°C [33]. Larger wavelength shifts have been obtained by means of mechanical tuning. For example a tuning of about 45 nm has been demonstrated in a polymeric Bragg reflector by imposing a tensile strain on a flexible waveguide

grating device [33] and a tuning over 90 nm with a bandwidth of 0.04 nm has been observed in a silica-based fiber Bragg grating filter through a mechanically beam-bending technique acting on a micrometer screw [41]. A tuning range of 76 nm and filter bandwidth of 1.4 nm without significant change of the filter characteristics has been measured in an acoustically tunable LiNbO3 integrated filter [34]. A wide tuning up to 160 nm has been reached by changing the air-core thickness through a piezoelectric actuator in hollow waveguide Bragg reflectors [42]. Tunable planar Bragg gratings can be realized by using liquid crystals where the peak reflection wavelength tuning is induced by a change of the liquid crystal refractive index controlled by an applied voltage via the large electro-optic response [37].

The periodic nature of index variations couples the forward and backward-propagating waves at wavelengths close to the Bragg wavelength and, as a result, provides frequency-dependent reflectivity to the incident signal over a bandwidth determined by the grating strength. Let us consider a situation in which:

- The index modulation of the periodic medium is concentrated in an array of equidistant planes as depicted in Figure 1.5.
- These planes are infinite so that reflection from these planes is specular. Each of the planes reflects only a very small fraction of the incident plane wave. The total scattered wave consists of a linear superposition of all these partially reflected plane waves. The diffracted beams are found when all these reflected plane waves add up constructively.

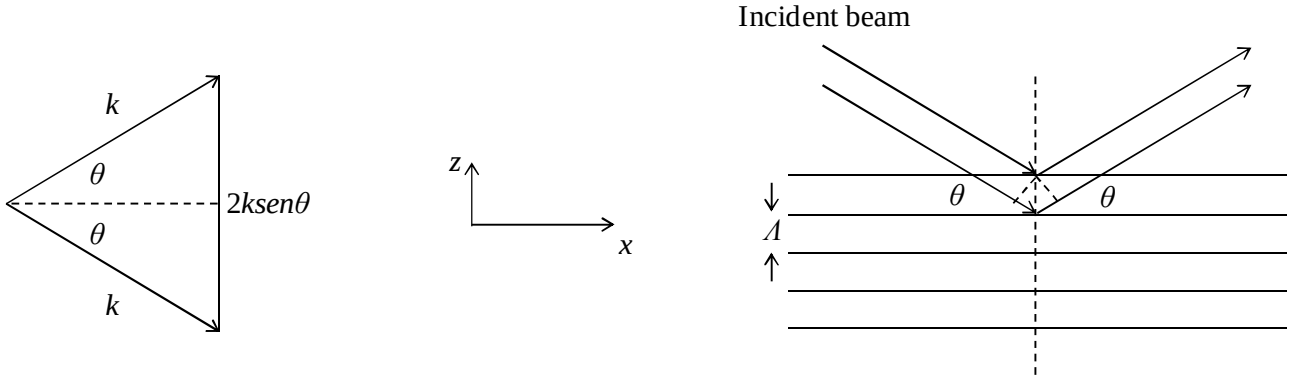

Figure 1.5: Scattering of monochromatic plane wave from a periodic medium.

For a one-dimensional periodic medium, Λ is the period of the index variation in space. The path difference for rays reflected from two adjacent planes is $2\Lambda \sin\theta$, where θ is the angle of incidence measured from the planes. Constructive interference occurs when the path difference is an integral number of wavelengths λ / n_{eff} in the medium, so that:

$$2\Lambda \sin\theta = m\left(\frac{\lambda}{n_{eff}}\right) \qquad m = 1,2,3,... \tag{1.13}$$

where n_{eff} is the spatially averaged index of refraction of the periodic medium and m is an integer. Equation (1.13) is known as the Bragg law. Although reflection from each plane is specular, beam diffraction occurs only for certain values of θ, which obey the Bragg law so that reflections from all planes add up in phase. Another form for Equation (1.13) is:

$$2k\sin\theta = m\left(\frac{2\pi}{\Lambda}\right) \qquad m = 1,2,3,... \tag{1.14}$$

where $k = 2\pi n/\lambda$ is the wavenumber of the light beam in the medium. The left side of Equation 1.14 is the change of the wavevector upon diffraction from the periodic medium. Thus the Bragg law can be interpreted as simply the conservation of momentum. A periodic index function $n(z)$ can be expanded in a Fourier series as:

$$n(z) = n_0 + n_A + \sum_m a_m \exp\left(-i\frac{2\pi}{\Lambda}mz\right) \tag{1.15}$$

where n_0 is the spatially averaged index of refraction, n_A is a constant representing the amplitude of the periodic index modulation, and a_m is the *m*-th Fourier component of the periodic index variation. We note that the *m*-th Fourier component has a wavenumber of $m(2\pi/\Lambda)$. Each of the Fourier components (*m*), can be considered as an infinite set of partial reflectors with a spacing Λ/m responsible for a Bragg diffraction of order *m* according to Equation 1.14. Although the Bragg law is derived by assuming an infinite medium, the results 1.13 and 1.14 are valid, provided the dimensions of these reflection planes are much larger than the beam size.

Under these conditions, the periodic medium is called a *thick* grating (or *volume* grating). In this case, also called Bragg regime, the impinging beam is divided only into a single diffracted beam in addition to a partially transmitted one. In a thin grating, the transverse dimension (thickness) of the periodic index variation is relatively small compared with the beam size and/or wavelength of light. In this case when a plane wave is incident onto the periodic medium, diffraction from each of the planes occurs in addition to the specular reflection. The diffraction from each of these planes is a result of the finite size of the planes. This allows the scattered light to be directed along an angle *θ'*, which can be different from the incident angle *θ*. Using a similar argument leading to Equation (1.13). We obtain the following condition for constructive interference:

$$\Lambda\sin\theta + \Lambda\sin\theta' = m\left(\frac{\lambda}{n}\right) \qquad m = 1,2,3,... \tag{1.16}$$

where *m* is an integer. This is known as the *grating equation*. According to this equation, there are multiple diffraction orders, each one corresponds to a different *m*, for any given angle of incidence. This is the main difference between a *thin* and a *thick* grating. In a *thick* grating, there is only one diffraction order at a given angle of incidence. Figure 1.6 shows a periodic dielectric waveguide in which the periodic dielectric perturbation is due to a small sinusoidal variation of the index of refraction of the guiding layer of a dielectric slab waveguide. The index variation can be obtained, for example, by the diffusion of metal ions into the guiding layer (e.g., Ti diffused in $LiNbO_3$). A similar type of index variation in the core of a single-mode silica fiber can be obtained by UV exposures. A periodic dielectric perturbation can be created also by having a surface corrugation on the guiding layer. The surface corrugation (or surface relief) can be obtained, for example, by using

photolithographic techniques. These periodic waveguides are used for spectral optical filters, mode converters, as well as in distributed feedback lasers.

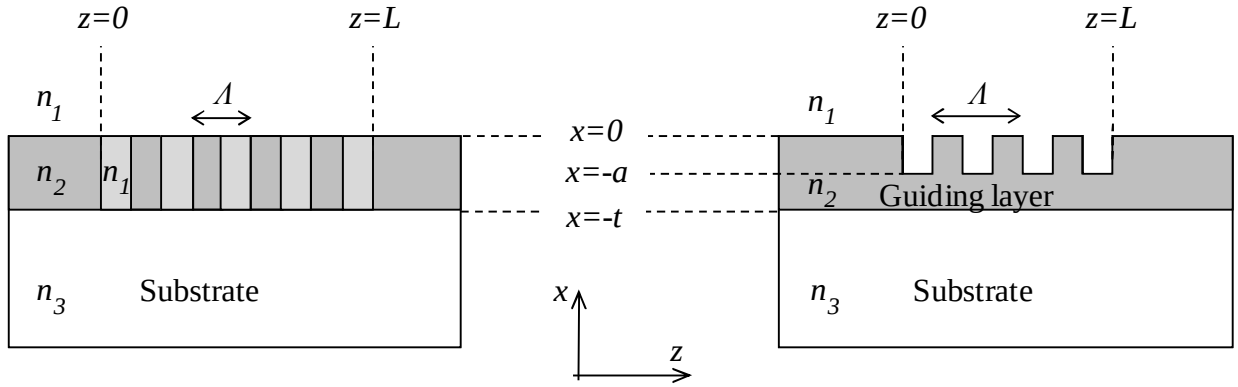

Figure 1.6: Schematic drawing of periodic dielectric waveguides. The periodic dielectric perturbation can be obtained by either changing the index of refraction of the guiding layer (or cladding layer) as shown in (a), or by etching the surface of the guiding layer (or cladding layer) as shown in (b).

The dielectric constant $\varepsilon_a(x,z)$ for the periodic waveguide structure shown in Figure 1.6a can be written as:

$$\varepsilon_a(x,z)=\begin{cases}\varepsilon_0 n_1^2, & 0<x\\ \varepsilon_0 S(z), & -t<x<0\\ \varepsilon_0 n_3^2, & x<-t\end{cases} \tag{1.17}$$

where n_1 and n_3 are the indices of refraction of the layers of the dielectric slab waveguide, t is the thickness of the guiding layer, and $S(z)$ is the periodic dielectric perturbation defined as:

$$S(z)=S(z+\Delta)=\begin{cases}n_1^2, & 0<z<\Lambda/2\\ n_2^2, & \Lambda/2<z<\Lambda\end{cases} \tag{1.18}$$

For the structure shown in Figure 1.6b the periodic dielectric constant is:

$$\varepsilon_a(x,z)=\begin{cases}\varepsilon_0 n_1^2, & 0<x\\ \varepsilon_0 S(z), & -a<x<0\\ \varepsilon_0 n_2^2, & -t<x<a\\ \varepsilon_0 n_3^2, & x<-t\end{cases} \tag{1.19}$$

where a is the depth of the surface corrugation (see Figure 1.6b), and $S(z)$ is reported in Equation (1.18).

Depending on the applications, it can be necessary to have broadband reflectors or spectral filters with narrow bandwidth. In broadband Bragg reflector applications, it is essential a strong dielectric perturbation, which provides a large coupling constant for the contradirectional coupling. The dielectric perturbation provides the coupling between an incoming mode and the same mode that

propagates in the opposite direction. In multimode waveguides, a strong periodic dielectric perturbation may cause coupling between modes of different spatial wavefunctions.
In other words, it may couple a mode $E_k \exp[i(\omega t - \beta_k z)]$ to a different mode $E_n \exp[i(\omega t - \beta_n z)]$ propagating in the opposite direction. The situation in a single-mode waveguide is relatively simple. We first consider the simple case of a TE mode propagation in a single-mode slab waveguide structure. Furthermore, we are interested in the spectral regime where the forward propagating TE mode $AE_0(x)\exp[i(\omega t - \beta z)]$ is only coupled with the backward wave $BE_0(x)\exp[i(\omega t - \beta z)]$, where A and B are constants, and $E_0(x)$ is the TE mode wavefunction. An efficient contradirectional coupling occurs only when $\beta - (-\beta) = 2\beta = 2m\pi/\Lambda$ for some integer m. The coupling between the backward and the forward by the m-th Fourier component of the periodic dielectric perturbation can thus be described by:

$$\begin{aligned} \frac{d}{dz}A &= -i\kappa B(z)\exp(i\Delta\beta z) \\ \frac{d}{dz}B &= i\kappa^* A(z)\exp(-i\Delta\beta z) \end{aligned} \tag{1.20}$$

where the coupling constant κ, for the case of periodic surface corrugation, is given by:

$$\kappa = \frac{\omega}{4}\varepsilon_0 b_m (n_1^2 - n_2^2)\int_{-a}^{0} \left|E_{0y}(x)\right|^2 dx \tag{1.21}$$

where $E_{0y}(x)$ is the wavefunction of the fundamental TE mode. It is possible to note that the magnitude of the coupling constant is an increasing function of the depth of the corrugation. The momentum mismatch is given by:

$$\Delta\beta = \beta - (-\beta) - m\frac{2\pi}{\Lambda} = 2\beta - m\frac{2\pi}{\Lambda} = 2(\beta - \beta_0) \tag{1.22}$$

where $\beta_0 = m\pi/\Lambda$.. For the case of the fundamental TE mode in a single-mode waveguide, is defined n_{eff} as the effective index of the mode such that:

$$\beta = n_{eff}\frac{\omega}{c} = n_{eff}\frac{2\pi}{\lambda} \tag{1.23}$$

The momentum mismatch in the contradirectional coupling can thus be written as:

$$\Delta\beta = 2\beta - m\frac{2\pi}{\Lambda} = \frac{2n_{eff}}{c}(\omega - \omega_0) \tag{1.24}$$

where ω_0 is the center frequency where the Bragg condition is satisfied. The coupled equations can be solved analytically and the general solutions are written as:

$$A(z) = C_1 e^{i(\Delta\beta/2)z - sz} + C_2 e^{i(\Delta\beta/2)z + sz}$$
$$B(z) = \frac{i}{\kappa}\frac{d}{dz}A(z) \tag{1.25}$$

where C_1 and C_2 are constants, and the parameter *s* is given by:

$$s = \sqrt{|\kappa|^2 - \left(\frac{\Delta\beta}{2}\right)^2} = \sqrt{|\kappa|^2 - [\beta(\omega) - \beta_0]^2} \tag{1.26}$$

The solution subject to the boundary condition $B(L) = 0$ can be written as:

$$A(z) = e^{i(\Delta\beta/2)z}\frac{s\cosh s(L-z) + i(\Delta\beta/2)\sinh s(L-z)}{s\cosh sL + i(\Delta\beta/2)\sinh sL}$$
$$B(z) = e^{-i(\Delta\beta/2)z}\frac{-i\kappa^* \sinh s(L-z)}{s\cosh sL + i(\Delta\beta/2)\sinh sL}A(0) \tag{1.27}$$

The reflectance (or diffraction efficiency) is given by:

$$R = \left|\frac{B(0)}{A(0)}\right|^2 = \frac{|\kappa|^2 \sinh^2 sL}{s^2\cosh^2 sL + (\Delta\beta/2)^2 \sinh^2 sL} \tag{1.28}$$

Maximum reflectance occurs at $\Delta\beta = 0$, where the reflectance is given by:

$$R_{MAX} = \tanh^2|\kappa|L \tag{1.29}$$

It is possible to note that the reflectance is an increasing function of $|\kappa|L$. Significant contradirectional coupling occurs in the spectral regime, where $-2|\kappa| < \Delta\beta < 2|\kappa|$. In this regime, the parameter *s* is real and the general solutions are exponential, indicating a strong exchange of energy between the forward mode and the backward mode. This spectral regime is equivalent to a frequency range of:

$$-\frac{|\kappa|c}{n_{eff}} < \omega - m\frac{\pi c}{n_{eff}\Lambda} < \frac{|\kappa|c}{n_{eff}} \qquad m = 1,2,3,... \tag{1.30}$$

The spectral width of the photonic bandgap where the peak reflectance occurs is thus given by:

$$\Delta\omega_{gap} = 2\frac{|\kappa|c}{ne_{ff}} \tag{1.31}$$

where we recall that n_{eff} is the effective index of the mode. It is important to note that the coupling constant depends on the Fourier expansion order *m*. An effective broadband reflector must have a high reflectance. Since the peak reflectance is given by $\tanh^2|\kappa|L$, an efficient broadband reflector

requires $|\kappa|L > 1$. Furthermore, the useful bandwidth for reflection is limited by the photonic bandgap $\Delta\omega_{gap}$. Thus a large coupling constant κ is desirable for a broadband reflector. For spectral filter applications, it is rather suitable to have a spectral filter that provides a narrow bandwidth. In the area of optical communications, spectral filters with narrow bandwidth of a few GHz are often needed. These filters are employed to block undesirable radiation and to transmit only the radiation in the desired spectral regime. A weak periodic perturbation with a small coupling constant is desirable for this application. Figure 1.7 shows the coupling efficiency as a function of the phase mismatch in contradirectional coupling.

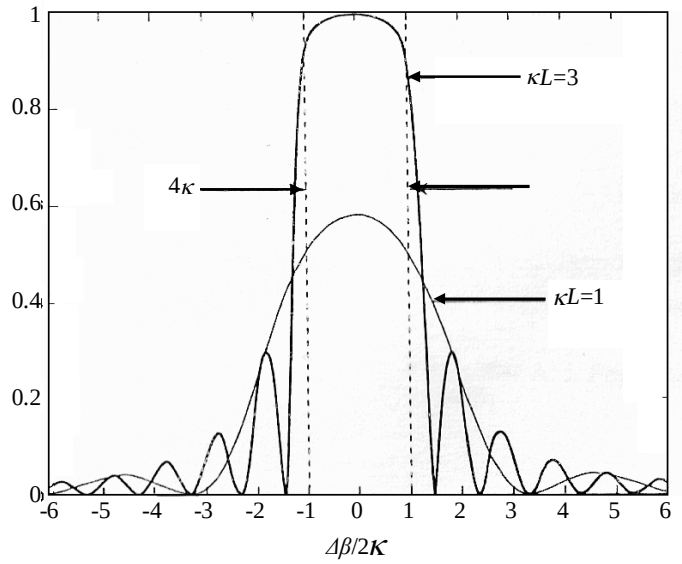

Figure 1.7: Coupling efficiency as a function of the phase mismatch $\Delta\beta$.

The width of the main peak can be estimated by imposing $\Delta\beta = 4\kappa$. After some mathematical steps, the bandwidth is given by:

$$\frac{\Delta\omega_{gap}}{\omega_0} = 2\left|\frac{n_1}{n_0}\right| \tag{1.32}$$

For example, a bandwidth of 25 GHz at λ=1550nm would require an index modulation of $n_1 / n_0 = 6 \cdot 10^{-5}$. As noted earlier, a narrowband filter requires a small coupling constant. The reflectance spectrum as shown in Figure 1.7 exhibits several sidelobes on both sides of the photonic bandgap. These sidelobes result from the impedance mismatch at the edge of the periodic structure. For spectral filter applications, these sidelobes are very undesirable. There are two different techniques to attenuate these side lobes: the grating apodization and chirping. The spatial apodization smooths over the transition from the homogeneous region to the periodic region, while the second one provides a variation of the grating pitch along the axis of optical propagation.
In chapter four we will discuss integrated Bragg reflectors in low-index media, enabling strategies for wavelength tunability in electro-optic and all-optical liquid crystals.

1.4. Integrated devices for sensing

Resonators structures are fascinating both for their geometric simplicity and for their ability to efficiently confine optical energy within small mode volumes. Recently, incorporation of resonators with fluidics has come under intensive investigation. Such an integration belongs to a newly defined area called optofluidics [43], which describes optical systems including fluids. This kind of system is able to achieve additional functionality into chip-based microfluidics. Optofluidic resonators are optical devices in which the resonator and fluidic systems are combined to produce synergistic functionality that could not otherwise be achieved. The fluid in the device may be injected from an external part of the device or it may be inherent to the resonant geometry. With regard to development of sensors, optofluidics provide the benefit of small sample volumes, easy sample delivery and tunability.

Micro-optofluidics and nano-optofluidics are also being explored for developing functional lab-on-chip systems and sensors [44]. Integration of these systems offers significant advantages including minimized consumption of reagents, portability, increased automation and reduced costs. Identification and quantification of the analyte can be accomplished by evaluation of the refractive index. This can be measured by several techniques, such as evanescent waves in liquid waveguides [45], surface plasmon resonance [46] [47], long period gratings [48], interference at the liquid-solid interface [49], Fabry-Perot cavity [50], Mach-Zender interferometry [51] and ring resonators [52].

Reducing the liquid volume is a crucial requirement for many applications involving traces of substances. In such cases, detection techniques with high sensitivity to refractive index variations in extremely small volumes of fluids are needed. The smallest volume measured claimed up to date was in the order of 10 femtoliter, though without apparent confinement [53]. However, as the volumes shrinks, so does the light-analyte interaction volume with the probing light. This problem can be circumvented by increasing, either the effective interaction depth or the effective interaction length. The former can be increased by confining the resonant optical field close to the liquid sample. The latter can be increased by using resonant techniques based on multi-pass interaction. However, multi-pass interaction demands resonant cavities with long photon lifetimes or, in other words, a high *Q*:

$$Q = \frac{E}{\Delta E} = \omega_R \tau = \frac{2\pi c \tau}{\lambda_R} \tag{1.33}$$

where *c* is the speed of light, E is the energy stored in the resonator, ΔE is the energy lost per unit cycle associated with the considered resonance, τ, ω_R and λ_R are the ring down time (i.e. photon lifetime), circular frequency and wavelength at resonance, respectively. An equivalent definition is often given as:

$$Q = \frac{\lambda_R}{\Delta\lambda} \tag{1.34}$$

where $\Delta\lambda$ is the line width. The former definition allows to measure the *Q* with a ring down technique in the time domain [54].

The highest value of Q reported to date for ring resonators is $Q = 1.2 \cdot 10^6$ [55] in air with much lower values in denser fluids. The capillary-based optofluidic ring resonator (OFRR) is also an interesting approach, though the demonstrated Q is still moderate ($1.2 \cdot 10^5$) [56]. The highest Q reported to date for unloaded WGM resonators is 10^8 in air and 10^6 in water for microtoroids [57] and 10^{11} for microspheres [58]. However, in most cases, in- and out-coupling are performed by a fragile suspended tapered fiber optics, which is accurately positioned by using bulky and expensive 3-axis nanopositiong stages. This coupling technique is effective to show proof of principle on bulky vibration-free optical benches, but it is not amenable to confine tiny quantities of liquid analyte nor to integration and large scale deployment in lab-on-chips. It has been recently shown that coupling by integrated optical waveguides [59] [60] is also possible. In WGM sensors, estimation of the refractive index is performed by measuring the frequency shift of the resonance peak. All measurement techniques to evaluate refractive index change, can be reassumed in three separated categories:

a) Evanescent field based method,
b) Resonant cavity based method,
c) Surface plasmon based method.

a) The *field evanescent method* was first proposed in 1960's [61]. In this technique the optical field is divided between the waveguiding material and the volume around the sensor. The optical field directly interacts with the analyte. One advantage of this technique is that the waveguides are not band-width-limited. To characterize the performance of an evanescent waveguide sensor the parameters known as penetration depth and threshold sensitivity are the most interesting parameters.
The penetration depth characterizes the overlap of the evanescent field with the environment. In this respect is desirable to have a large penetration depth as much as possible, to increase the detected area. The expression for penetration depth is:

$$d_p = \frac{\lambda_R}{2\pi\sqrt{n_1^2 \sin^2\theta - n_2^2}} \tag{1.35}$$

In general there is a balance between increasing penetration depth, which increases the detection efficiency, and increasing of the loss of the device, which negatively affects both the signal: noise and sensitivity. A waveguide sensor is sensitive to environmental changes as temperature. Therefore, a more complex method of detection was implemented based on an integrated Mach-Zehnder Interferometer (MZI) [51] where the environmental effects are normalized out of the signal by the application of the reference arm.

b) *Optical resonant cavities* is an extension or subset of evanescent-based detection. A discrete set of wavelengths are resonantly coupled with the cavity [62]. The detection mechanism for optical cavities is similar to that of optical waveguides. The optical field interacts with the substance (i.e. fluids or molecules) around the surface of the cavities. This change is detected as a shift in the resonant frequency of the device. To perform the detection one can monitoring also the power, but much higher sensitivity is achieved by monitoring changes in the resonant frequency of the device.

The interaction between the optical field and an external variation can be described by the application of Maxwell's equation to the simple governing relations of optical microcavities. An optical cavity's resonance condition is defined by the wavelength λ for which the cavity's circumference is an integer multiple of the orbital wavelengths. Therefore, the resonant wavelength must be changed for any change in the cavity radius (R) or refractive index (n) according to the following [63]:

$$\frac{\Delta\lambda}{\lambda} = \frac{\Delta R}{R} + \frac{\Delta n}{n} \tag{1.36}$$

A variation of n or a variation of R will shift the resonant wavelength.

c) A surface plasmon or surface plasmon-polariton (SPP) is an electromagnetic wave which propagates at a metal-dielectric interface. The conditions for generating a surface plasmon mode depends on the geometry of the plasmonic structure and the environmental parameters. Therefore any changes in the environment, such as the binding of biomolecules or fluids to the surface of the metal film will change the plasmon resonance. Several methods have been proposed to detect refractive index changes using surface plasmon resonance [64] [65]. These are typically defined by the method of detecting the sensing signal. The most common methods are:

- Angular,
- Spectral,
- Localized.

In angular detection, transverse polarized light is incident on a coupling prism, generating an evanescent field. Because the field is non-propagating at the majority angles, the optical power is reflected back into a photodetector, with minimal loss. At specific angle of incidence (θ_{sp}) the energy is coupled into the metal film generating the surface plasmon resonance. This phenomena is detected as a reduction in power that is described by:

$$\sin\theta_{sp} = \frac{1}{n_p}\sqrt{\frac{\varepsilon_m(\lambda)\varepsilon_d}{\varepsilon_m(\lambda)+\varepsilon_d}} \tag{1.37}$$

where n_p is the refractive index of the prism, $\varepsilon_m(\lambda)$ is the dielectric constant of the metal film, λ is the wavelength ε_d is the dielectric constant of the dielectric layer.

Spectral surface plasmon detection exploits this dependence to monitor the coupling conditions between the incident wave and the generated plasmon. The main difference between angular and spectral detection is in the experimental apparatus. In angular detection, the incident angle is varied, and the wavelength is constant. In spectral detection, the incident angle is constant and the wavelength is varied.

An emerging field on in surface plasmon detection is based on highly localized plasmon fields. These can be generated using ordered arrays of nanoparticles or nanohole arrays. By creating more localized optical fields, the sensitivity of the device to change the environmental dielectric is greatly increased.

2. Liquid crystals and composite materials for photonic applications

2.1. Introduction

Liquid crystals (LC's) science and applications permeate almost all segments of the society, from large industrial displays to individual homes and office devices. The words "liquid crystals" became famous and of common knowledge because the impressive success LC flat panel display technology. Anyway LC's have an important role in photonic devices and network applications, especially when a wavelength tuning is required [66] [67]. Functional devices can be made with these materials, by confining them between two surface aligning substrates separated by just a few micrometers.

The confinement with two plane and parallel surfaces is of course widely used in flat display technology but it is not the only way to confine LC's. In several applications the LC's are confined with polymer interfaces and also the field of liquid crystals on silicon (LCOS) [68], in which mircomachined silicon structures acts as chamber for the liquid crystals, is well developed.

LC's are anisotropic uniaxial materials, with birefringence exceeding 0.2 or even higher. This may result in large phase shifts within very short optical paths. Furthermore, various powerful electro optical field effects designed for LC enable low power consumption applications by voltage controlling the direction of the LC optic axis. The combination of device-specific LC-molecular properties and electro-optical effects makes LC's attractive as materials for many opto-electronic applications, not just displays [69]. Signal processing devices based on free-space spatial light modulators have been demonstrated to perform optical functions such as beam steering and optical switching among optical fibers for telecommunications [70]. Optical filters using fiber Fabry-Perot LC cavities have also been demonstrated [67]. Polarization conversion of near-infrared light, based on nonlinear effect has been shown in a simple standard LC cell [71]. While such free space components have good performance for optical communication systems their insertion losses are very high [70]. This is mainly due to light passing repeatedly through indium tin oxide electrodes. In integrated optics, the use of LC as a propagation medium was originally discarded. This was because large light scattering losses were found in LC's made of rod-like molecules [72]. However following improved alignment of the LC's, scattering losses can be greatly reduced and integrated optics using LC's is worth being reconsidered, enabling competitive integrated optical devices based on LC's. Another competitive feature of using LC's for photonic integrated circuits is associated with the LC light absorbance. Like virtually all organic materials, LC's absorb light in the UV region. The values of their ordinary refractive indices range from 1.45 - 1.6 which perfectly match the refractive indices of silica optical fibers and low loss silica on silicon optical waveguides. Mechanical stability and the possibility to photo-pattern the alignment of LCs [73], on a nano/micro scale are other interesting features of LCs compared with state-of-the art opto-mechanical micro switches [74].

Ultrashort vertical directional couplers made of passive waveguides separated by a gap filled with refractive index-controllable LC-material have been predicted by exploiting LCs exhibiting large birefringence, which allow coupling lengths shorter than 100 micrometers. These vertical couplers were shown to be applicable in novel compact guided wave optical switches.

Another important LC feature is the possibility of mixing them with polymers, obtaining composite materials with extremely useful optical properties for the realization of novel photonic devices. In general LC and composites can be considered as active materials to be combined with low loss and reliable passive waveguide technology.

2.2. Liquid crystals: basic properties

Nematics Liquid Crystals (NLC) are the most widely studied and used LC. Nematics best exemplify the dual nature of liquid crystals fluidity and crystalline structure. In this section we reports only the basic properties necessary to understand all LC-based devices proposed in the following chapters of this thesis. Then we introduce the order parameter, elastic constants, free energies and the interaction between NLC and an external electric field.

2.2.1. Order parameter and free energy

The liquid crystalline phases can be divided in two different types: the ordered phase and the disordered phase. For the ordered phase the physical properties of (LC) are studied with the elastic continuum theory.

LC's either in the disordered or isotropic phase behave like ordinary fluids of anisotropic molecules. They can thus be described by theories pertaining to anisotropic fluids. The physics of LC is best described in terms of the so-called order parameters. If $\hat{k}$ is the long axis of the molecule, the microscopic scalar order parameter *S* is defined as:

$$S = \frac{1}{2}\left\langle 3\left(\hat{k}\cdot\hat{n}\right)\left(\hat{k}\cdot\hat{n}\right)-1\right\rangle = \frac{1}{2}\left\langle 3\cos^2\theta - 1\right\rangle \tag{2.1}$$

θ is the angle made by the molecular axis with the director axis (See figure 2.1). The average $\langle\ \rangle$ is taken over the whole ensemble. The scalar order parameter defined previously is sufficient to describe liquid crystalline systems composed of molecules that possess cylindrical or rotational symmetry around the long axis $\hat{k}$.

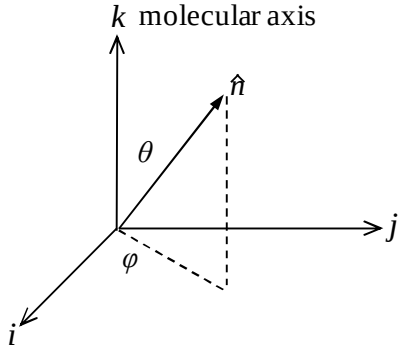

Figure 2.1: Coordinate system defining the microscopic order parameter of a nematic liquid crystal molecule. *i*, *j*, and *k* are the molecular axes, whereas $\hat{n}$ denotes the average direction of liquid crystal alignment.

The order parameter, defined by Equation (2.1), is an average over the whole system and therefore provides a measure of the orientation order. The smaller the fluctuation of the molecular axis from the director axis orientation direction, the closer the magnitude of *S* is to unity.

In a perfectly aligned (LC), $\left\langle \cos^2\theta \right\rangle = 1$ so that *S* = 1, while in a perfect random system, such as isotropic phase of LC, $\left\langle \cos^2\theta \right\rangle = \frac{1}{3}$ and *S* = 0.

Because of the application of an external perturbation field, a NLC undergo deformation as any solid. Figure 2.2a depicts a "solid" subjected to torsion, with one end fixed.

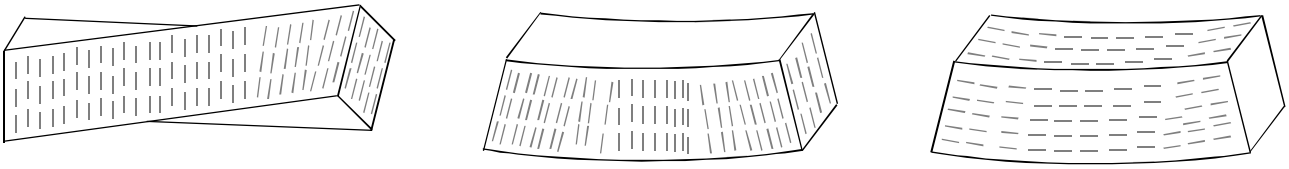

Twist (a) Splay (b) Bend (c)

Figure 2.2: Deformations in a nematic liquid crystal.

In ordinary solids this would create a very large stress, arising from the fact that the molecules are translationally displaced by the torsional stress. On the other hand, such Twist deformations in LC, owing to the fluidity of the molecules, simply involve a rotation of the molecules in the direction of the torque; there is no translational displacement of the center of gravity of the molecules, and thus, the elastic energy involved is quite small. Similarly, other types of deformations such as Splay and Bend deformations, as shown in Figures 2.2b and 2.2c, respectively, involving mainly changes in the director axis, will incur much less elastic energy change than the corresponding ones in ordinary solids. Figures 2.2a - 2.2c show that the Splay and Bend deformations necessarily involve flow of the LC, whereas the Twist deformation does not. Twist, Splay and Bend are the three principal distinct director axis deformations in NLC. Following the theoretical formalism first developed by Frank [75], the free-energy densities the free-energy densities (in units of energy per volume) associated with these deformations are given by:

$$\text{Splay: } f_1 = \frac{1}{2}K_1\left(\nabla \cdot \hat{n}\right)^2 \tag{2.2}$$

$$\text{Twist: } f_2 = \frac{1}{2}K_2\left(\hat{n} \cdot \nabla \times \hat{n}\right)^2 \tag{2.3}$$

$$\text{Bend: } f_3 = \frac{1}{2}K_3\left(\hat{n} \times \nabla \times \hat{n}\right)^2 \tag{2.4}$$

K_1, K_2 and K_3 are the respective Frank elastic constants. As the optical properties of LC depend on applied voltage I developed a vectorial optical model of the electro-optical response of the material. The model couples the free energy minimization of the LC director profile and the Poisson equation solution. The local electric field reorienting the LC molecules varies from point to point while reorientation occurs. This behavior is common to all LC devices.

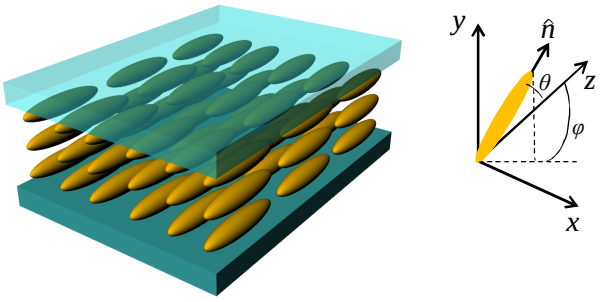

Figure 2.3: Liquid crystal standard cell.

However, I present here a simplex LC cell to study the reorientation of the LC. Therefore, coupling of the free energy minimization and Poisson equation is needed to provide a detailed profile of the LC director, and hence of the refractive indices distribution.
The orientation of the LC director $\hat{n}$ corresponds to the minimum of free energy, which includes the elastic and the electrostatic term. The elastic energy is referred to as Oseen–Frank energy and is expressed as:

$$F_{elastic} = \frac{1}{2}\iiint \left\{ K_1 \left(\vec{\nabla}\cdot\hat{n}\right)^2 + \frac{1}{2}K_2\left[\hat{n}\cdot\left(\vec{\nabla}\times\hat{n}\right)\right]^2 + \frac{1}{2}K_3\left[\vec{n}\times\left(\nabla\times\hat{n}\right)\right]^2 \right\} dv \tag{2.5}$$

dv is the elementary volume cell. The boundary conditions are assumed constant (strong anchoring) so that they do not contribute to *F*. The overall integral to be minimized is therefore:

$$F = F_{elastic} - \iiint \left[\frac{1}{2}\varepsilon_0\varepsilon_\perp \left|\vec{E}\right|^2 + \frac{1}{2}\varepsilon_0\Delta\varepsilon(\vec{E}\cdot\vec{n})^2 \right] dv \tag{2.6}$$

where $\vec{E} = -\vec{\nabla}V$ is the applied electric field, $\varepsilon_\perp$ is the permittivity when the field is applied perpendicular to the director $\hat{n}$ and $\Delta\varepsilon$ is the relative dielectric anisotropy.
The minimization of *F* is achieved by solving the Euler - Lagrange equation of the free energy density. This approach is simpler than global or relaxation approaches, and therefore more adapted for large 3D problems. To solve the partial derivative equation, a finite element method is well suited since it permits implementation of the weak form of the Euler - Lagrange equation. We have implemented the weak form model on COMSOL Multiphysics: it allows us to use a finite element method, and to couple the problems of the stationary value of *F* with the solution of the Poisson equation for the distribution of the electric field in the structure:

$$\vec{\nabla}\cdot\left[\varepsilon_\perp\vec{\nabla}V + \Delta\varepsilon(\vec{\nabla}V\cdot\vec{n})\vec{n}\right] = 0 \text{ in LC} \tag{2.7}$$

The weak formulation might produce a spurious solution. When this occurs, the boundary conditions should be carefully chosen and solutions at intermediate voltages may help achieve the final convergence. The resulting output data are the spatial distribution of the LC tilt and twist angles or equivalently the director orientation:

$$n_x = \cos(Tilt)\cdot\sin(Twist) \tag{2.8}$$

$$n_y = \sin(Tilt) \tag{2.9}$$

$$n_z = \cos(Tilt)\cdot\cos(Twist) \tag{2.10}$$

where n_x, n_y and n_z are the projection of the molecular director on the referential system indicated in Figure 2.3. Simple algebraic calculations give the spatial distribution of the permittivity tensor [76]:

$$\varepsilon_{xx} = n_0^2 + \left(n_e^2 - n_o^2\right)\cos^2(Tilt)\sin^2(Twist) \tag{2.11}$$

$$\varepsilon_{yy} = n_0^2 + \left(n_e^2 - n_o^2\right)\sin^2(Tilt) \tag{2.12}$$

$$\varepsilon_{zz} = n_0^2 + \left(n_e^2 - n_o^2\right)\cos^2(Tilt)\cos^2(Twist) \tag{2.13}$$

$$\varepsilon_{xy} = \varepsilon_{yx} = \left(n_e^2 - n_o^2\right)\sin(Tilt)\cos(Tilt)\sin(Twist) \tag{2.14}$$

The advantage of this model is that we do not make any hypothesis or simplification of the director and electric potential distributions. Therefore, this fully consistent model may be used for any type of geometry, either two or three dimensional, provided the boundary conditions are correctly stated.

2.2.2. Dielectric constants and refractive indices

Dielectric constants and refractive indices are physical parameters that characterize the electronic responses of LC to externally applied fields (electric or optical). Their values are highly dependent on the direction and the frequencies of the field. We consider the interaction between the LC and a low frequency external electric field. The dielectric constant ε is defined by the Maxwell equation:

$$\vec{D} = \vec{\varepsilon}\cdot\vec{E} \tag{2.15}$$

$\vec{D}$ is the displacement current, $\vec{E}$ is the electric field and $\vec{\varepsilon}$ is the dielectric tensor. For a uniaxial NLC:

$$\vec{\varepsilon} = \begin{bmatrix} \varepsilon_\perp & 0 & 0 \\ 0 & \varepsilon_\perp & 0 \\ 0 & 0 & \varepsilon_\parallel \end{bmatrix} \tag{2.16}$$

For the two principle axes we obtain:

$$D_\parallel = \varepsilon_\parallel E_\parallel \tag{2.17}$$

$$D_\perp = \varepsilon_\perp E_\perp \tag{2.18}$$

$\varepsilon_\parallel$ and $\varepsilon_\perp$ are in the order of $5\varepsilon_0$. Most nematics, as E7, possess positive dielectric anisotropy $\varepsilon_\parallel > \varepsilon_\perp$. In all devices proposed in this thesis we use the LC called E7 [77]. Its characteristics at λ = 1550 nm and T= 20°C are:

Permettivity	Refractive index	Elastic constants
$\varepsilon_{\parallel} = 20$	$n_e = 1.69$	$K_1 = 12\text{pN}$
$\varepsilon_{\perp} = 7$	$n_o = 1.5$	$K_2 = 7.3\text{pN}$
		$K_3 = 17\text{pN}$

Table 2.1: Liquid crystal E7 dielectric and mechanical properties.

The Figure 2.4 shows the wavelength-dependent refractive indices of E7 at T= 25 °C. The open squares and circles are the n_e and n_o of E7 in the visible region while the downward and upward triangles stand for the measured data at λ=1.55 μm and λ=10.6 μm, respectively [78].

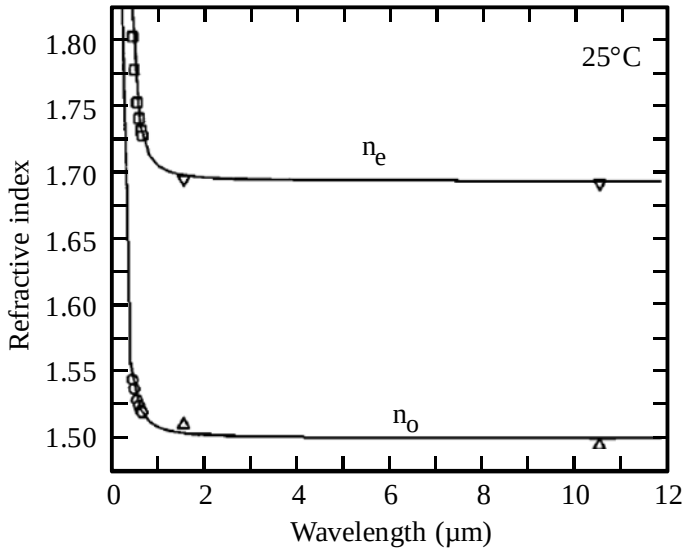

Figure 2.4: Wavelength-dependent refractive indices of E7 at 25 °C.

The solid curve are the fittings to the experimental data in the visible spectrum by using the extended Cauchy model.

The dependency on temperature can be expressed as a function of the average refractive index <*n*> and of the birefringence Δ*n*:

$$n_e = \langle n \rangle + \frac{2}{3}\Delta n \tag{2.19}$$

$$n_o = \langle n \rangle - \frac{1}{3}\Delta n \tag{2.20}$$

The average refractive index linearly decreases with temperature:

$$\langle n \rangle = A - BT \tag{2.21}$$

The birefringence depends on temperature according to Haller approximation:

$$\Delta n(T) = (\Delta n)_0 \left(1 - \frac{T}{T_c}\right)^{\beta} \tag{2.22}$$

where $(\Delta n)_0$ is the birefringence at T= 0 K, β is a material constant and T_c is the nematic-isotropic phase transition temperature (clearing point). The overall expression of refractive index as a function of temperature is therefore:

$$n_e(T) = A - BT + \frac{2(\Delta n)_0}{3}\left(1 - \frac{T}{T_c}\right)^{\beta} \tag{2.23}$$

$$n_o(T) = A - BT - \frac{(\Delta n)_0}{3}\left(1 - \frac{T}{T_c}\right)^{\beta} \tag{2.24}$$

These equations have four parameters: [*A*, *B*] and [$(\Delta n)_0$, β]. They can be determined by measurements of n_e and n_o at two temperatures. We can get [*A*, *B*] and [$(\Delta n)_0$, β] respectively, by two-stage fittings. By arranging the equations (2.20) and (2.21) we find $\langle n \rangle = (n_e + 2n_o)/3$. To obtain [*A*, *B*], we fit the average refractive index as a function of temperature using equation (2.21). To find [$(\Delta n)_0$, β] we fit the birefringence data as a function of temperature using (2.22). Therefore, these two sets of parameters can be obtained independently from the same set of refractive indices but at different forms.

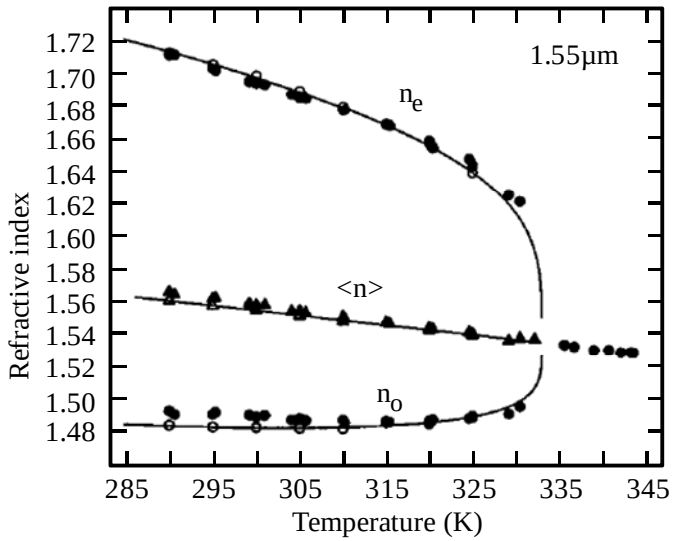

Figure 2.5: Temperature-dependent refractive indices of E7 at λ = 1.55 μm.

In Figure 2.5 the variation of n_o and n_e and <n> versus temperature is reported, at the wavelength of 1.55 μm. It can be observed that the model fits quite well the measurements [78]. In Figure 2.5 the black dots represent the experimental result while the circles represent the interpolation based on Equations (2.23) and (2.24).

2.3. Basic description of azobenzene

In this section we briefly report the basic properties of azocompounds materials, focusing our attention to understand the concepts that we can use to implement azo compounds to obtain all-optical device.

In general the terms "azobenzene" and "azo" are used to refer to the class of compounds that exhibit the core azobenzene structure with different ring substitution patterns.

Azobenzene with two phenyl rings separated by azo (-N=N-) bond, represents the basic constituent of a broad class of azo compounds. Figure 2.6 reports some examples of azomolecules.

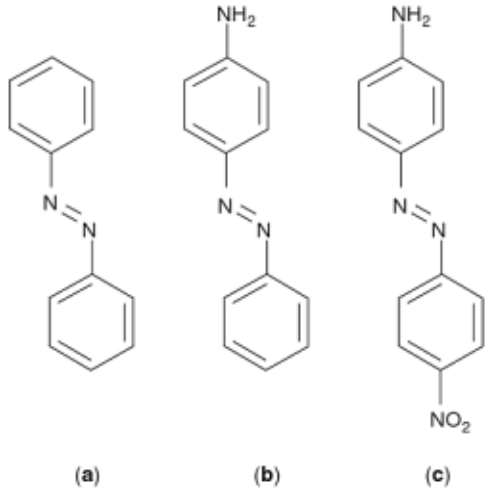

Figure 2.6: (a) azobenzenes, (b) amino-azobenzenes and (c) pseudo-stilbenes.

The azo groups are versatile, chemically stable and mechanically robust molecules. Their strong electronic absorption can be tailored by ring substitution to fall anywhere from the ultraviolet (UV) to visible red regions.

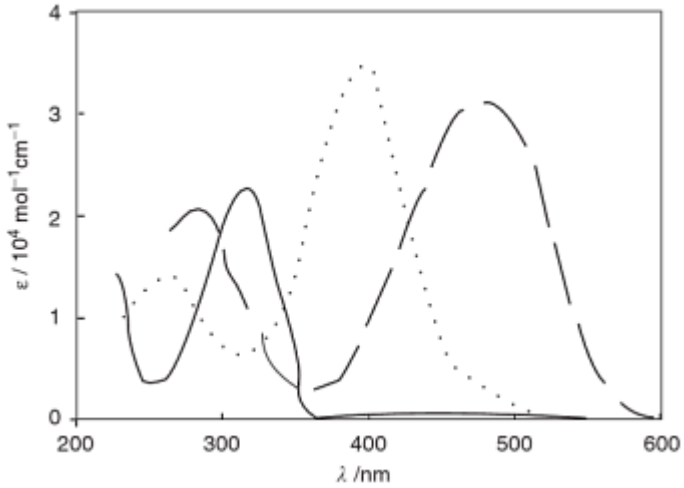

Figure 2.7: Typical absorbance spectra for *trans*-azobenzenes [79].

In Figure 2.7 the azobenzene-type molecules (solid line) have a strong absorption in the UV, and a low intensity band in the visible (barely visible in the graph). The aminoazo-benzenes (dotted line) and pseudo-stilbenes (dashed line) typically have strong overlapped absorption in the visible region.

With an appropriate electron-donor-acceptor ring substitution, the π electron delocalization of the extended aromatic structures can yield high optical nonlinearity. The most important effect, that we use to develop the device proposed in section 4.3, is the readily induced and reversible isomerization about the azo bond between the *trans* and *cis* geometric isomer and the geometric changes that result when azo groups are incorporated into polymers. The light-induced interconversion allows systems incorportating azobenzene to be used in all-optical devices.
The mechanism of isomerization takes place either through a rotation about the N-N bond or through inversion as reported in Figure 2.8:

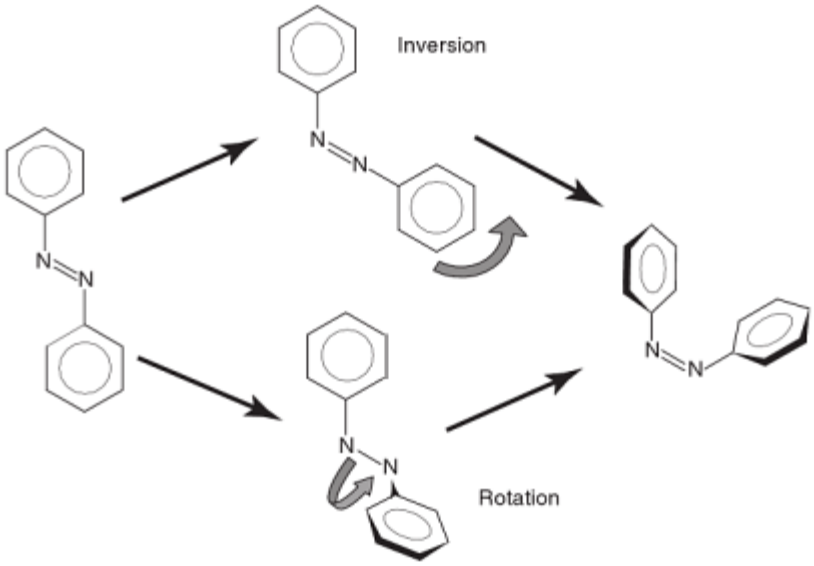

Figure 2.8: The mechanism of azobenzene isomerization proceeds either via rotation or inversion.
(Figure 2.8 is from [79])

Both mechanisms may be competiting, with a different one depending on the particular environment. The availability of the inversion mechanism explains how azos are able to isomerize easily even in rigid matrices since the inversion mechanism has a much smaller free volume requirements than the rotation. Under the irradiation of light with proper wavelength, the isomerization process is characterized by angular-dependent excitation and result in the photoselection of a preferred azobenzene dye orientation, which is perpendicular to the polarization of the light and capable of aligning LC.
If a linearly polarized light of enough intensity passes through pure LC, they reorient parallel to the polarization of light [80]. This reorientation is induced by the anisotropy of the LC's polarizability. By doping the LC with 1% dye, the intensity needed to reorient them is reduced by one or two orders [80], because the torque exerted on the LS by the 1% doped dyes, is one or two orders of magnitude higher than that induced by the optical field on the pure LC.
When irradiation ceases, the initial configuration of the azo compound is recovered due to thermal back isomerization and this optical response was reported to occur in 200 μs. Much work in the field of liquid crystalline azobenzene polymers took advantage of azobenzene photochromism including its effect on the pitch of cholesteric liquid crystals [81], surface assisted liquid crystalline photoalignment [82], optical switching [83] and the photochemical phase transition of guest/host liquid crystal with a photoresponsive azobenzene dopant [84]. In the applications reported in section 4.2, advantages of the last effect are exploited.

3. Tunable optical filters and sensors based on Whispering Gallery Modes

3.1. Introduction

In recent years, dielectric spherical resonators have been extensively studied for their optical properties. In 1912, Lord Rayleigh published "*The problem of the whispering gallery*" [85], in which he demonstrated the very efficient propagation of acoustic waves along the internal surface of the dome of St. Paul's Cathedral in London.

In the same way a non absorbing dielectric microsphere can sustain Whispering Gallery Modes (WGMs) that correspond to the resonance condition for which the light beam travels through total internal reflection (TIR), in proximity of the surface of the dielectric sphere. The light is strongly confined within the microsphere. WGMs are also referred as Morphology Dependent Resonances (MDR) [86]. The first observations of WGM in optics can be attributed to solid state WGM laser. Laser action was studied in Sm:CaF_2 resonator [87]. Recently, WGM resonators have attracted increasing attention because their great potential also in the areas of optical communications systems and biochemical sensing [88].

For practical applications like lasers and filters, the target for researchers and engineers is to obtain a "box" in which there are connected two fibers for the input/output light and two (or more) electric wires to tune the spectral response of the filter.

3.2. Physical basis of microsphere resonators

WGM can be viewed as high angular momentum electromagnetic modes in which light propagates by repeated total internal reflection (TIR) along the internal microsphere surface. After circumnavigating the microsphere, the light wave returns to its starting point in phase to interfere constructively with itself.

Let us consider a microsphere of radius R with refractive index n_1 and a ray of light propagating inside. The ray hits the internal surface with angle of incidence α. If the refractive index of the medium surrounding the microsphere is n_2, the limit angle is defined as $\alpha_L = \arcsin\left(\frac{n_2}{n_1}\right)$.

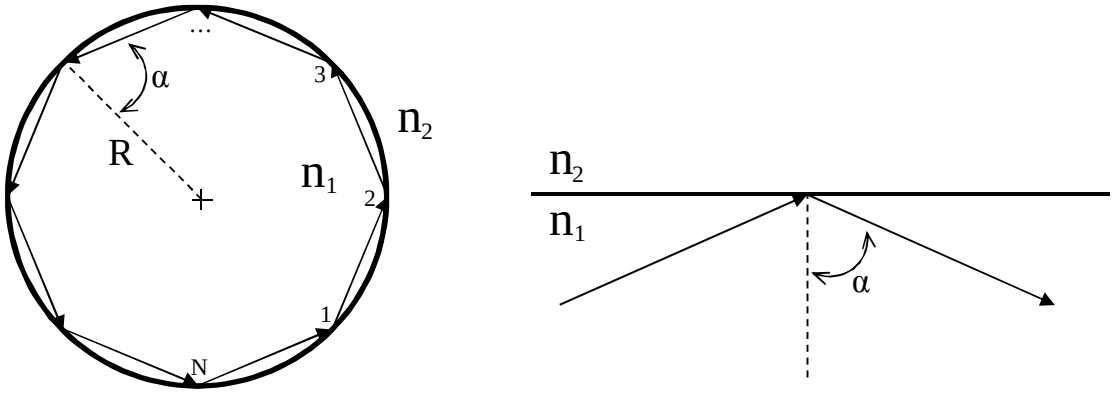

Figure 3.1: (Left) Multiple reflections inside the microsphere, N is the number of reflection for one round trip; (Right) Reflection of a plane wave from a dielectric interface.

The total internal reflection occurs when $\alpha > \alpha_L$. Because of spherical symmetry, all subsequent angles of incidence are the same, and the ray is trapped inside the microsphere. Figure 3.1 leads to the concept of resonance. If $R >> \lambda$, where is the wavelength of the trapped light, the light propagates close to the surface and traverses a distance close to $2\pi R$ in a round trip. If one round trip exactly equals d wavelengths in the medium (d is an integer), then one expects a standing wave to occur. This condition translates into $2\pi R \approx d\lambda / n_2$, where λ / n_2 is the wavelength in the medium. In terms of the size parameter the resonance condition is $2\pi R / \lambda = d / n_2$.

An individual WGM can be identified in terms of three mode numbers: *n*, the radial electromagnetic field component; *m*, the equatorial electromagnetic field component; *l*, the polar electromagnetic field component.

The radial part of a sphere WGM can be described by spherical Bessel functions with an external evanescent tail. The polar (or longitudinal) field dependence follows spherical harmonics, and the equatorial (or latitudinal) field variation is sinusoidal [89]. Specifically, *n* = 1,2,... gives the number of maxima in the radial field pattern of a particular WGM, while *l* = 0,1,... and *p* = -*l*,...,0,...,*l* help define the equatorial and polar field extent. Modes of highest field confinement correspond to high values of *l*, and opposite values of *p* correspond to waves propagating in opposite directions along the sphere equator. *l*-|*p*|+1 equals the number of lobes in the polar field.

In a perfect sphere form, the resonant wavelength of any given WGM is determined only by *l* and *n*, since different radial and/or equatorial mode components correspond to different distances light must travel in order to complete a resonant path around the sphere. In this perfect sphere case, the polar component in WGMs does not influence the resonant wavelengths. This degeneracy condition exists because the field extension in the polar direction is countered exactly by a reduced optical path, due to a lesser circumference at higher latitudes.

The modal structure and spectra of WGMs has been studied using numerical methods [90]. Theory of WGMs resonances in spherical resonators is developed in analogy with quantum mechanical shaped resonances [91] [92]. Orthogonality of WGMs is proven in [93]. This thesis reports a simple method proposed by A. B. Matsko and V. S. Ilchenko **[**94**]** for approximate description of high order WGMs. Let us consider a dielectric sphere with dielectric constant distribution $\varepsilon(R)$, which depends on the radius *R*. The electric field in the sphere obeys the Maxwell equation:

$$\nabla \times \left(\nabla \times E\right) + \frac{\varepsilon(r)}{c^2}\frac{\partial^2 \overline{E}}{\partial t^2} = 0 \tag{3.1}$$

where *c* is the speed of the light in the vacuum. The electric field expression is $\overline{E} = \int_0^\infty d\omega \bar{e}(r)\exp(-i\omega t)$ and equation (3.1) can be rewritten as:

$$\nabla \times \left(\nabla \times \bar{e}\right) - k^2 \varepsilon(r)\bar{e} = 0 \tag{3.2}$$

where $k = \omega / c$ is the wave vector. Equation (3.2) may be solved in terms of TE and TM modes. With keeping in mind that $\nabla \cdot (\varepsilon \bar{e}) = 0$ we write:

$$e = \sum_{\nu,m} \frac{1}{r}\left[\Psi \mathrm{Y}_{\nu,m} + \frac{1}{\varepsilon(r)} \nabla \times \left(\Phi \mathrm{Y}_{\nu,m} \right) \right] \tag{3.3}$$

The radial function $\Psi(r)$ and $\Phi(r)$ stand for TE and TM modes respectively, $\mathrm{Y}_{\nu,m}$ are vector spherical functions with angular number ν and magnetic number m. It is worth noting that modes of an infinite dielectric cylinder may be described in a similar way. Radial field distribution for TE modes is:

$$\frac{\partial^2 \Psi}{\partial r^2} + \left[k^2 \varepsilon(r) - \frac{\nu(\nu+1)}{r^2} \right] \Psi = 0 \tag{3.4}$$

where ν is angular momentum number (ν = 0, 1, 2, 3, . . .). The electric field distribution has dependence $\Psi(r)/r$. Equation (3.4) has an exact solution for a homogeneous dielectric spherical cavity with $\varepsilon(r) = \varepsilon_0 = \text{const}$. Such a solution leads $\Psi(r) = J_\nu + 1/2(kr)$, where $J_\nu + 1/2(kr)$ is the Bessel function of the first kind. The mode spectrum is determined by the boundary conditions $\Psi(r) \to 0$ for $r \to 0$ and 0. For the case of high TE mode order $\nu >> 1$

$$k_{\nu,q} \cong \frac{1}{a\sqrt{\varepsilon_0}} \left[\nu + \alpha_q \left(\frac{\nu}{2} \right)^{1/3} - \sqrt{\frac{\varepsilon_0}{\varepsilon_0 - 1}} + \frac{3\alpha_q^2}{20} \left(\frac{2}{\nu} \right)^{1/3} + O(\nu^{-2/3}) \right] \tag{3.5}$$

where α_q is the q[th] root of the Airy function, a is the radius of the resonator. The expression for TM WGM spectrum looks similar:

$$k_{\nu,q} \cong \frac{1}{a\sqrt{\varepsilon_0}} \left[\nu + \alpha_q \left(\frac{\nu}{2} \right)^{1/3} - \sqrt{\frac{1}{\varepsilon_0(\varepsilon_0 - 1)}} + \frac{3\alpha_q^2}{20} \left(\frac{2}{\nu} \right)^{1/3} + O(\nu^{-2/3}) \right] \tag{3.6}$$

Equation (3.6) gives satisfactory results for the eigenvalues as well as eigenfunctions of the exact problem. The third terms in the right hand side of (3.5) and (3.6) represent the fact that the dielectric WGRs are open resonators. The optical field tunnels outside the resonator's surface at the characteristic length $\approx 1/(k_{\nu,q}\sqrt{\varepsilon_0 - 1})$. The larger the susceptibility ε_0, the smaller is this length and the closer are the solutions to the solution for a closed resonator. The first order approximation for the mode eigenfunctions and eigenvalues may be found from the solution of an approximate equation:

$$\frac{\partial^2 \Psi}{\partial r'^2} + \left(k^2 \varepsilon_0 - \frac{\nu(\nu+1)}{a^2} - r' \frac{2\nu(\nu+1)}{a^3} \right) \Psi = 0 \tag{3.7}$$

where we assume that $\nu >> 1$, $r' = a - r$, $\Psi(0) = \Psi(a) = 0$, and a is the radius of the sphere or cylinder. Comparison of the numerical solution of the exact (3.4) and of the approximate (3.7) shows that the solution of (3.7):

$$\Psi_q(r') = \Psi_{q,0} Ai\left[\left(\frac{2\nu(\nu+1)}{a^3}\right)^{1/3} \frac{r'}{\alpha_q} - \alpha_q\right] \tag{3.8}$$

where $\Psi_{q,0}$ is the field amplitude and k_q is the root of the equation:

$$k_{\nu,q}^2 \varepsilon_0 - \frac{\nu(\nu+1)}{a^2} = \alpha_q \left(\frac{2\nu(\nu+1)}{\alpha^3}\right)^{2/3} \tag{3.9}$$

gives satisfactory results for the eigenvalues as well as eigenfunctions of the exact problem. For instance, it is easy to see that (3.9) gives a close approximation of the first two terms of the decomposition (3.5).

3.3. Light coupling into microspheres

For practical applications of WGR the problem of an efficient, robust and controllable coupling is crucial. The most used coupling system to inject light into a microsphere can be divided into:
a) evanescent-wave based coupling,
b) free beam coupling.
For the applications only the first method is interesting and can be implemented in several ways.
As evanescent wave couplers used to inject light into a microsphere there are prisms, tapered optical filters, angle polished fibers and integrated waveguides. For the practical applications the coupling with an integrated waveguide is the most used method.
Prism-to-sphere with frustrated total internal reflection [95] is the oldest method to couple light in a resonator. Basically it can be considered as the sequence of three phenomena. First, the input beam is focused inside the high-index coupling prism under the angle that provides phase matching between the evanescent wave of the total internal reflection spot and the WGM, respectively. Second, the beam shape is tailored to maximize the modal overlap in the near field. Third, the gap between resonator and prism is optimized to achieve critical coupling [96]. It is not amenable for practical applications due to the presences of the prism.
The tapered fiber [97] [98] is an excellent coupling tool that allows fine tuning of the fiber mode propagation constant by controlling the taper thickness. Fiber tapers are commonly fabricated by heating and at the same time slowly pulling a section of the fiber to form a narrow waist. The appropriate taper waist can be as small as a micrometer in diameter, with the fundamental mode extending significantly into the free space surrounding the taper. The typical total length of the adiabatic tapered section is more than 1 cm. An important limit for practical applications for fiber couplers consists in the fact that the tapered region is very thin and therefore very fragile and easy to deteriorate. In the angle polished fiber technique a fiber end is polished along a specific angle that allows phase matching [99]. The integrated waveguide coupler [100] consists of a properly designed phase-matched surface-channel waveguide whose evanescent field overlaps with the microsphere WGMs. Achieving an efficient coupling is rather critical and requires a careful alignment, but the system is more compact and robust than the fiber taper.

Free-beam coupling: if the main loss mechanism in the resonator is the radiative loss due to curvature, one can couple light into a WGM if it comes in the exact shape that coincides with the emission pattern of leaky WGMs. The problem is in difficulty of excitation and detection of WGMs with larger *Q* using free beam technique [101].

3.4. Quality factor

Among many parameters that characterize the resonator the *Q* is a basic one as reported in the first chapter of this thesis. The *Q* is related to the lifetime of light energy in the resonator mode (τ) as $Q = \omega\tau$, where ω is the angular frequency of the mode. For example, the ring down time corresponding to a mode with $Q = 10^{10}$ and wavelength λ=1.55 μm is 8 μs, thus making ultrahigh-*Q* resonators potentially attractive as light storage devices. *Q* is fundamentally restricted by the radiative emission, which is unavoidable in open dielectric resonators.

The highest *Q* up to the date, $Q = 10^{11}$, is reported in [102]. The highest measured *Q*-factor in amorphous WGM resonators is $Q = 8 \cdot 10^9$ at 633 nm [103]. Theoretical implications from the experimental data for the *Q* in liquid WGRs are about $Q \geq 10^6$ for 20 μm diameter droplets [104]. *Q* measured in liquid WGRs are less than 10^5 [105]. For silica microspheres, *Q* is in the order 10^8 [106]. Quality factors of microring and microdisk WGRs typically do not exceed 10^6. The highest value of Q-factor reported to date for ring resonators is $Q = 2 \cdot 10^6$ [107]. The highest Q-factor reported to date for *unloaded* WGM resonators is 10^8 in air and 10^6 in water for microtoroids [108]. For an isolated (not coupled) WGM resonator, we can identify four independent contributions to its intrinsic Q-factor, Q_o:

$$\frac{1}{Q_0} = \frac{1}{Q_{rad}} + \frac{1}{Q_{abs}} + \frac{1}{Q_{s.s}} + \frac{1}{Q_{cont}} \tag{3.10}$$

Q_{rad} denotes the radiative (curvature) losses. For a given mode the *Q* factor associated with the TM polarization is lower than the value associated with the TE polarization. Q_{rad} increases exponentially with increasing resonator size and the diffraction losses can be considered as negligible with respect to absorption losses for well confined modes. Q_{abs} is associated with absorption and bulk scattering in the material constituting the resonator. It decreases as the losses (α) in the material increases. For example for the undoped silica, with α = 0.1-0.2 dB/km at λ=1.55μm, $Q_{abs} \cong 10^{11}$. $Q_{s.s}^{-1}$ is strictly related at the surfaces inhomogeneities. Q_{cont}^{-1} denotes the losses introduced by surface contaminants during the fabrication process.

If we assume a microsphere made of a low loss material (examples, silica or sapphire) and we neglect the potential imperfection due to the fabrication process, the most important term in equation (3.10) became Q_{rad}. Q_{rad} is the term to investigate to define the total *Q* factor then we can understand why a microsphere *Q* is higher than the *Q* of a ring resonators and disk resonators.

Let us consider a ring resonator, a disk resonator and a microsphere resonator made with the same material and with the same radius (i.e. the external radius for the ring). We neglect the material and

fabrication imperfections. Also the absorption losses are negligible respect to the radiative losses. It means that, from equation (3.10), $Q_0 \approx Q_{rad}$.

(a) (b) (c)

Figure 3.2: Light propagation in (a) ring resonator, (b) disk resonator and (c) microsphere resonator.

A ring resonator needs both the internal and external boundary surfaces for propagation of light. It means an increase of radiative losses. In a disk resonator only the external boundary surface is required for propagation of light. Then the Q for a disk resonator is higher than the Q for a ring resonator. The propagation of light in a preliminary analysis a microsphere resonator, in which the light travel in a region that looks like a disk, as reported in Figure 3.2 (c).

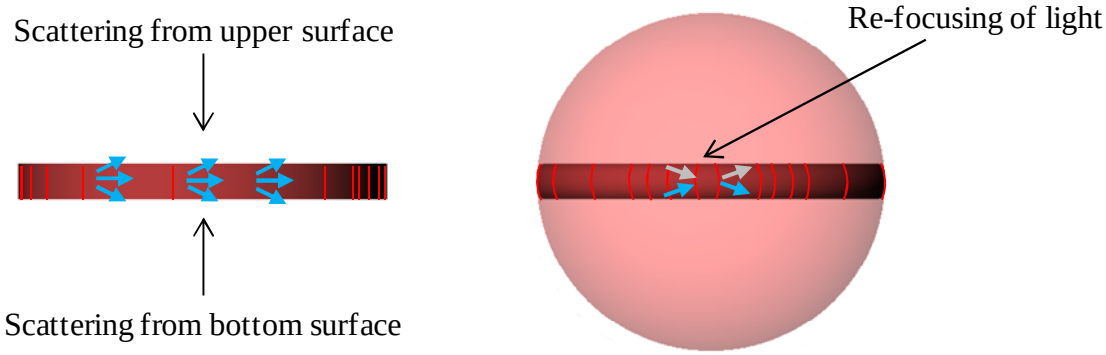

(a) (b)

Figure 3.3: Comparison between propagation of light in a (a) disk resonator and (b) in a microsphere resonator.

In a disk resonator light that travels near the internal surface, is also subject to diffraction phenomena. In that case, along its path, the volumes occupied by the light increases and also the scattering in the upper and bottom surface of the disk play a role in the reduction of the total Q. In a microsphere, the shape of the external boundary surface provides the re-focusing of light that remains confined in a limited region of the microsphere.

The experimental measurement of the Q is generally achieved in two ways:

- The first method is based on equation ($\lambda/\Delta\lambda$). In this situation the wavelength of the input laser is tuned and the correspondent spectral response is collected by a photo-detector. This technique requires an input laser with fine tuning in wavelength ($\Delta\lambda$) and with a very short laser pulse.
- The second method "*Ringdown*" is reported in [54]. In this case the equation used to measure the Q is $Q = \omega\tau$ where τ is the ringdown time. Let us assume that the input wavelength satisfies the resonance condition. In this case the light travel inside the microsphere because of the total internal

reflection. If in a specific time t_o the input light is turned-off, the coupled light still travels inside the microsphere until it expires in t_1 because the absorption of the microsphere and because the scattering. The measurement of $\tau = t_1 - t_0$, used in $Q = \omega\tau$, defines the Q.
It is easy to understand that the ringdown is better to be used in all cases in which Q assumes high values (more than 10^7) because it is much easier to use a long time than a short time. In all other cases the first method as reported before is preferable.

3.5. Whispering gallery mode tuning

The tunability of the WGM resonators can be achieved by several methods. Most common methods are mechanical trimming [109] and temperature tuning [110][111]. Another technique proposed consists in the electrostriction [112]. For mechanical tuning a tuning of 250 *pm* with an applied pressure of 10 *Pa* is reported in for a PMMA hollow microsphere with diameter 1 mm [109]. For the thermal tuning [111] the measured sensitivity is 18 *pm/K* for silica microsphere with diameter 83 *μm* and 14 *pm/K* for silica microsphere with diameter 430 *μm*. For the electrostrinction the tuning reported in [112] is 15 pm with an applied electric field of 250 *KV/m*. For thermal and mechanical tuning the limit are related at the tuning speeds that is in the order of *ms*, and also the low tuning accuracy represent a tuning. The limit of the electrostrinction method is the high values of electric field required to obtain the tuning that make this principle not amenable for practical applications. In [113] a novel mechanism to obtain the tuning of WGM is reported. It consists in the application of liquid crystals as tuning medium. The tuning reported is about 500 pm with an applied voltage of 11 Volt, for a sapphire microsphere with 300 *μm* diameter.

3.6. Tunable filter based on microsphere resonators and liquid crystals

A suitable and never explored before solution to obtain the tuning of WGMs is the implementation of liquid crystals as tuning medium. Liquid crystals (LC) have the advantage of the electro-optical control so they can be included in the "box" and also they have not the limitations in terms of tuning uniformity. The main problem is the integration of a microsphere, LC and a waveguide in a unique system to obtain a mechanically stable electro-optical tunable filter.

3.6.1. Design e numerical analysis

The proposed device is reported in Figure 3.4. It consists of an integrated optoelectronic device based on a sapphire microsphere integrated with a liquid crystal tuning medium to produce a narrowband, electrically tunable filter. The sapphire microsphere is glued over a diffused waveguide in a glass substrate. At the base of the microsphere, a small volume of LC is infiltrated.

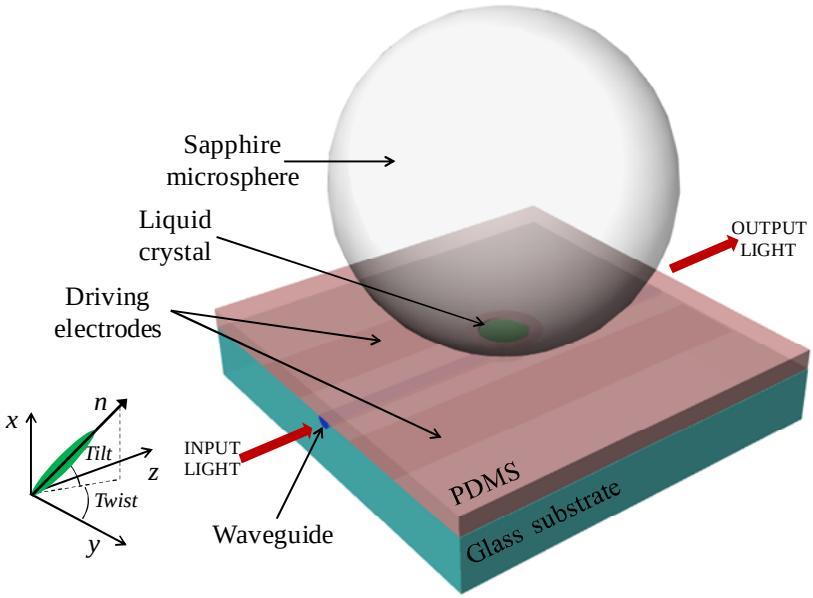

Figure 3.4: Schematic view of the proposed device showing the molecular director **n** and its decomposition into tilt and twist angles.

We consider a microsphere described by equation:

$$(x - x_0)^2 + y^2 + z^2 = R^2 \tag{3.11}$$

The center of the microsphere is raised above the glass substrate by $x_0 = R + d$, where R is the microsphere radius and d is the distance from the substrate to the edge of the sphere. The radius of the cylindrical aperture is:

$$r = \sqrt{2[d(h-R) + hR] - h^2 - d^2} \tag{3.12}$$

where h is the height of the PDMS layer, d=0 µm means that the sphere is in direct contact with the substrate and it is convenient to obtain a mechanically stable system.

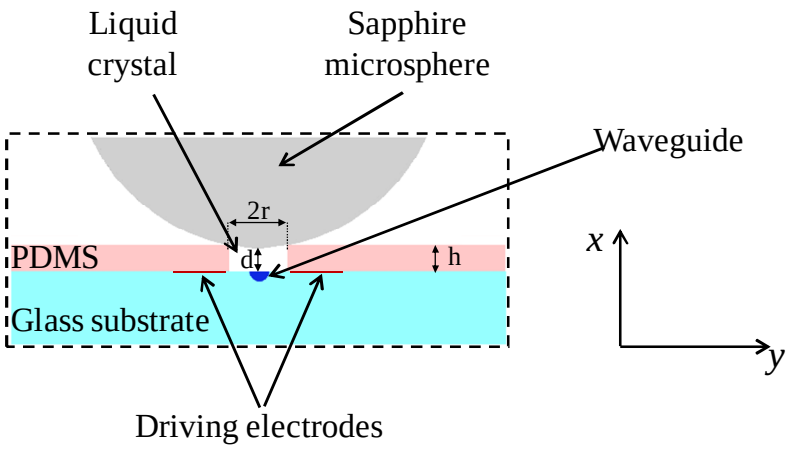

Figure 3.5: Cross section, geometrical parameters.

Figure 3.5 reports the cross section of the structure. It shows that for a fixed value of *h*, the variation of *r* implies the variation of *d*. In particular the following Figure 3.6 shows the relation between the internal radius of the cylindrical aperture (*r*) and the microsphere – waveguide distance (*d*), for a fixed values of microsphere radius (*R* = 150μm) and several values of PDMS thickness (*h*).

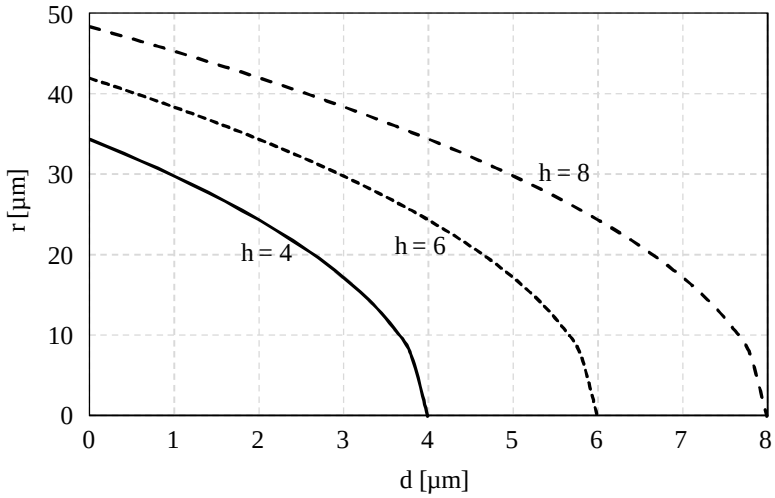

Figure 3.6: Geometrical parameters relation for a fixed microsphere radius R = 150 μm.

In such a structure two different aspects must be studied: the LC reorientation and the propagation of light in the structures. Both aspects depend on the applied voltage (*V*). The LC consider in the proposed device is the E7. For the E7, $n_{\parallel}$=1.689 and $n_{\perp}$=1.5 at 1550 nm. In the rest condition (i.e. *V* = 0), the molecular director $\hat{n}$ is parallel to *z*: it is the LC rest state and is imposed by the rubbing of the Nylon along the *z* direction. Ideally, in the rest condition, $\hat{n}$ is defined with *Tilt* ~ *Twist* ~ 0°. The application of a voltage between the two electrodes implies the formation of an electric field between the two electrodes. To obtain the electric field distribution we solve the Poisson equation in the structures.

The reorientation of the LC is achievable by coupling the minimization of the LC free energy with the solution of the Poisson equation. The free energy involves an elastic terms and an electrostatic term. The elastic term depends by the intrinsic properties of the LC and it is calculated with the Oseen-Frank equation reported in chapter 2, (i.e. equation 2.6).

The refractive index of the sapphire is taken as 1.7 at 1550 nm without considering the negligible birefringence. The computed profiles of the refractive indices are shown in Figure 3.8 for a TE-like input light for four values of control voltage.

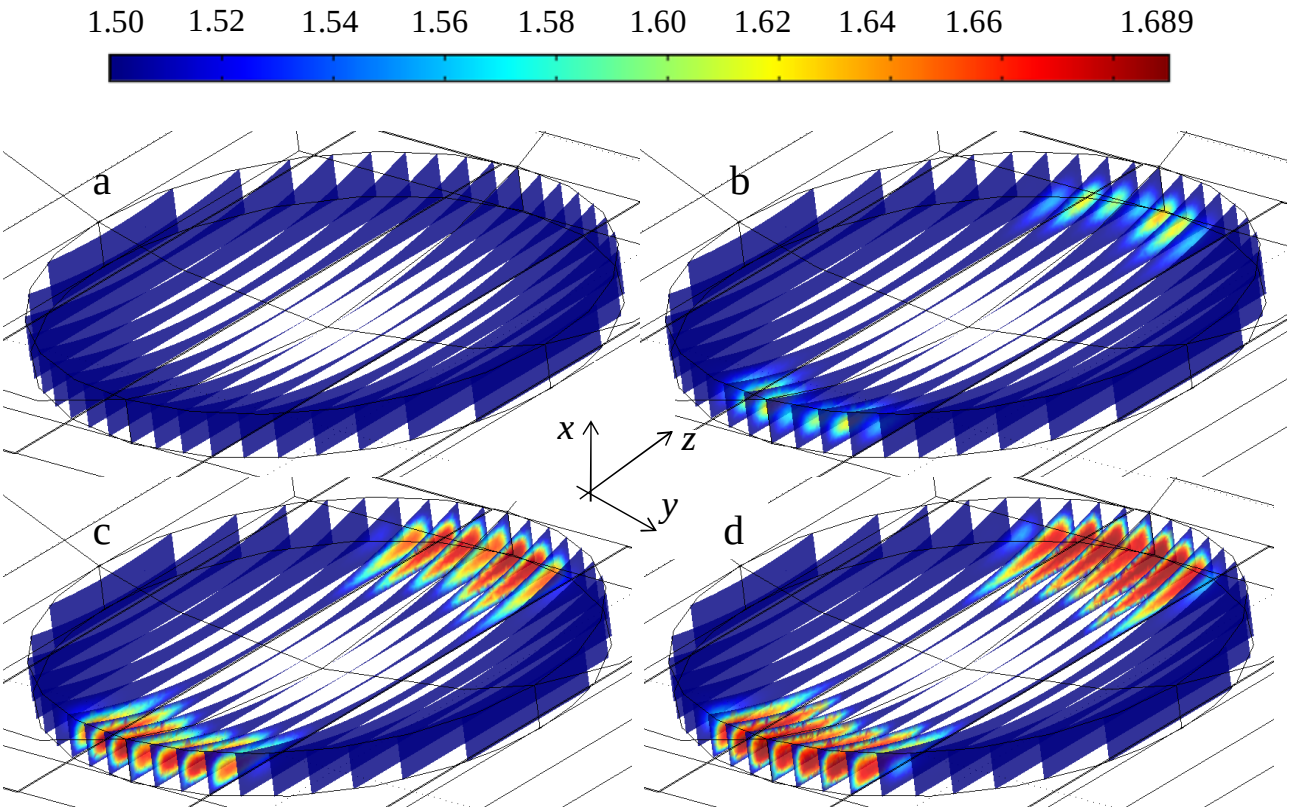

Figure 3.7: Refractive index n_{TE}(Twist) profile calculated profile calculated for the liquid crystals in (a) ground state, (b) 5.5 V, (c) 9.0 V (d) saturating voltage switching (11V). In the colour scale. In the colour scale blue and red represent minimum (1.5) and maximum (1.689) refractive index value for a TE-polarized wave, respectively.

We can recognize two well defined regions for the LC:

region 1, $|y| < t/2$, where $E_y >> E_x$

region 2, $|y| > t/2$, where $E_y << E_x$

t is the electrodes inter-distance.

In the region 1, the electric field mainly acts on the *Twist* angle because the electric field lines are //*y*. It means that for a TE-like input light we can consider the follow expression for the refractive index:

$$n_{TE}(Twist) = \frac{n_{\perp} n_{\parallel}}{\sqrt{n_{\perp}^2 \cos^2(Twist) + n_{\parallel}^2 \sin^2(Twist)}} \tag{3.13}$$

In the region 2, the electric field mainly acts on the *Tilt* angle because the electric field lines are //*x*. It means that a TE-like input light does not observe a refractive index change in the region 2. It is an important aspect of the proposed device because the LC reorientation achieves a high confinement of light only under the equatorial region of the microsphere and it results in a reduction of scattering losses.

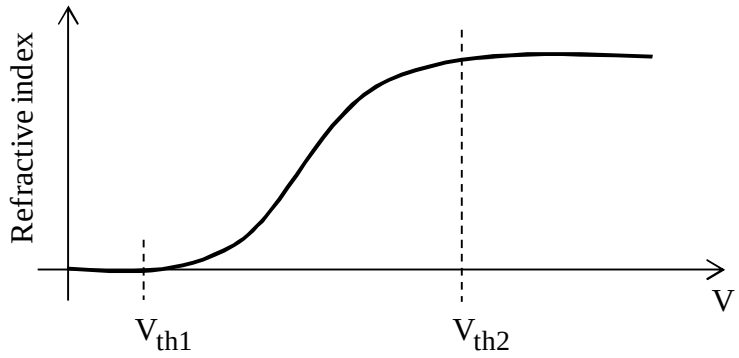

Figure 3.8: Liquid crystal reorientation in una zona specifica per mostrere quanto segue:

Figure 3.8 clearly identifies three zones:
- when the applied voltage is comprised between the ground state and the threshold value V_{th1}, there is not LC reorientation. In this situation the LC elastic forces are higher than electric field forces.
- when the applied voltage is higher than V_{th1}, the LC reorientation starts. There is reorientation of the LC until the applied voltage is V_{th2}.
- V_{th2} is the saturation voltage and over this value is useless to increase the applied voltage because the LC is completely reoriented.

The knowledge of the LC refractive index distribution as a function of the applied voltage allows us to study the problem of light propagation in the devices. It requires the definition of all boundary conditions and the definition of the materials involved in the structures.

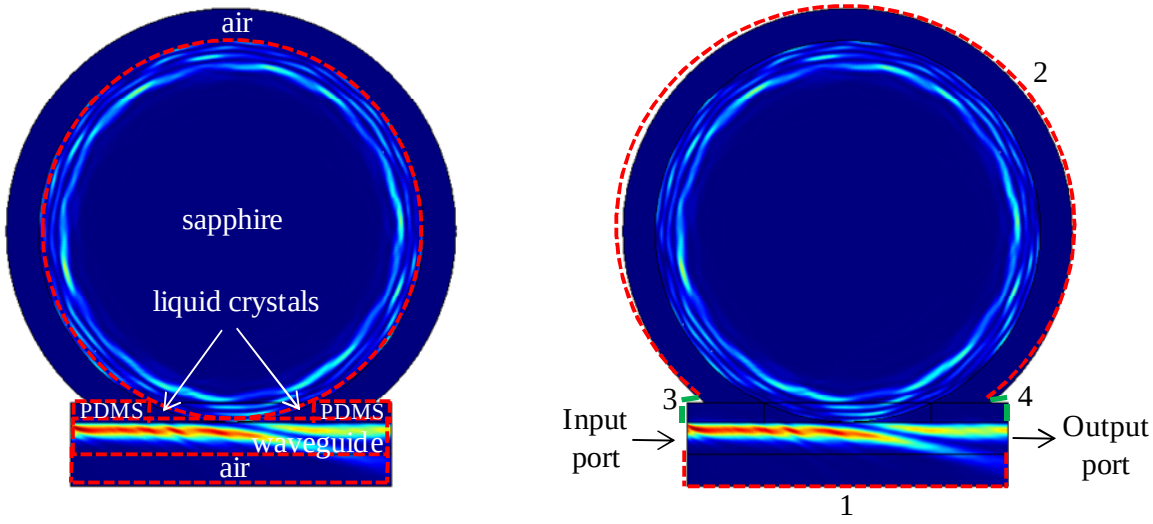

Figures 3.9: boundary conditions and subdomain conditions. The boundaries 1, 2, 3 and 4 are used to know the light power and distribution in each boundary of the device.

Figure 3.9 sketches a 2D geometry of the proposed device to define the optical parameters. The microsphere is made of sapphire with refractive index 1.7 at 1550 nm. PDMS has a refractive index of 1.406 at 1550 nm. The LC refractive index for a TE input light is well described in equation (3.13) and it is a function of the applied voltage as the *Twist* depends on the applied voltage. The waveguide refractive index is defined as following.

Let us call x and y the respective horizontal and vertical axes in the cross section of the glass substrate, we can assume a refractive index profile following the equation:

$$n(x,y) = n_{sub} + \Delta n_{sub}\left[\exp\left(\frac{y}{h_{diffx}}\right)^2 \exp\left(\frac{x+d_{bur}}{h_{diffy}}\right)^2\right] \tag{3.14}$$

where n_{sub} is the BK7 refractive index, Δn_{sub} is the maximum value of the refractive index contrast in the substrate, d_{bur} is the depth of the centre of the channel, and h_{diffx} and h_{diffy} are physical parameters of the depth of K^+ and Ag^+ diffusion, in respectively the horizontal and vertical directions (they are also the standard deviations of the Gaussian). The values of Δn_{sub}, d_{bur}, h_{diffx} and h_{diffy} depend on the technological process. In particular, h_{diffx} and h_{diffy} depend on the process duration and of the diffusion coefficients of K^+ and Ag^+ in BK7. According to the experiment, we have deduced the following parameter values for a 6 µm wide channel, characterized at a wavelength of 1550 nm: $\Delta n_{sub} = 0.04$, $d_{bur} = 0.25$ µm, $h_{diffx} = 2.0$ µm, $h_{diffy} = 2.8$ µm.

As input signal we consider a Gaussian beam with TE polarization. We are interested to know the relation between the Output port and the Input port to understand if the device acts as an optical filter.
Figure 3.10 shows the computed normalized optical intensity in the plane $y = 0$ for the input light that travel which travels from left to right and it is launched a few micrometers under the PDMS–glass substrate interface. This demonstrates that the electromagnetic field resonantly coupled to the microsphere (for d =0 µm) is confined in a few micrometers below the surface.

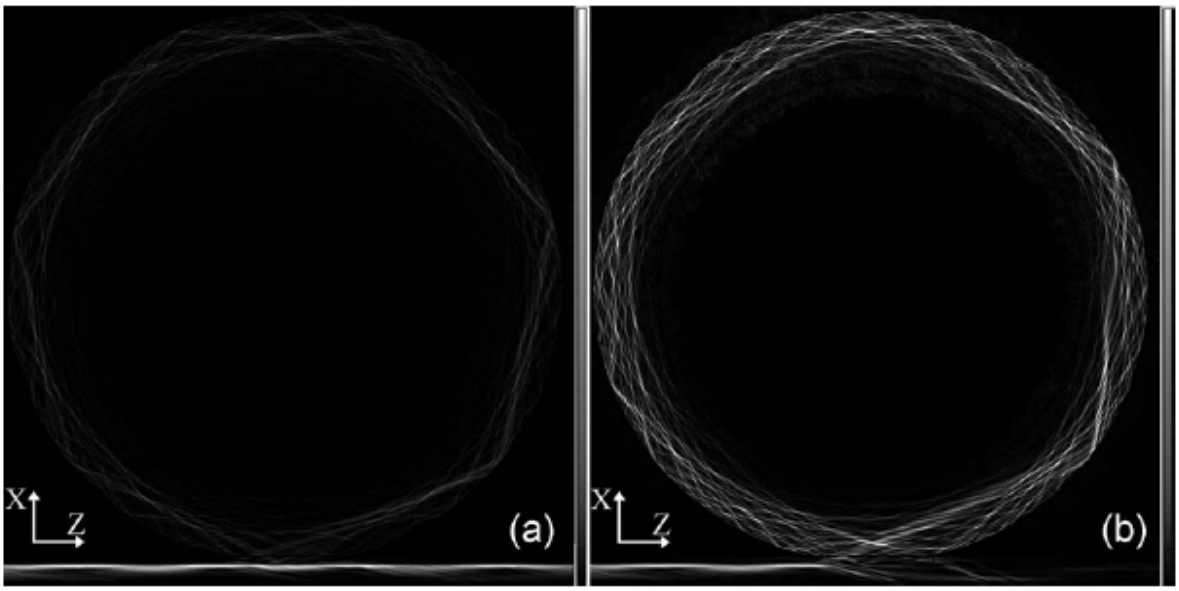

Figure 3.10: Calculated spectra for (Left) OFF-condition resonance and (Right) ON- condition resonance.

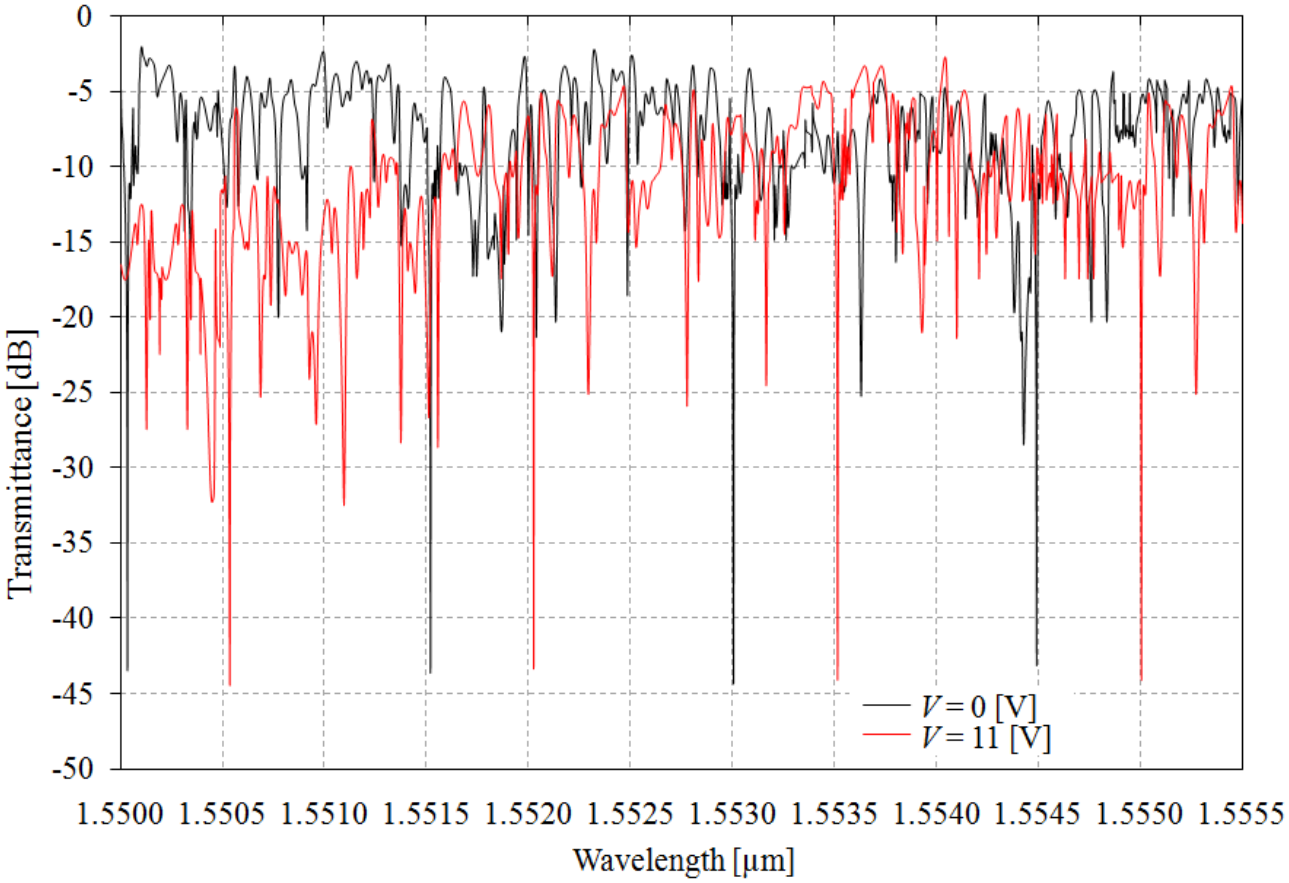

Figure 3.11: Calculated spectral response for two values of applied voltage.

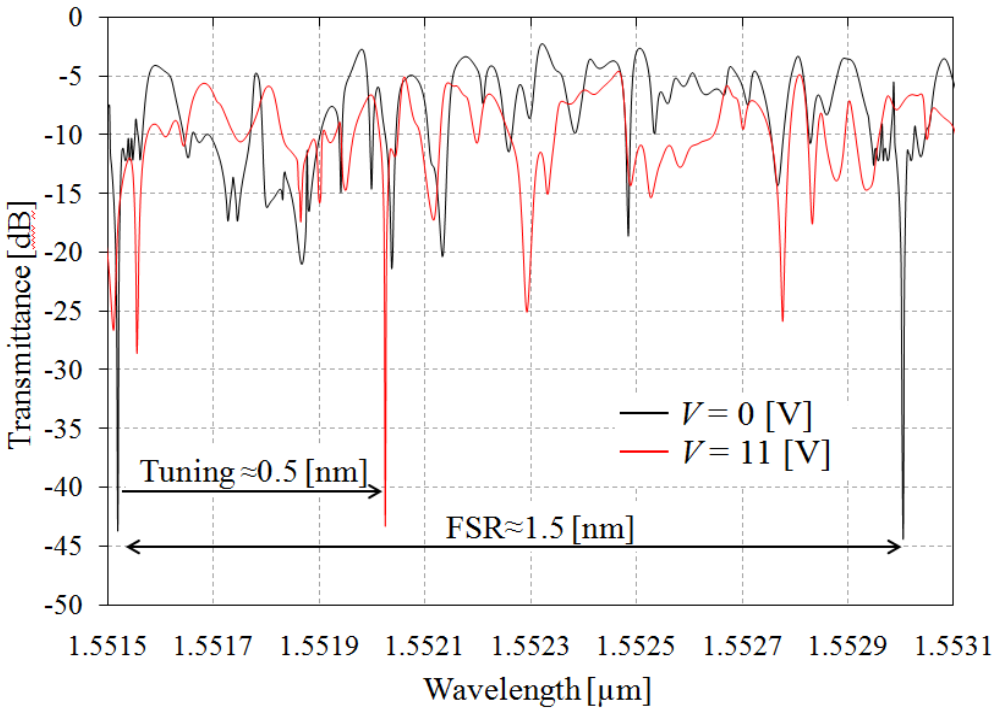

Figure 3.12: Details of the calculated spectral response to define the tuning range and the FSR.

The dips in the transmitted spectra are at approximately −44 dB, with 3 dB linewidths of only 0.2 pm (25 *MHz*), when calculated with a wavelength step as narrow as 0.1 pm.

The *Q*-factor of the filter is approximately $Q \approx 8 \cdot 10^6$ and remains virtually unchanged when the filter is electrically tuned. The redshift of the WGMs is approximately 0.05 nm/V. The shift correlates well with the expected shift, assuming that only 3% of the microsphere surface exposed to the optical field is exposed to a refractive index shift not larger than 10%.
Figure 3.11 and its detail in Figure 3.12, report a tuning range of 500 pm i.e. the 35% of the *FSR*. A way to increase the tuning is to increase the quantity of LC inside circular cavity. By a fabrication point of view it consists in a new definition of the geometrical parameters of the structure. The limit of this solution consists in the increase of LC volume which implies a reduction of the *Q*-factor (see paragraph 3.7). Another solution consists in the fabrication two or more filters in a series configuration as reported in figure 3.13.

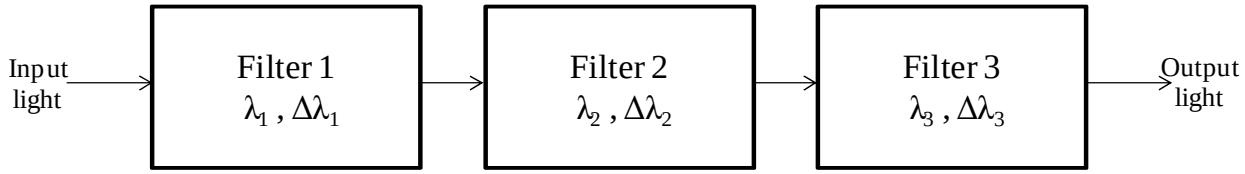

Figure 3.13: Series of optical filters.

The filter *i* (i = 1, 2, 3) when the applied voltage is $V = 0$, has a notch for λ_i. $\Delta\lambda_i$ is the tuning range achievable with the filter-*i*. A way to control the position of λ_i consists in the control of *d*. In fact, as reported in [114], the circulation phase shift is given by:

$$\vartheta = \frac{4\pi n_{eff} R}{\lambda} \tag{3.15}$$

n_{eff} corresponds to the effective refractive index of the mode. n_{eff} depends on the waveguide, microsphere and liquid crystal refractive index and thickness. A thickness variation of the liquid crystal modifies n_{eff}, then modifies the phase shift and therefore the resonant wavelength.
After this configuration, one can fabricate the structure so that the $\lambda_2 = \lambda_1 + \Delta\lambda_1$ and $\lambda_3 = \lambda_2 + \Delta\lambda_2$.
With a proper control of the spectral response of each filter is possible to select a specific wavelength in the full *FSR* without decreasing the *Q*-factor.
The fabrication of a single filter or a series of three filters do not imply the increase of fabrication costs. The microspheres are positioned in the same substrate and the circular aperture to host liquid crystal and microspheres are made in the same PDMS layer.
The results reported above, shows how is possible to integrate the dielectric microspheres and LC by exploiting their respective properties: i) the high *Q*-factor of the microspheres and ii) the electro-optic effect in LC to use it as tuning medium.

3.6.2. Fabrication

The fabrication of the filter requires several materials and several photolithography steps. They are related to the waveguide fabrication and PDMS conformation to obtain the structure as described before. Basically, the fabrication steps to consider are:

a) Waveguide fabrication

b) PDMS definition
c) Nylon 6 deposition and rubbing
c) Microsphere positioning
d) Liquid crystals infiltration

a) Waveguide fabrication consists of immersing the glass substrate in a mixture of fused salts at high temperature. When a glass plate containing sodium ions is immersed in a solution of fused salts containing ions chemically similar to sodium, it occurs an exchange between the two types of ions. The ions in the mixture take the place of their analogue in glass. This phenomenon induces a gradual increase of refractive index, which depends on temperature and duration of the process. Being a diffusion process, the largest refractive index change occurs near the glass surface. The resulting refractive index distribution depends on:

- the type of glass used
- the type of ion and its concentration in the salted bath
- the temperature and duration of the exchange process.

The choice of the glass substrate is therefore a critical factor, as its composition influences all the parameters that characterize the ion exchange process, among others the ion diffusion coefficient and the optical absorption loss [115]. Various glass substrates have been studied, in order to define the ones more suitable to give exchanged ions and to determine the ideal glass specifications [116]. One of the most common and cheapest glasses is soda-lime. This glass is available as plates for laboratories. It has a high concentration of sodium ions, however this concentration changes from one plate to another, and it also has a significant level of metallic impurities. For the device under investigation reported, we use a glass plate produced by Schott and named BK7, whose optical, mechanical and thermal characteristics are reported in Figure 3.14 [117] [118].
The index contrast Δn that can be achieved, between the channel and the bulk substrate, depends on the fabrication process and the salts to be exchanged, the composition of these latter being the major contribution. The different technologies to make single mode waveguides on BK7 substrates include exchanges with: tallium Tl+, potassium K+ or silver Ag+. Nevertheless, although it leads to a high index contrast ($\Delta n \sim 0.1$), tallium is barely used because it is very toxic [119]. Exchange with K+ has been extensively developed and permits to fabricate low-loss waveguides, but it does not yield high index contrast. Eventually exchange with Ag+ can yield high index contrast ($\Delta n \sim 0.13$) and therefore high confinement waveguides. However high concentration of Ag+ in glass also leads to the formation of silver colloidal particles under the edges of the aluminium mask used to define waveguides, which induces a significant increase of absorption loss [120]. The idea is therefore to combine the merits of both Ag+ and K+ exchanges. The technique is called double ion exchange: K+ ions are first implanted, and then Ag+ ions. In this manner, high index contrast waveguides can be fabricated, which have lower propagation loss with respect to single Ag+ exchange. In addition, thanks to the K+ layer, the lateral diffusion of Ag+ is smaller: the waveguide width is thus better controlled and the mask aperture can be enlarged, which releases a technological constraint [121].

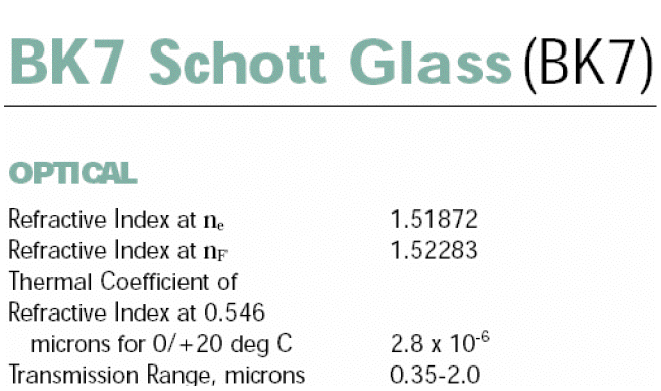

BK7 Schott Glass (BK7)

OPTICAL

Refractive Index at n_e	1.51872
Refractive Index at n_F	1.52283
Thermal Coefficient of Refractive Index at 0.546 microns for 0/+20 deg C	2.8×10^{-6}
Transmission Range, microns	0.35-2.0

Wavelength (*nm*)	Refractive Index *n*
632.8	1.51509
643.8	1.51472
656.3	1.51432
694.3	1.51322
786.0	1.51106

Figure 3.14: Optical and mechanical properties of BK7 glass plate. The optical and physical characteristics are quite good: excellent optical transparency, low dependence on temperature and sufficient mechanical resistance.

To implement the process of ion exchange, a furnace is used: it is a cylinder with an external thermal isolation, and an inner heating resistance. The furnace contains alumina powder. The BK7 sample is located in a beaker filled with nitrate salts and closed by a tap. The resistance heats up the alumina powder. This one is stirred by compressed air, in order to homogenise temperature in the whole volume of the furnace. A temperature controller permits to regulate the process with an accuracy of ±1 °C, the maximum temperature being 600°C.

We used BK7 glass plates of dimensions 5 × 5 cm and 1 mm thickness. The glass plates are first washed in a mixture of soap and deionised (DI) water, under ultrasound. They are cleaned with DI water and dried. We have chosen is the double ion exchange: K^+-Na^+ and Ag^+-Na^+. The process steps are the following:

- The BK7 glass plate is immersed in a potassium nitrate bath (KNO_3) and put in furnace at a temperature of 400°C. During this step, the ions K^+ (present in the salt) and Na^+ (present in the glass plate) are exchanged and K^+ ions thermally diffuse in BK7. The glass refractive index is increased, but not enough to enable the fundamental optical mode. After 80 min, the glass plate is taken out of the furnace and left to cool down to ambient temperature. Then, it is rinsed in DI water (to wash away from the glass surface any remaining salt) and dried. As this step is a diffusion process, it can be observed that temperature is fundamental and has an influence on the index contrast and on the depth of the exchanged zone. If the furnace temperature is not stabilised or if the controller is not accurate, the waveguide reproducibility may be affected.
- A 200 nm thick aluminium film is evaporated on the glass plate. After positive photoresist spin coating, the waveguides are photolithographically defined. Aluminium is wet-etched, leaving the waveguide location open.
- The glass plate is immersed in a mixture of silver nitrate $AgNO_3$ and sodium nitrate $NaNO_3$, and put in furnace at 320°C. During this step, the ions Ag^+ (present in the salt) and Na^+ (still present in the glass plate) are exchanged. The Ag^+ ions diffuse in the glass, in the zones not protected by the physical aluminium mask. The temperature during this step is lower than during the K+ exchange, so that the potassium layer can remain practically unchanged. After 5 hours, the sample is taken out of the salt bath and is left to cool down at ambient temperature in a sufficient time. Afterwards the sample can be rinsed. A thermal shock of the glass plate covered with a metal film could indeed break the sample. Eventually, the maximum of Ag+ concentration will be located slightly below the K+ region, giving rise to embedded optical channels.

- The sample is placed a third time in the furnace, for 24 hours at 300°C. This step is called "annealing" and it aims to give thermal energy to Ag+ ions in order to reach a more uniform distribution of dopant (and subsequently of refractive index). The temperature is lower, so that annealing affects Ag+, and not K+. In practise, this final step is useful to reduce significantly the propagation losses due to silver colloids. We have indeed measured a decrease of the losses from 4 dB/cm without annealing, down to 0.5 dB/cm with annealing.

It should be noticed that after the second ion exchange (Ag+ - Na+), the aluminium mask should be removed, only leaving markers for fiber coupling. Actually in our case, we partially remove the aluminium layer because we want to use it to define coplanar electrodes for the further device. Each sample is composed of eight optical channels, 6 µm wide, and a set of calibration waveguides. This latter is made up of a series of optical waveguides of different widths: from 2 µm to 12 µm. This set is used to check light propagation in a variety of waveguides. In order to be optically characterized, the sample shall be sawn perpendicularly to the channels. In practise, the cut edges will be always somewhat rough, which will generate coupling losses by scattering. A way to refine these interfaces is to polish the facets and therefore to reduce the size of the glass chirping. Polishing is a mechanical process that can be done manually or automatically. It consists of a series of rubbing of the side facets of the sample, on an abrasive sand paper, so that the resulting smoothness and planarity of the facets can be greatly increased (typically the roughness is less than one micrometer). As the double ion exchange process is a diffusion process, the refractive index distribution in the channel should be Gaussian-like [122].

Propagation of infrared laser light launched at one end of the waveguide by butt coupling is observed for a channel with a length of 2 cm. A pigtailed polarization controller is connected to a single mode optical fiber, terminated with a cleaved face to couple light into the optical channel waveguides. The polarization controller consists in a series of three waveplates, placed between two aligned fiber collimators, which allow to rotate a linear polarization of the light without power variation. After calibrating the input light by means of a polarizer before coupling the cleaved fiber with the waveguides, it is possible to measure the state of polarization of light injected into the waveguides. The optical waveguide output is collected by a 10X microscope objective and focussed on an infrared vidicon camera. Figure 3.15 reports the image of the output near-field. The guided light shows a good optical confinement with estimated optical losses below 1 dB/cm.

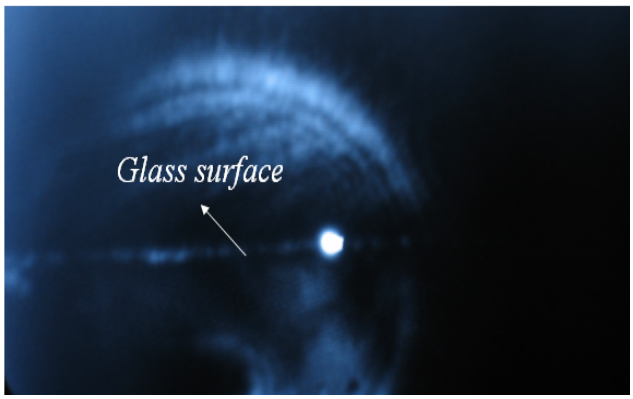

Figure 3.15: Picture of the waveguide output (1550nm) focussed on an infrared camera.

b) The PDMS is a suitable material in optics due its low refractive index (1.406 @ 1550nm [123]). There are several methods to integrate and geometrically define the PDMS in an optical device. The most common methods are:

- The mold technique [124], in which the PDMS is deposited in a mold previously fabricated. After the deposition the PDMS is mechanically removed from the mold. In this way the PDMS assumes the complementary shape of the mold. The mold technique is also suitable for high definition nanostructures but it is not directly applicable for the realization of our device.
- The classic UV-curing of PDMS requires a high UV energy and it is not amenable for mass production. Another limitation is related at the bonding between the substrate covered with PDMS and the mask used for the photolithography definition.

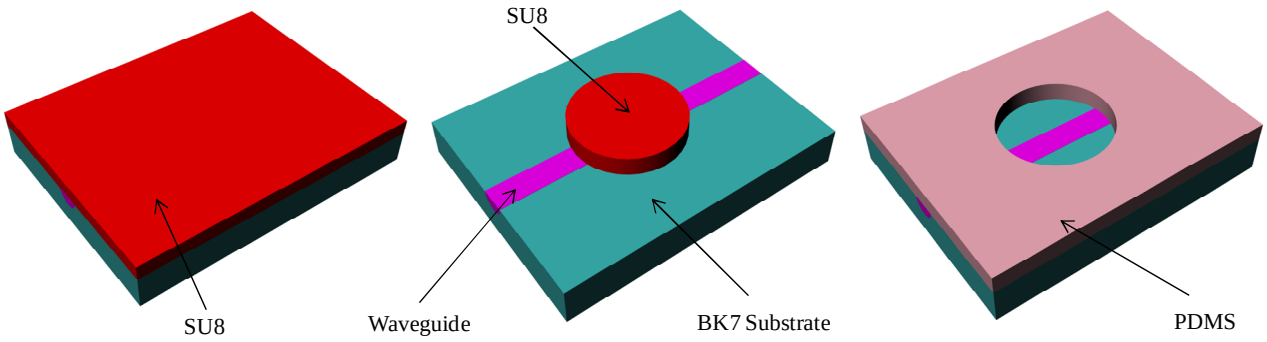

Figure 3.16: Basic fabrication steps.

Figure 3.16 describes some steps to fabricate the proposed device. A glass substrate is well cleaned with IPA (isopropyl alcohol) to remove all dust particles. The substrate is covered with SU8 [125] (red colour). SU8 is a high contrast, epoxy based photoresist designed for micromachining and other microelectronic applications, where a thick, chemically and thermally stable image is desired. SU8 has been widely used by MEMS producers. In particular for the fabrication of the device we use the SU-8 3000 that is ideally for near vertical sidewalls in very thick films.

For example to obtain a SU8 thickness of 8 µm, it is spinned at 1000 rpm for 30 seconds. Before the exposure UV exposure a soft bake at 95°C for 4 minutes is required. The exposure is performed for 20 seconds with exposure energy density of 130 mJ/cm^2. The development for 3 minutes and the post exposure bake for 3 minutes at 95°C ensure the right definition of the SU8 features. Figure 3.17 reports the structure in SU8.

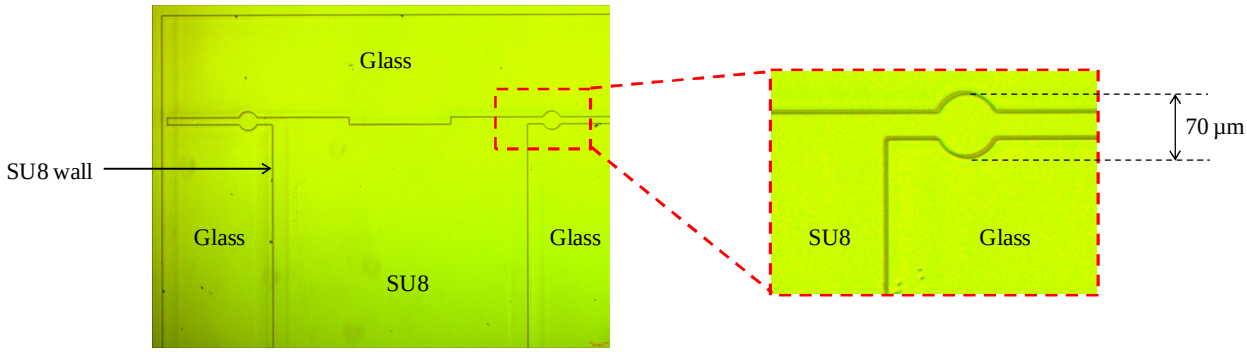

Figure 3.17: SU8 definition.

The substrate including the SU8 structures is then covered with another glass with the same dimension of the substrate. The two glasses are blocked with two pliers and the lateral apertures are infiltrated with PDMS. In this condition the distance between the two glasses depends on the SU8 thickness and also the PDMS thickness depends on the SU8 thickness. With a mechanical action the two glasses are separated obtaining the PDMS structure as reported in Figure 3.17.

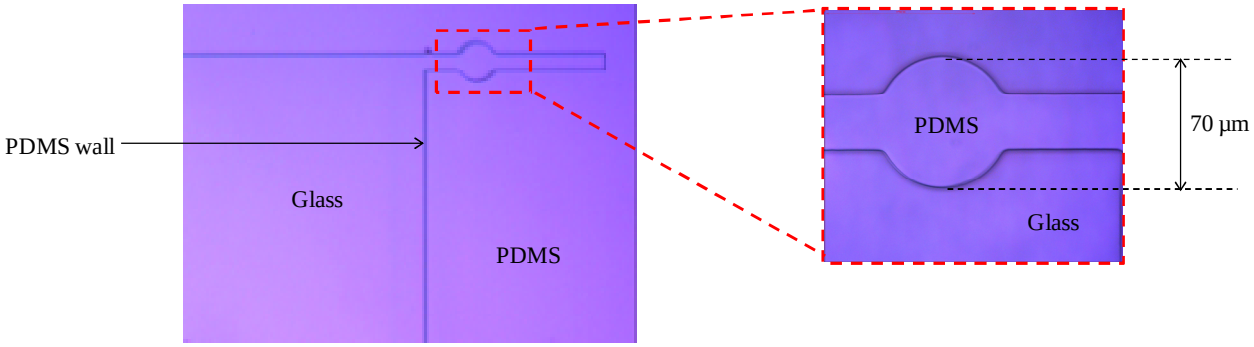

Figure 3.18: PDMS definition.

c) To obtain a precise LC reorientation, the structure reported in Figure 3.18 is covered with a thin layer of *Nylon 6*. A 50 nm thick layer of *Nylon 6* is obtained by spinning a solution of 0.5% wt/vol in trichloroethanol at 4000 rpm for 40 seconds. *Nylon 6* is then crystallized by thermal treatment in air at 160°C for 4 h. Afterwards a mechanical rubbing of *Nylon 6* was made by using a velvet cloth to promote planar homogeneous alignment of the LC.

d) The microsphere is manually positioned over the PDMS circular aperture. Practically speaking a microsphere is positioned over circular aperture using the tip of an optical fiber. When the microsphere is correctly positioned, it is glued on position by means of UV-curable glue. The glue does not affect the electromagnetic problem because it is positioned in a region far from the light path.

e) The infiltration with LC is the last operation. Figure 3.19 shows the LC infiltration procedures.

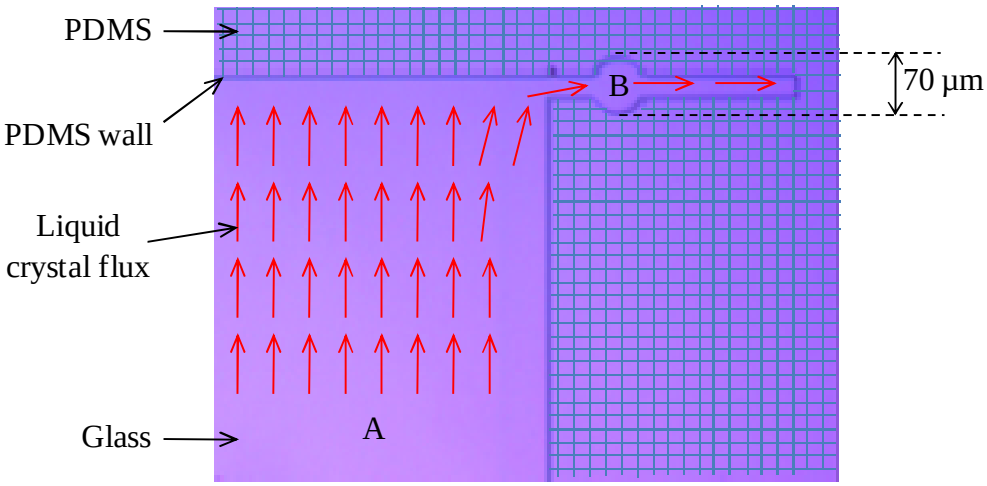

Figure 3.19: LC infiltration.

The filling is realized in the vacuum. The LC is initially positioned in the point A and for capillarity it flows in the region comprised between the microsphere and the waveguide, B. The air in the area B is pushed out by the LC.

3.7. An optofluidic sensor based on microsphere resonators

This section reports about an optofluidic sensor based on a microsphere resonator. Thanks to the nanofluidic design this sensor could operate with tiny and well controlled volumes of measuring fluid, down to 1 pl. We introduce a figure of merit, which clarifies the effect of high *Q* resonators and allows us to compare different geometries of the device, choosing the optimal one according to the range of the refractive index of the measurand fluid and the volume available for the measurement.

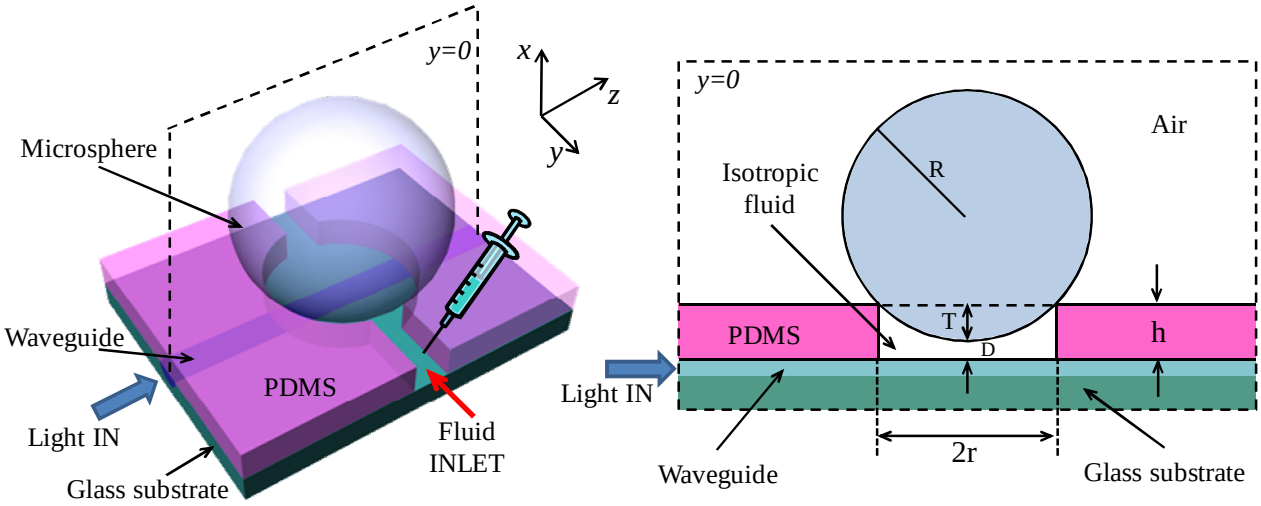

Figure 3.20: Device structure and definition of the geometrical parameters.

The proposed device is illustrated in Figure 3.20. It consists of a microsphere positioned over a double ions exchange waveguide. The dispensing of the measurand fluid is here schematically represented by a syringe, though microfluidic systems made with polydimethylsiloxane (PDMS) and capable of dispensing sub-nanoliter volumes have been demonstrated [126]. PDMS is one of the preferred materials for optofluidics [127] due to its elasticity, optical transparency, biocompatible surface chemistry [128] and low cost process by several techniques, including soft lithography [129]. A simple O_2 plasma activates the surface allowing adhesion to other PDMS or glass and resulting in sealed devices. Furthermore, its low refractive index (1.406 @ 1550 nm) makes it an excellent optical cladding for glass waveguides. For our common fabrication process, once covered by PDMS, these waveguides have an effective refractive index of $n_{eff} \approx 1.5089$ for the fundamental TE mode, as computed by using a mode solver. Small variations of the effective refractive index occur for a set of relevant covering liquids with refractive index fluid in the 1.3-1.53 range, but as a general rule, guided propagation in the waveguide results only for measurand fluids with $n_{fluid} < n_{eff}$. Excellent resonant coupling (i.e. critical coupling) into the sphere and low loss for non-resonant wavelengths (i.e. undercoupling) is obtained when $n_{fluid} < n_{eff} < n_{sphere}$. When nfluid exceeds neff, optical modes leak out of the waveguide, show poor coupling to the spherical resonator and high optical losses, which limit the effective interaction length. Hence, in order to be

able to measure a broader range of fluids, we focus the current study to commercially available sapphire microspheres. A cylindrical aperture in the PDMS supports the microsphere and controls its distance D from the waveguide and, at the same time, defines the confining cavity and the inlets and outlets for the injection of the measurand fluid. The microsphere is positioned over the apertures and glued in place for a stable vibration-free arrangement. D is related to the PDMS thickness (*h*) and the cylindrical aperture radius (*r*). The phase matching coupling condition for a light beam propagating in the waveguide and the WGMs in the microsphere depends on the refractive index of the fluid. The injection of an isotropic fluid with $n_{fluid} > 1$ in the cylindrical cavity, results in an apparent increase of the effective size of the microsphere. Hence the propagation pathway of the photons inside the microsphere increases. This increase is measured in the spectrum transmitted by the waveguide as a shift in the resonance peak wavelength to longer wavelengths. We consider a microsphere described by the equation:

$$(x + x_0)^2 + y^2 + z^2 = R^2 \tag{3.16}$$

The centre of the microsphere is raised above the glass substrate by $x_0 = R + D$, where R is the microsphere radius and D is the distance from the substrate to the edge of the microsphere. Thus, the radius of the cylindrical aperture is:

$$r = \sqrt{2[D(h - R) + hR] - h^2 - D^2} \tag{3.17}$$

We consider a choice of values for PDMS thickness and limit our study in the case of D = 0, i.e. $T = h$, where T is the height of the spherical cap as this condition determines the minimum fluid volume for any combination of R, r and h. Furthermore, the condition $T = h$ implies that the sphere is in physical contact with the waveguide which makes the sensor less sensitive to vibrations that strongly limit practical usability of WGM resonators coupled by tapered fibers. Hence, the Equation (3.17) becomes:

$$r = \sqrt{2hR - h^2} \tag{3.18}$$

The surface (S) of the microsphere in contact with the isotropic fluid is:

$$S = 2\pi RT \tag{3.19}$$

and the fluid volume inside the cylindrical cavity is:

$$V = \pi r^2 h - \pi h \frac{3r^2 - h^2}{6} \tag{3.20}$$

The effect of the fluid on the optical properties of the structure is defined at design stage by geometrical overlap of the optical mode in the waveguide and in the sphere and by the length of interaction. This overlap is dynamically varied by the injected measurand fluid, which somehow

behaves as a optical matching fluid. As the fluid covers only a fraction of the microsphere, we have two options for defining a cover factor to help comparing different geometries. In Figure 3.21 we plot the effect of the radius and PDMS thickness on the fraction of circumference (*C*%) and fraction of area (*S*%) of the sphere and fluid volume.

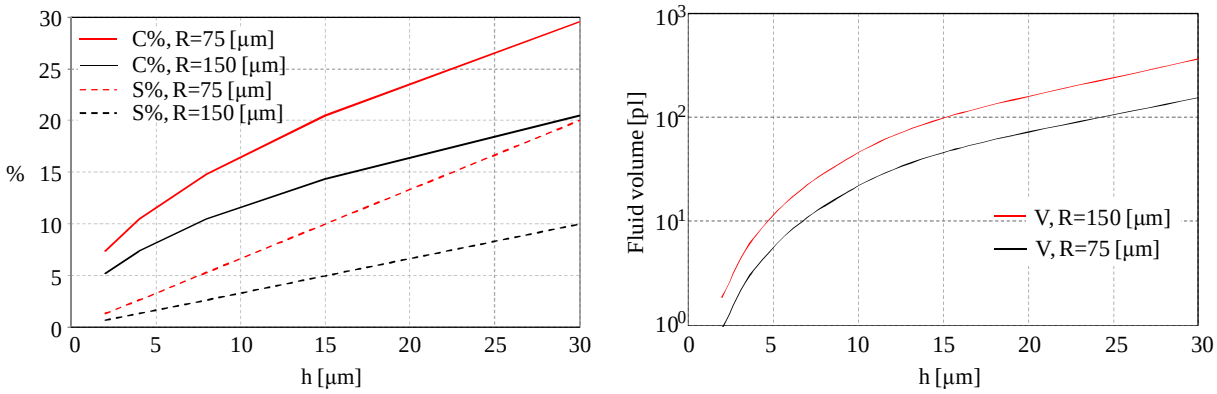

Figure 3.21: (Left) Percentage of microsphere circumference (C%) and surface (S%) in contact with the isotropic fluid which affects the effective interaction length, Leff , and (Right) total fluid volume inside the cavity.

The corresponding volume occupied by the measurand fluid remarks that volumes as low as 1 pl, a yet unprecedented value for a micro-fluidic sensor, are possible. In the following we systematically study the effect of the fluid volume on the performance of the sensor.

3.7.1. Design and numerical analysis

The model used to study the sensor is similar to the previous one used to study the tunable optical filter in section 3.6. However in this case we do not need to consider the reorientation of LC, so that the model consists of a pure electromagnetic problem in which the fluid in the cavity is to consider as an isotropic material with a proper refractive index.

The behaviour of the device is studied by the Finite Element Method (FEM), implemented in COMSOL Multiphysic, as a function of nfluid for microspheres with R =75 µm and R = 150 µm to understand the effect of their radius. The analysis is done in the frequency domain by sweeping the wavelength of a Gaussian optical field with TE polarization which is coupled to the diffused waveguide, thus mimicking butt-coupling from an optical fiber used in the experimental conditions. We have chosen for a frequency domain analysis, as this allows to finely follow the narrowband resonances of WGM. In Figure 3.22 we plot the computed normalized transmission for seven values of refractive index for two scenario cases, (a) R = 75 µm, h = 2 µm and (b) R = 150 µm, h = 4 µm as this combination results in the same exposed surface S%. When n_{fluid} is comparable or larger than $n_{eff} = n_{eff}(n_{fluid})$, optical power is progressively transferred to the liquid and scattered, which results in a decrease of the *Q*. This makes the identification of the peak shift less precise.

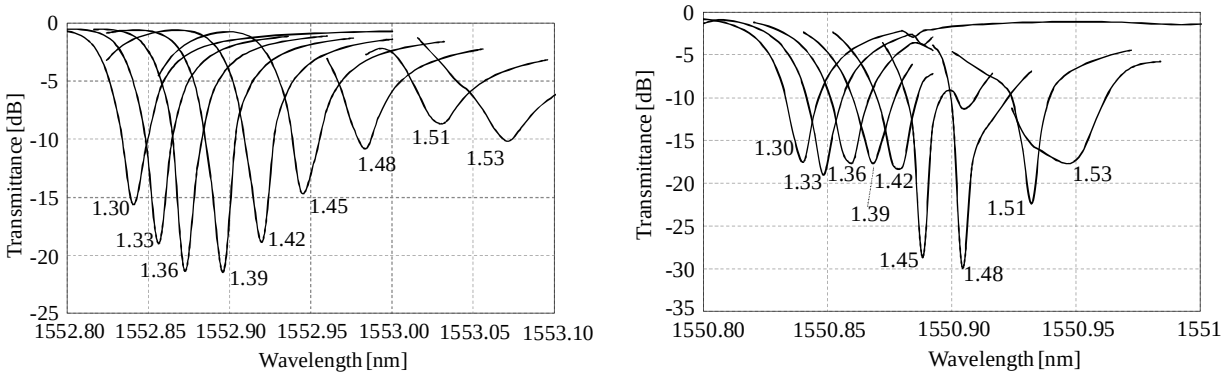

Figure 3.22: Computed normalized transmission for seven values of refractive index for (a) R = 75 μm and h = 2 μm and (b) R = 150 μm and h = 4 μm.

From the full data sets, in Figure 3.23 we summarize the computed shift of the peak when fluids with larger refractive indices are injected for different geometries and fluid volumes.

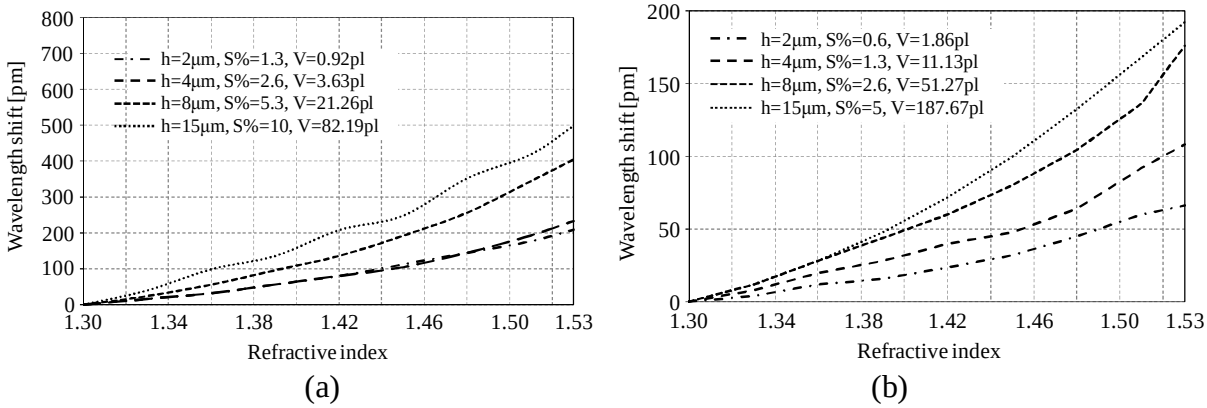

Figure 3.23: Computed peak shift as a function of refractive index values of flowing fluid. For (a) R = 75 μm and (b) R = 150 μm. Larger cavity determines larger shifts, but at the expense of larger fluid volumes.

Our results in Figure 3.23 follow the trend described by equations (3) and (4) in Ref. [130]. Those equations indicate that the resonance shift strongly depends on the field intensity at the sphere surface. The increase of the refractive index of the fluid inside the cavity enhances the amplitude of the evanescent field that senses the fluid. As expected, Figure 3.23 shows that the larger the surface of the microsphere in contact with the fluid, the larger the peak shift. However, this also implies an increase of the measurand fluid's volume. While sensitivity is often defined as $S = \frac{\partial \lambda}{\partial n}$ [131], this does not take into any account any constraint on the volume of the measurand fluid. Hence, to study quantitatively this behaviour of our device, we define its sensitivity per unit volume $S = \frac{1}{V}\frac{\partial \lambda}{\partial n}$, here approximated for our discrete data set as the normalised centred difference $S_V = \frac{1}{V}\left(\frac{\lambda_{k+1} - \lambda_{k-1}}{2\Delta n}\right)$ and plot it in Figure 3.24.

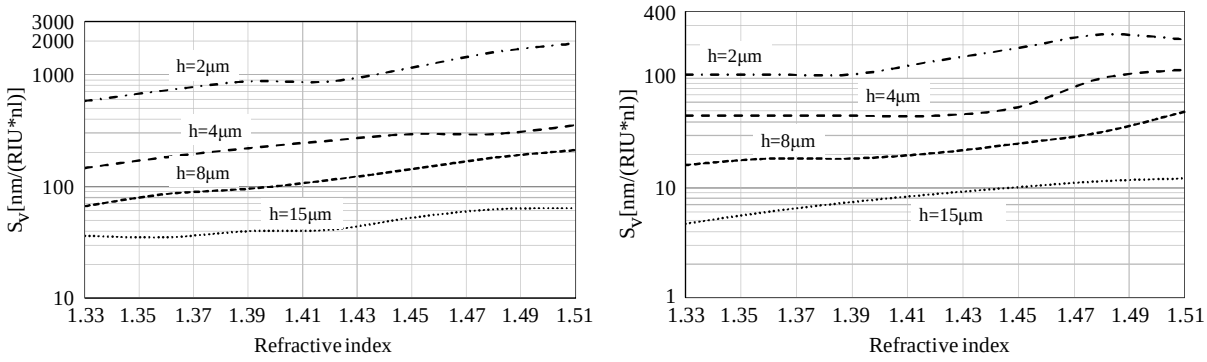

(a) (b)

Figure 3.24: Sensitivity SV curves for (a) 75 µm and (b) 150 µm radius. In all cases, sensitivity slightly increases with the refractive index due to better phase matching of optical power inside the resonator.

From figure 3.23 one would be tempted to conclude that smaller spheres are more sensitive. However one must also keep into account the resolution and limit of detection in the measurement of the resonant wavelength λ_R. This is done in the frequency domain by "sampling" the transmittance curve *vs* wavelength with a stable tunable laser with a bandwidth much narrower than the bandwidth of the resonator. Commercially available tunable lasers in the near 1.55 µm telecom window have a bandwidth of ≈100 KHz (0.8 fm at 1550 nm) and a comparable resolution $\delta\lambda$ in the tuning. The measure of the peak shift is ultimately done by measuring variations in the transmitted power. Variations of power is measured with a resolution normalised by *Pmin*, the transmitted power at the resonant wavelength. To estimate the minimum detectable power variation δP measureable at the output of the device, we write the transmitted power *vs* wavelength as the simplest parabolic approximation of the Lorentzian shape, $P = a(\lambda - \lambda_R)^2 + P_{\min}$. The parabolic interpolation is defined, solving the system of equations:

$$\begin{cases} P_{\min} = a\lambda_R^2 + b\lambda_R + c \\ \dfrac{P_{\min}}{2} = a\left(\lambda_R - \dfrac{\Delta\lambda}{2}\right)^2 + b\left(\lambda_R - \dfrac{\Delta\lambda}{2}\right) + c \\ \dfrac{P_{\min}}{2} = a\left(\lambda_R + \dfrac{\Delta\lambda}{2}\right)^2 + b\left(\lambda_R + \dfrac{\Delta\lambda}{2}\right) + c \end{cases} \tag{3.21}$$

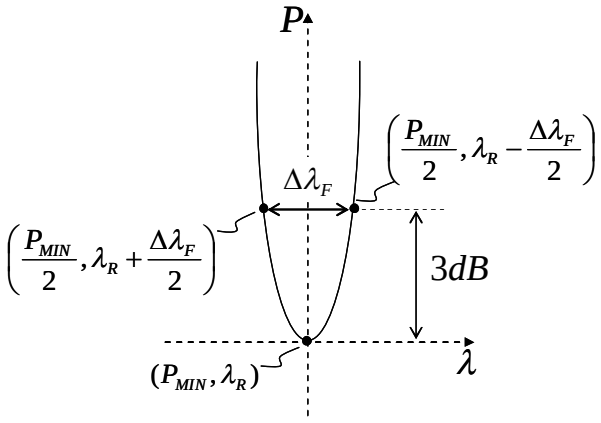

Figure 3.25: Parameter definition for the system of equations 3.21.

$\delta P/P_{min}$ is directly related to $Q = \frac{\lambda_R}{\Delta\lambda}$ through the relationship $\delta P/P_{min} = 8Q^2 * \delta\lambda/\lambda R$. As one would expect, larger values of *Q*, typical of larger spheres, ease the detection of small wavelength changes as the *Q* "amplifies" the power variation in the detector. However, for the same value of the PDMS thickness *h*, smaller spheres expose a larger percentage of circumference and surface to the measurand fluid, thus somehow counterbalancing the smaller *Q*. Smaller values of *Q* result also in easier shift of the resonant frequency, thus in a more sensitive readout. To quantify these opposing effects in small and larger microspheres and optimise the design of the microfluidic sensor for a set of experimental constraints such as available fluid volume or refractive index range, we here define the "amplified" sensitivity per unit volume as a figure of merit $S_Q = 8 * Q^2 * S_V$. This takes into account the sensitivity as "amplified" by the resonant multipass effect. We plot this as a function of refractive index in Figure 3.26. This figure of merit allows us to identify the best design parameters of the microfluidic resonator for a range of values of the refractive index of the measurement fluid.

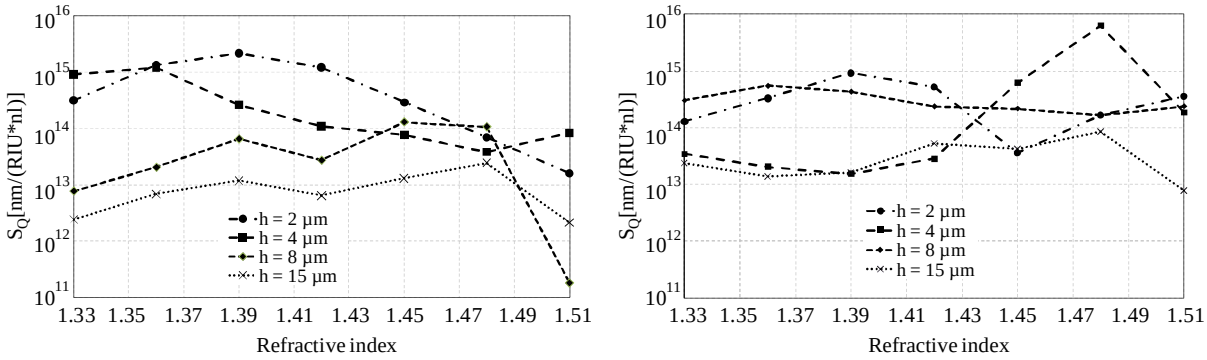

Figure 3.26: Amplified sensitivity S_Q *vs* refractive index of the mesurand fluid nfluid for 75 µm (a) and 150 µm (b) radius.

From Figure 3.26, we see that small volumes of low refractive index fluids should be measured by using smaller microspheres, as they have larger S_Q. For instance, $S_Q \geq 10^{15}$ nm/(RIU*nl) are obtained with $n_{fluid} \leq 1.42$ with h = 2 µm or h = 4 µm. For $n_{fluid} \geq 1.48$ the amplified sensitivity drops below 10^{15} nm/(RIU*nl), whatever the configuration defined by the PDMS height h. Conversely, larger refractive indices should be measured by using larger microspheres with R = 150 µm for which there exist some configurations with $S_Q \geq 1014$ or even $S_Q \geq 1015$ for $n_{fluid} = 1.48$. To get insight into the optimal configuration when a measurand fluid volume is the ruling parameter, we replot in Figure 3.27 the same data *vs* fluid volume. We see that smaller spheres provide larger S_Q for small values of nfluid, while larger sphere are generally preferable in all other cases.

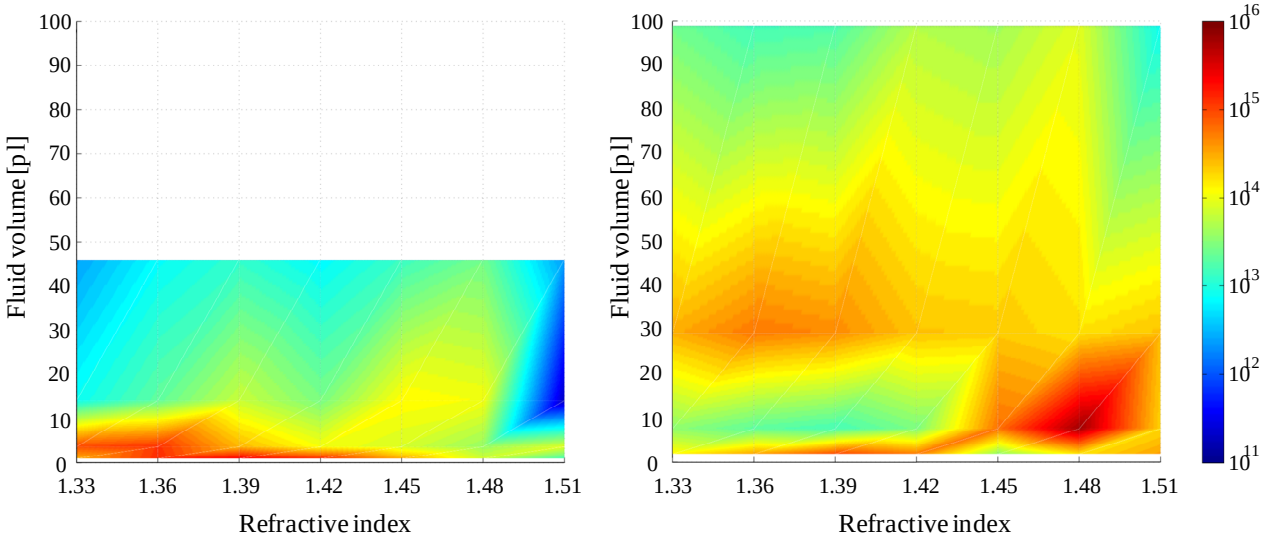

Figure 3.27: Amplified sensitivity S_Q vs measurand fluid volume nfluid for (a) R=75 µm and (b) R=150 µm.

We try to compare our results with the most sensitive resonant refractometric sensors reported in the literature. A sensitivity defined as $S = \frac{\partial \lambda}{\partial n}$ was found as high 30 nm/RIU for 55 µm radius microsphere fully immersed in water/ethanol solution [132] 160±25 nm/RIU for grated silicon wire [133], and 700 nm/RIU for an optical microfiber coil [134]. These values are higher than our 2nm/RIU (for h=2 µm and 0.925 pl), however, they refer to resonators fully submerged in the measurand fluid and they lack micro/nano-fluidic. Hence, their minimum possible fluid volumes are comparable or often much larger than the volume of the resonator (in the several nl to µl range), which significantly reduces the overall sensitivity per unit volume S_V.

3.8. Conclusions

Chapter 3 shows the great potentiality of WGM in a microsphere in filtering and sensing. Section 3.6 reports of an innovative tunable electro-optic filter. It combines the high *Q*-factor WGMs of the spherical resonators and the large electro-optic effect of the LCs into a simple and rugged filter. An applied voltage can tune the spectral response of the filter. The value of the FSR and the quality factor remains unchanged for the various values of the applied voltage. An increase of the applied voltage increases the power coupled with the sphere and increases the on–off ratio of the filter's insertion loss. Another important aspect of WGM is investigated in Section 3.7 where an optofluidic sensor is reported. The proposed device shows properties comparable with the state of the art. The optofluidic sensor is able to work with a fluid volume in the order of 1pl.

4. Optical filters based on Bragg's law including organic materials

4.1. Introduction

Optical tunable filters are essential components in WDM optical communication systems. An extensive research activity is today focused on the realization of novel tunable filters characterized by compactness, low cost, high performance and low power consumption. Integrated optics devices controlled by light can make fiber optic systems for telecom and sensor applications [135] completely electromagnetic interferences free and able to exploit the fiber optic near infrared bandwidth by using WDM [136].

Bragg filters have been demonstrated by employing waveguides made of different materials and structures such as polymers [137], silicon-on-insulator (SOI) [138], hollow capillaries [139] and liquid crystals (LC) [140]. One of the most important parameters for a Bragg filter is the tuning. In photonic applications, the most common mechanisms to tune such filters are thermo-optical effect [137], electro-optical effect [140] and opto-optical effect [141]. In the recent years, much attention has been devoted to liquid crystals (LC) and composite materials made of LC and polymers as efficient materials for photonic devices with filtering function.

In this chapter we study novel integrated tunable filters using LC gratings which introduce advantages in terms of compactness, low power consumption and low cost. In section 4.2 we report a detailed study of an electro-optical Bragg filter based on NLC, while in section 4.3 we report the fabrication and characterization of an opto-optical Bragg filter that involves azo-compounds. For the proposed devices, we study the performance of the devices in terms of tuning range.

4.2. Electro-optical filter based on liquid crystals

This section reports a detailed numerical study of a versatile configuration for a guided-wave voltage-tunable distributed feedback grating based on reorientation in NLC coplanar comb electrodes. The aim of the study is to obtain a wide tuning range with a low applied voltage, then with low power consumption. The proposed device allows a transverse electric (TE) mode to undergo distributed feedback with an adjustable Bragg wavelength in the whole C and L band for optical communications. The structure also ensures a bi-dimensional signal confinement in the planar NLC waveguide.

4.2.1. Device design

The device structure is a planar waveguide as sketched in Figure 4.1. It consists of a NLC layer sandwiched between two borosilicate BK7 glass plates. The LC considered in the structure is the E7, with properties reported in chapter 2. The inner face of one of the plates is patterned with comb-shaped Indium Tin Oxide (ITO) transparent electrodes as shown in Figure 4.2. The ITO electrodes are 100 nm thick, with complex refractive index $1.3 + i0.1$ at $\lambda = 1550$ nm. A 50 nm thick of *Nylon 6* is spinned in the inner interfaces of both glasses. The *Nylon 6* is necessary to obtain the right initial alignment for the LC. As initial alignment we assume a *pre-Twist* angle φ_0 of about 4° with respect to *z* in order to eliminate the Fréedericks threshold. Due to its low thickness and its

refractive index of 1.52 at λ = 1550 nm, the *Nylon 6* does not affect the propagation of light in the higher index NLC waveguide.

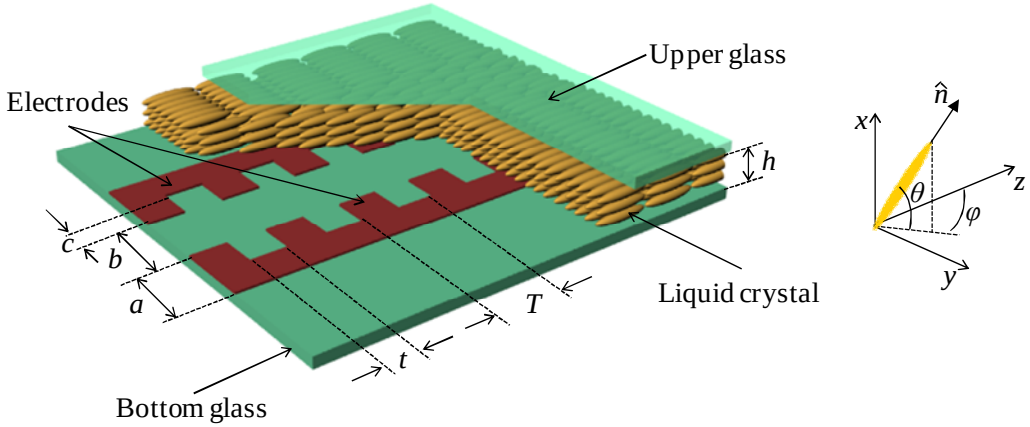

Figure 4.1: 3D sketch of the Bragg reflector and representation of the molecular director in the 3D space.

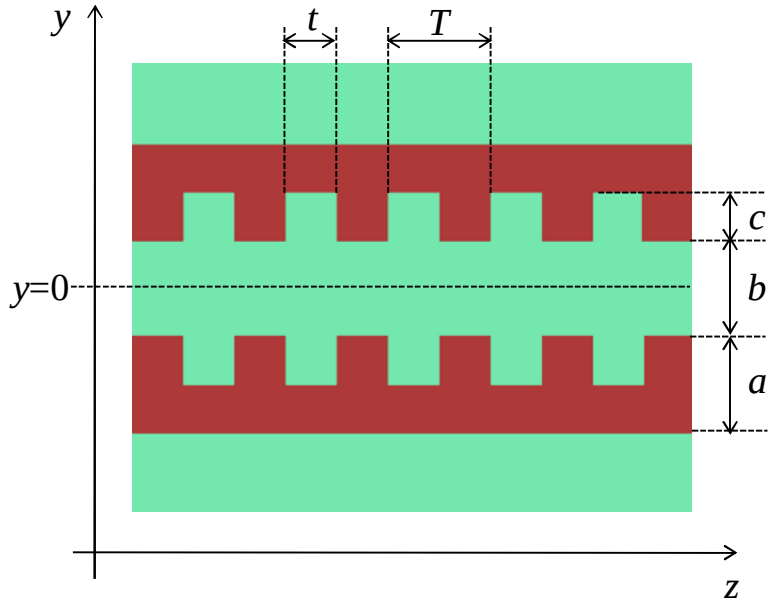

Figure 4.2: Electrodes top view.

As reported in Figure 4.2, both electrodes are periodic along *z* and symmetric with respect to *y* = 0. The electrode topology and the NLC parameters need to be selected in order to achieve high coupling between an injected transverse electric (TE) optical beam and the voltage-induced Bragg grating over a finite propagation distance. Moreover, the applied voltage is intended to increase the index in an NLC finite region along *y* and so ensure two-dimensional (2D) transverse confinement of the light injected in the thin film slab. In the regime of strong anchoring, the rubbed layers determine the boundary conditions for the molecular director in the glasses internal surfaces. Due to the position of the electrodes the electric field lines distribution assumes the behavior reported in Figure 4.3.

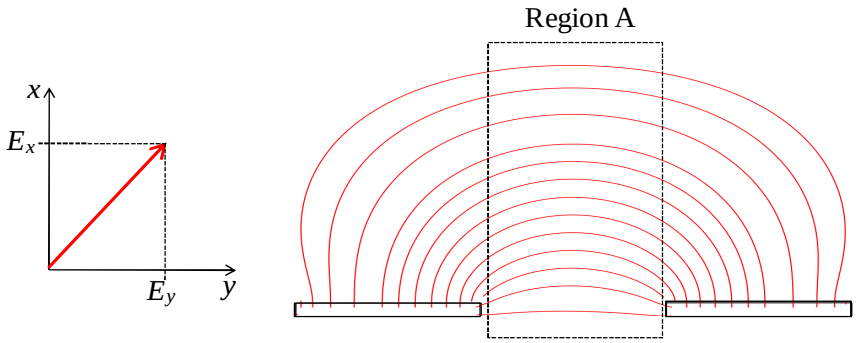

Figure 4.3: Electric field lines distribution.

In the region A, the region comprised between the two electrodes, for the electric field distribution we can consider that $E_y \rangle\rangle E_x$. It means that the LC reorientation in that area affects only the φ angle.

In order to obtain single mode operation at λ = 1550 nm, after several designs, we choose a device with geometries: NLC thickness h = 1 μm and electrode dimensions a = b = 500 nm, c = 250 nm, t = 250 nm and T = 500 nm.

An NLC layer with molecular director in the plane yz can support the propagation of transverse electric (TE) waves in the guide. The external voltage forces the rotation of the director in the bulk, yielding the formation of a periodic grating defined by the electrode topology.

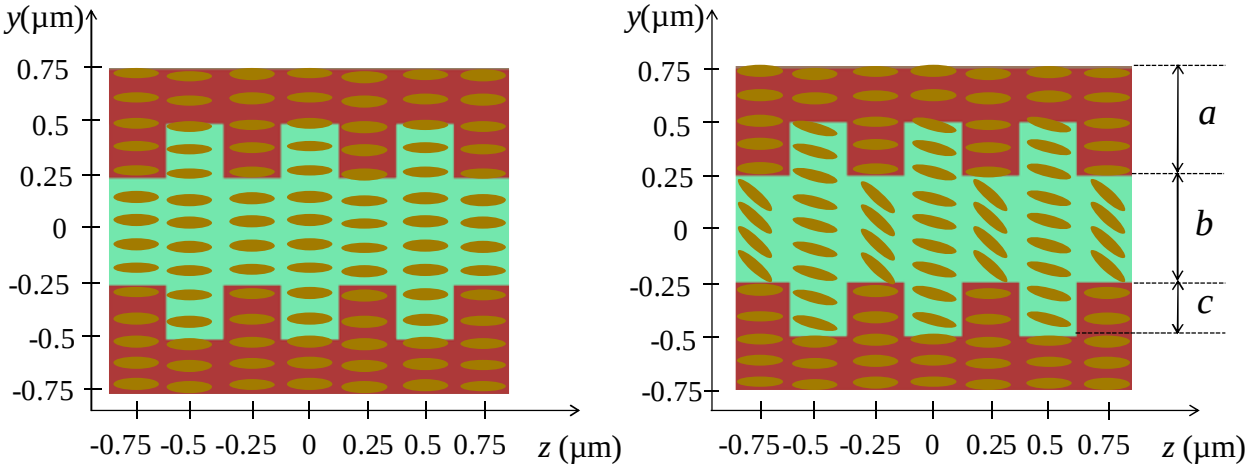

Figure 4.4: Sketch of liquid crystal reorientation above electrode area for V = 0 (left) and V > 0 (right).

Figure 4.4 displays molecular reorientation without and with applied voltage. At V = 0 V the director is aligned along z because the orientation imposed by the *Nylon 6*. An applied voltage can induce LC reorientation. The resulting *Twist* is larger in the regions where the inter-electrode separation is b (i. e. minimum inter-electrodes distance) as compared to those where the separation is b +2c (i. e. maximum inter-electrodes distance).

The low-frequency voltage applied between the electrodes perturbs the NLC molecular orientation, achieving an average increase of refractive index in a channel finite. The electro-optic orientation of the NLC director corresponds to the minimum of the free energy as reported in Equation 2.5. Minimization of Equation (2.6) and its solution yields the spatial distribution of the NLC director in

the reference system of Figure 4.1. To obtain a Bragg filter, we have to investigate two main properties of the device:

- the confinement of light in a limited 2D region of the structure;
- the grating definition along the direction of propagation.

Starting with the voltage-dependent molecular reorientation, we obtain the director distribution and finally the profile of the refractive index n_{TE} for extraordinarily TE-polarized light, i.e. for electric field vectors in the plane *xy*. Figure 4.5 shows the refractive index profile for TE-polarization for several values of the applied voltage.

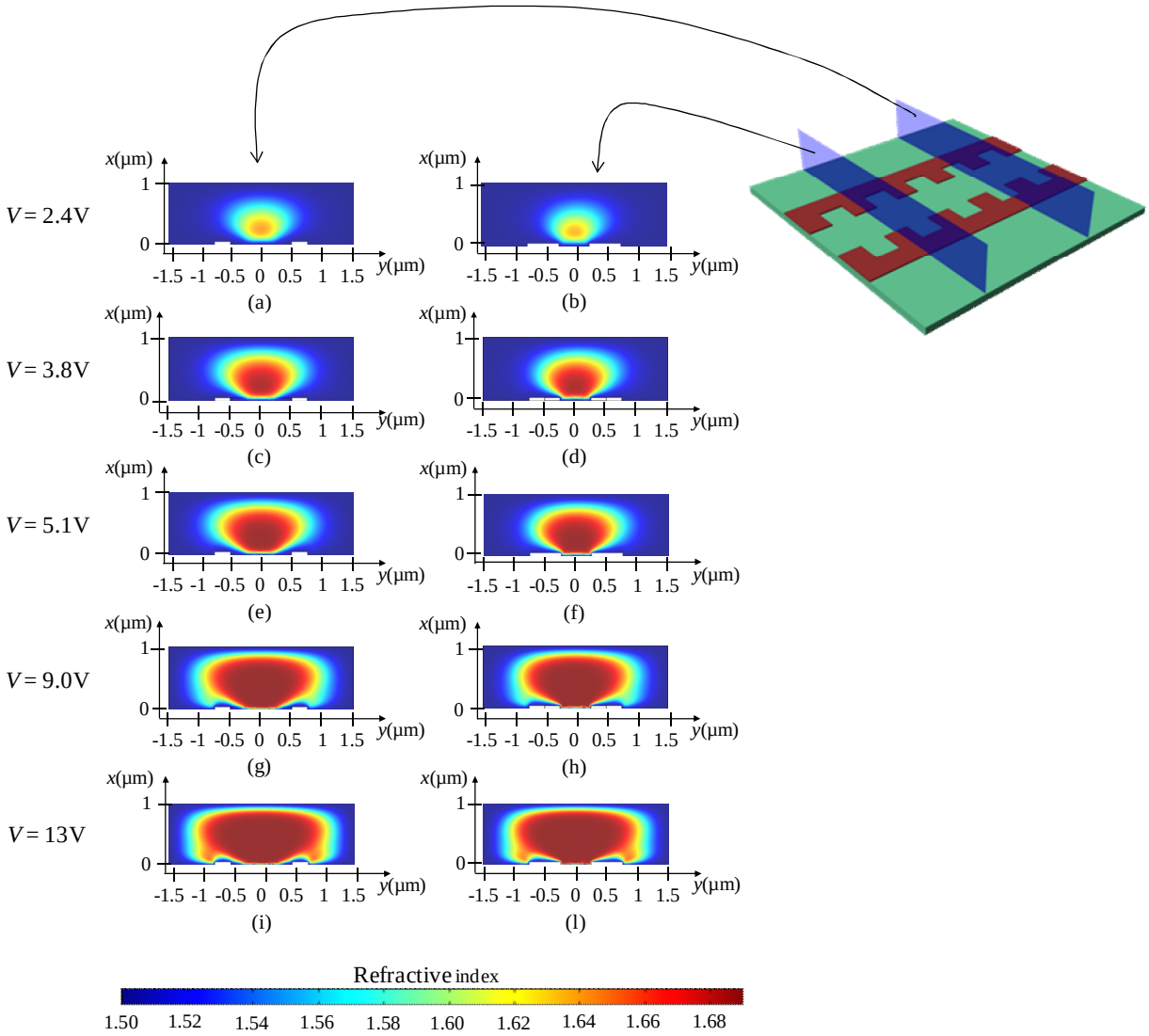

Figure 4.5: Refractive index profile for TE-polarization: (a) 2.4 V, z = 0 μm; (b) 2.4 V, z = 0.25 μm; (c) 3.8 V, z = 0 μm; (d) 3.8 V, z = 0.25 μm; (e) 5.1 V, z = 0 μm; (f) 5.1 V, z = 0.25 μm; (g) 9 V, z = 0 μm; (h) 9 V, z = 0.25 μm; (i) 13 V, z = 0 μm; (l) 13 V, z = 0.25 μm.

Because the non local electro-optic response of NLC, the distribution of the refractive index:

$$n_{TE}(z) = \frac{n_e n_o}{\sqrt{n_e^2 \cos^2 \varphi + n_o^2 \sin^2 \varphi}} \tag{4.1}$$

for the extraordinary TE-polarized electric field of TE modes in the planar waveguide (confinement across x) can be approximated by solving:

$$K\nabla^2\varphi - \frac{\Delta\varepsilon\left|E_y\right|^2}{2}\sin 2\varphi = 0 \tag{4.2}$$

Where $K \approx K_{22}$ and $E_y = E_y(x, y, z)$ is the dominant component of the applied (low-frequency) electric field. We consider $K \approx K_{22}$ because the main term in the definition of the elastic energy of the LC is the *Twist* deformation. Boundary conditions are dictated by the surface anchoring in $x = 0$ and $x = h$.

A mode solver or, equivalently, a beam propagator can then yield the transverse profile of the guided field distribution at a given wavelength and for each applied voltage. Due to the particular choice of parameters, only the fundamental order TE_{00} mode propagated in the structure. Figure 4.6 shows the TE_{00} mode transverse profile for a bias V = 5V, with an effective mode index, n_{TE00} = 1.5474 at λ = 1550 nm. The waveguide is mono-modal in the voltage range 0 V - 11 V.

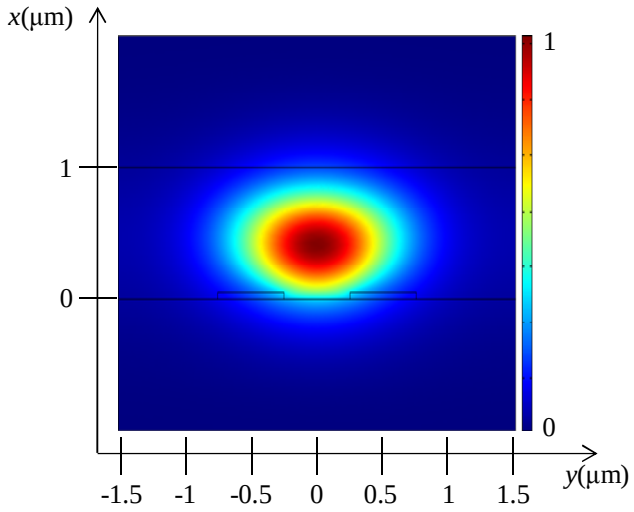

Figure 4.6: Intensity profile of the fundamental TE mode at 1550 nm for V = 5 V.

After the demonstration of 2D confinement of light, we can investigate the formation of the grating along the direction of propagation. The periodic separation between the electrodes yields a modulated strength of E_y and, correspondingly, a modulation of n_{TE} along z. Figure 4.7 displays the index modulation in a 6-period region along z, evaluated in x = 0.2 μm and y = 0 for various biases between 2.8 and 4.5 V.

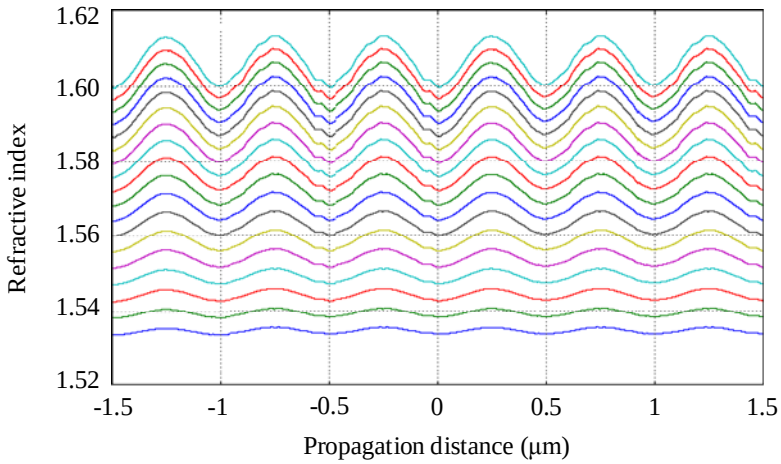

Figure 4.7: Refractive index modulation along z for applied voltages between 2.8V (bottom line) and 4.5V (top line) in 0.1V steps, evaluated 200nm above the electrodes and in the symmetry axis between them (y = 0).

As expected, the modulation is sinusoidal with a 0.5 μm period, maximum when the electrode spacing is *b*. The refractive index distribution for a TE input light, $n_{TE}(z)$, in the central region of the grating can be expressed as:

$$n_{TE}(z) = A + \frac{\Delta n}{2}\cos\left(\frac{2\pi}{T}z\right) \tag{4.3}$$

A is the average refractive index for the NLC along the direction of propagation, Δn is the difference between the maximum and the minimum of each sine curve. *T* is the period of the grating. Both *A* and Δn depend on the applied voltage, while *T* depends only on the electrodes geometry.

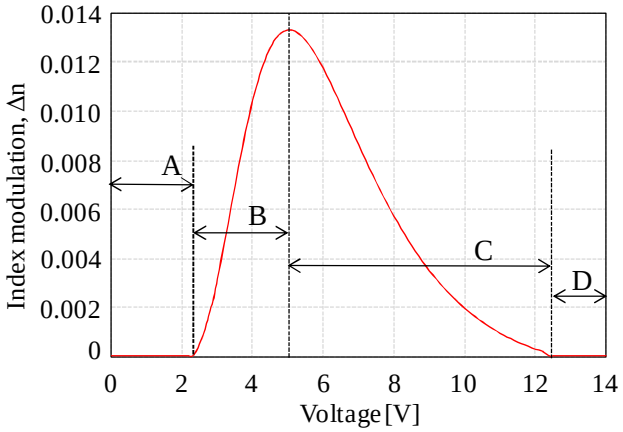

Figure 4.8: Longitudinal modulation versus applied voltage.

Figure 4.8 graphs the resulting index contrast versus voltage between 0 and 13 V. For $V = 5$ V the NLC director is entirely reoriented (//*y*) in the regions with minimum inter-electrode separation (*b*), but only partially reoriented where the electrodes are separated by $b + 2c$. Therefore, by increasing the voltage above 5V only the un-saturated NLC regions can still reorient, resulting in a progressive reduction of the index modulation for $V > 5$V. For $V = 12.4$ V the whole NLC has reoriented with director //*y* and a negligible index contrast. From Figure 4.8, four regions are well defined:

A) $V < 2.4$ V: the applied voltage is too low to create a grating;
B) 2.4 V $< V <$ 5 V: the NLC comprised in the region with minimum inter-electrodes distance, starts to reorient and for $V = 5$ V it reaches the saturation;
C) 5 V $< V <$ 12.3 V: only the un-saturated NLC region can still reorient;
D) $V >$ 12.3 V: all the NLC is reoriented and there is no grating in the structure. In this case the structure can be considered as a waveguide.
In all regions when the applied voltage increases, the parameter A in Equation (4.3) increases. In the region B the parameter Δn increases when the voltage increases. In the region C, the parameter Δn decreases when the applied voltage increases. In the regions A and D, $\Delta n = 0$ because in the region A the applied voltage is too low for the formation of a grating, while in the region D the entire LC is reoriented then no index modulation occurs.

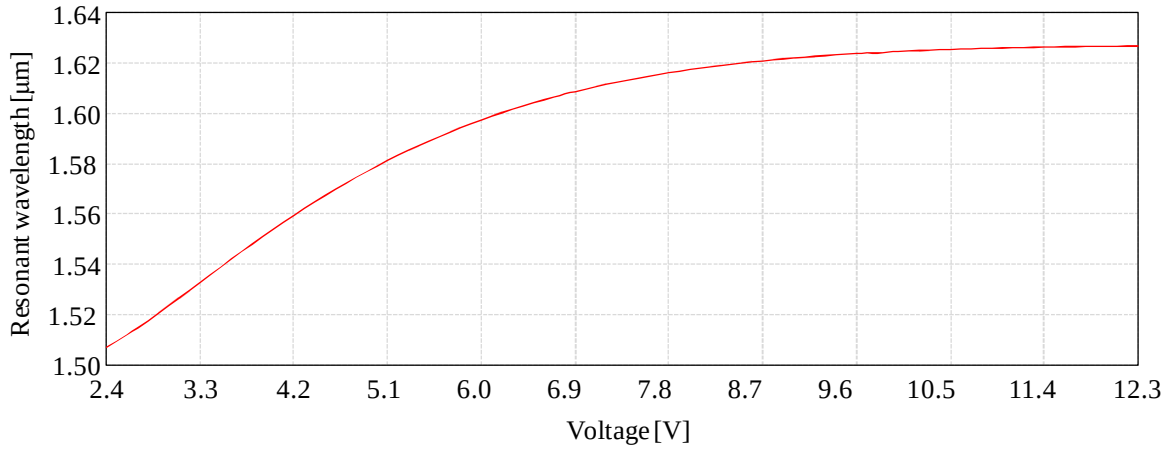

Figure 4.9: Bragg resonant wavelength versus applied voltage.

Based on the *e*-index distribution and using coupled mode theory, we calculated the resonant Bragg wavelength (Figure 4.9) as well as the back-reflected power for TE light propagating over 3000 periods, i.e. a grating length of 1.5 mm (Figure 4.10).

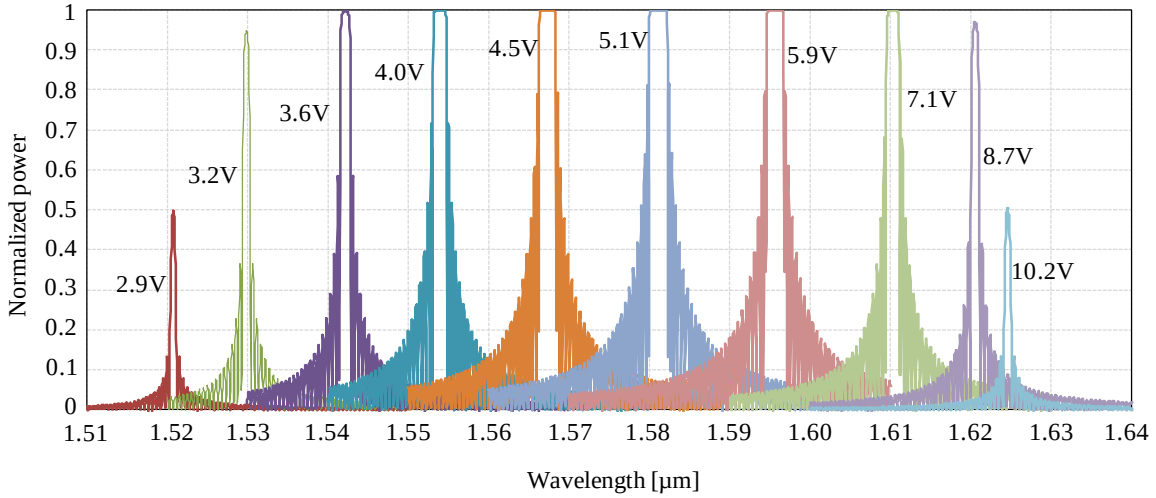

Figure 4.10: Spectral reflectivity for various voltages and propagation over 1.5mm (3000 periods). From left to right the backreflected wavelength positions are 1.52076µm, 1.5299µm), 1.54219µm, 1.55394µm, 1.56731µm, 1.58108µm, 1.59565µm, 1.61032µm, 1.62052µm and 1.6246µm.

The reflected wavelength at resonance red-shifts with applied biases of a few volts, providing an extended tunability of 104 nm with a reflectivity R = 50% (98 nm for R = 90%) while maintaining

good spectral selectivity. For a fixed voltage, the length of the grating does not affect the backreflected wavelength. The length of the grating plays a crucial role in the definition of the FWHM and the backreflected power. Figure 4.11 reports the behaviour of the FWHM and also the backreflected power as a function of the applied voltage.

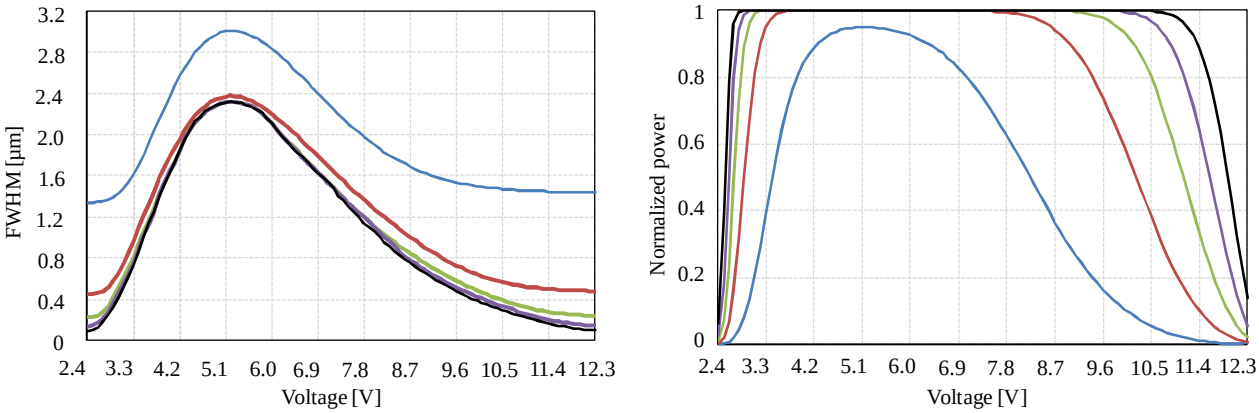

Figure 4.11: FWHM (left) and Bragg reflectivity (right) versus voltage for a few propagation lengths L in mm: 0.5 (blue), 1.5 (red), 3 (green), 5 (violet), 8 (black).

Graphs of FWHM and Bragg reflectivity versus bias are reported in Figure 4.11, for various reflector lengths, from 0.5 to 8.0 mm. Furthermore, for a given propagation length, a modest change in bias can alter the reflectivity. For instance, for L = 1.0 mm (2.0 mm) R increases from 30 to 100% (70 to 100%) as the voltage changes from 2.8 to 4.5 V.
The FWHM assumes the same shape of the refractive index modulation reported in Figure 4.8. The FWHM increases when the index modulation increases. For a grating length over 1.5 mm the FWHM starts to be independent from the length. The backreflected power is strictly related to the length because the increase of the length implies the enhanced of the constructive interference contributions that make the total backreflected power.

4.3. All-optical filter based on composite material

Recently, composite organic materials, such as azo-dye doped liquid cystals, have been engineered to obtain all-optical effects which proved very efficient in terms of switching speed and low driving optical power [142] [143]. Furthermore, micro/nano structured templates designed to realize holographic gratings called POLICRYPS (POlimer LIquid CRYstal Polymer Slices) [144] [145], based on polymers and LC, have been combined with such azo compounds to obtain efficient, optically controllable, free-space devices [146].
In this section we introduce and experimentally demonstrate an integrated all-optical tunable filter. We demonstrated a polarization independent all-optical Bragg filter integrated on glass made of ion exchanged channel waveguides and composite holographic gratings. The reversible trans-cis photoisomerization of azobenzene and its derivatives make LC a suitable medium for recording a diffraction grating for light. The filter exhibits a signal suppression more than 20 dB at the Bragg wavelength. A tuning range of 6.6 nm is observed by applying a pump of 45 mW. Simulations yield a Bragg wavelength shift in full agreement with our measurements.

4.3.1. Device fabrication

The filter is obtained by combining a simple low cost ion-exchange waveguide technology with a composite LC and a well-known photosensitive azo-dye compound, methyl red (MR), to enable full optical tuning at the telecom wavelengths.

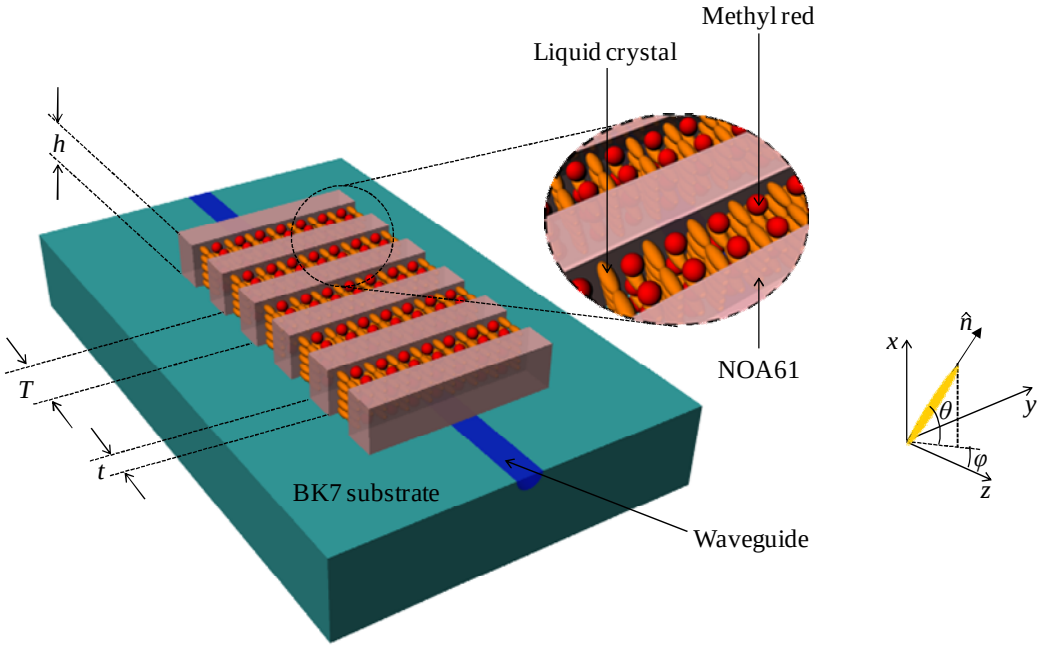

Figure 4.12: Schematic view of the proposed device with a zoom on the grating structure. The right inset sketches the orientation Tilt (θ) and Twist (φ) angles of the molecular director $\hat{n}$.

The fabrication of the device exploits a reliable low cost technique. First of all a double ion-exchange process (KNO_3-$AgNO_3$) is carried out to obtain a channel optical waveguide on a BK7 glass substrate as reported in chapter 3. A BK7 cover is placed on the top of the processed substrate by using ball spacers of about 1 μm, mixed to an UV-curable glue NOA61 to control the gap.

The basic idea for the fabrication of the grating is to avoid the formation of a separated NLC phase during the curing process. In this way we avoid the growing of NLC droplets obtaining only a macroscopic phase separation. This result is obtained by exploiting the high diffusion, which the NLC molecules can undergo when they are in the isotropic state. The realization of gratings is therefore the result of a new technique, that we have introduced, and called MPTIPS [147], from the acronym Mixed Polymerisation Thermal Induced Phase Separation. The standard procedure consists of the following steps:

a) The heating of a sample of photoinitiator monomer - NLC:MR mixture up to a temperature which is above the Nematic-Isotropic transition point of the NLC:MR component. This step prevents the appearance of a nematic phase during the curing process;

b) The illumination of the sample with the interference pattern of a curing UV radiation;

c) The slow cooling of the sample below the Isotropic-Nematic transition point (typically, down to the room temperature) after the curing radiation has been switched off and the polymerization process has come to the end.

The chemical mixture used to fill the cells has been prepared by diluting a small amount of E7 and Methyl Red (≈30 wt %) in the pre-polymer system Norland Optical Adhesive NOA61. The grating

has been cured by a total UV intensity of 11 mW/cm^2, acting on the sample for ≈ 1000 sec. Following the technique described in details in [148], we infiltrated the polymeric structure with NLC E7 doped with MR, 2% in weight, because it is the highest possible solubility of MR in NLC to minimize the pump power required for the optical switching [149]. E7 and MR have been chosen for their easy availability and well known properties, which allow immediate comparison with previous works.

The grating period is estimated in the Λ=1.50-1.55 μm range. At the thermal equilibrium, with no applied external stimulus, the MR is in its elongated *trans* form. The MR:E7 behaves as a guest-host optically anisotropic mixture of an LC compound and a non liquid crystalline compound. Figure 4.13 reports the micrograph of the fabricated device.

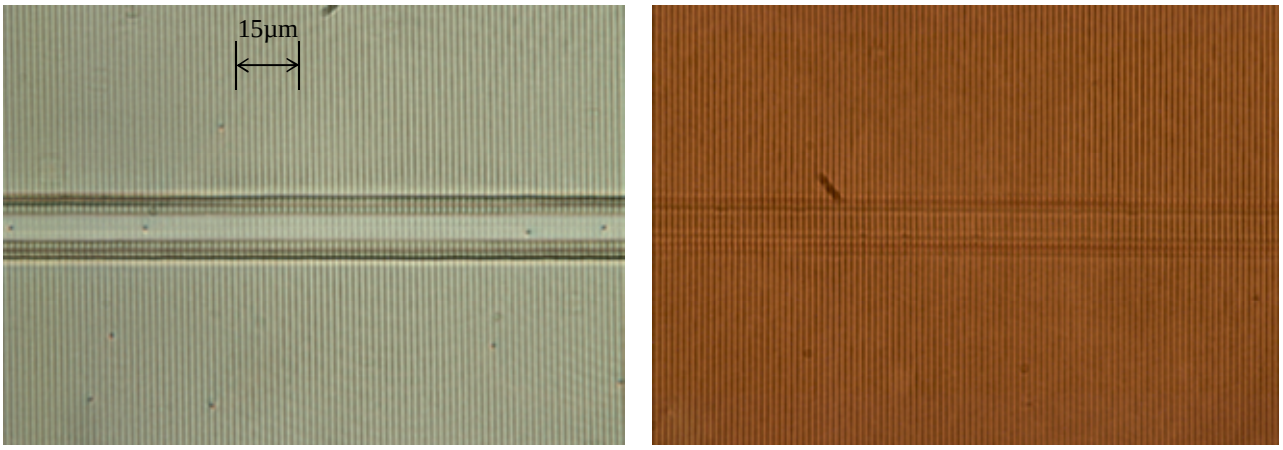

Figure 4.13: Micrograph of the grating without (left) and with (right) the NLC:MR mixture. In the centre of each micrograph is well recognizable the waveguide.

When compared to conventional holographic writing of periodic polymeric templates, our technique provides two striking advantages:

- it is completely insensitive to dust particles because the polymerization occurs in a sealed device;
- the polymer symmetrically adheres to both glass substrates leaving no gaps at all.

4.3.2. Devices characterization

In the LC:MR mixture, the long axis of the LC molecules and long axis of trans-MR remain aligned perpendicularly to the polymer slices, as in all POLICRYPS [150], as easily verified by the polarized adsorption spectrum. Due to the mismatch between the *trans* MR:E7 ordinary refractive index and the NOA61 index (1.5419 at 1550 nm) [151] the overlaying grating, a TE-like optical beam in the waveguide experiences a phase grating. This enables the device to operate as a Bragg filter. According to the Bragg law, the back-reflected wavelength λB is given by:

$$\lambda_B = \left(2\Lambda n_{eff}\right)/m \tag{4.4}$$

where *m* is the diffraction order and *neff* is the effective refractive index of the guided mode. The latter depends on the ion diffusion profile in the glass, on the overlayer refractive index and thickness, and on the upper glass refractive index. For *m* = 3, λB is in the telecom wavelength range of 1520-1570 nm.

The MR turns in the spherical *cis* form when the grating is irradiated by a green light beam λ=532 nm because of the absorption band of trans isomer. Such conformational transition breaks the directional order of the MR-E7 guest-host. In this condition, the NLC: MR mixture behaves like an optically isotropic material, as clearly verified by optical observation using a polarized microscope. The refractive index of the mixture after exposure can be estimated as the average value given by [152]

$$\langle n \rangle = \sqrt{\frac{n_{\parallel}^2 + 2n_{\perp}^2}{3}} = 1.5655 \tag{4.5}$$

There is therefore, a mismatch with the polymer refractive index and a variation in the value of λ_B.

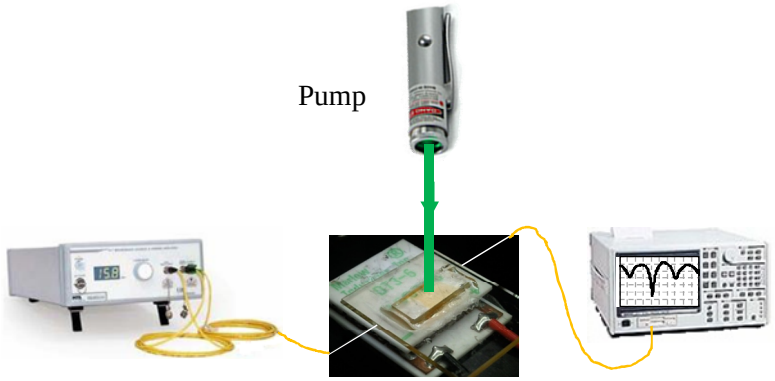

Figure 4.14: Setup to measure the transmitted spectra.

Figure 4.14 shows the setup used for measuring the transmitted spectra of this tunable filter. The polished input and output facets of the device were butt-coupled to single mode fibres. The input signal was supplied by an erbium doped fiber amplifier (EBS 4016/EDFA), used as a broadband source, emitting a signal from 1520 nm to 1580 nm. The filtered light signal was sent to an optical spectrum analyser. In all experiments, the sample temperature was set at 20.8°C. The pump laser with a circular spot (about 2 mm in diameter) at λ=532 nm emits 45 mW, which exceeds the *trans-cis* transition threshold, though it does not affect the temperature of the mixture. Figure 4.15 shows the transmitted spectrum, with a notch peak of -20 dB at λ=1545.7 nm when the pump is OFF (black line).

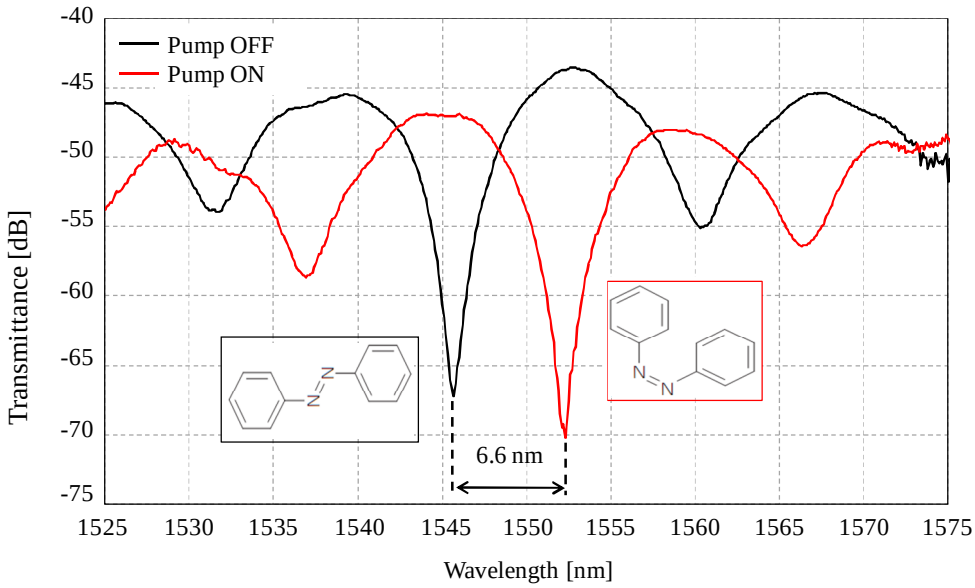

Figure 4.15: Transmittance of the all-optical filter. Black line – Pump OFF; inset with azo dye in trans-phase. Red line – Pump ON; inset with azo dye in cis-form.

When the pump is ON, the spectrum is shifted by 6.6 nm (red line), preserving its shape but with a slightly deeper notch of about -22 dB. The bandwidth of the transmitted notch, at -3 dB with respect to the transmittance minimum, is 3.3 nm when the pump is OFF and 2.7 nm when the pump is ON. The difference between these two values is because the different path of the light inside the structure in the ON and OFF state.

4.3.3.Numerical analysis

We have used Equation (4.4), to simulate the behavior of the filter in two computational steps.

- First, we studied the orientation of the NLC director between the NOA61 stripes in the POLICRYPS. The director profile was computed by minimizing the LC free energy, by solving the partial derivate Euler-Lagrange equation in the weak form by finite element method. In this case the equation reported in [Riferimento cap2] is inadequate to study the problem because it does not take into account the mechanical reorientation induced by the deformation of the exposed MR.
- Second, the NLC refractive index distribution derived from the director profile was used to describe the grating by a grating mode solver [[153]]. The computed effective index was then used in Equation (4.4).

In the simulation, we considered three different values of the grating thickness h = 1 µm, h = 1.1 µm and h = 1.2 µm, to consider the uncertainty in the estimation of the device gap. An increase of h yields an increase of n_{eff}. Initially, the NLC director is considered to be parallel to the z direction, therefore the input light with any polarization experiences the NLC $n_{\perp}$. After exposure to green light the NLC behaves isotropically and the average E7 refractive index $\langle n \rangle$=1.5655 is sensed by any input light polarization.

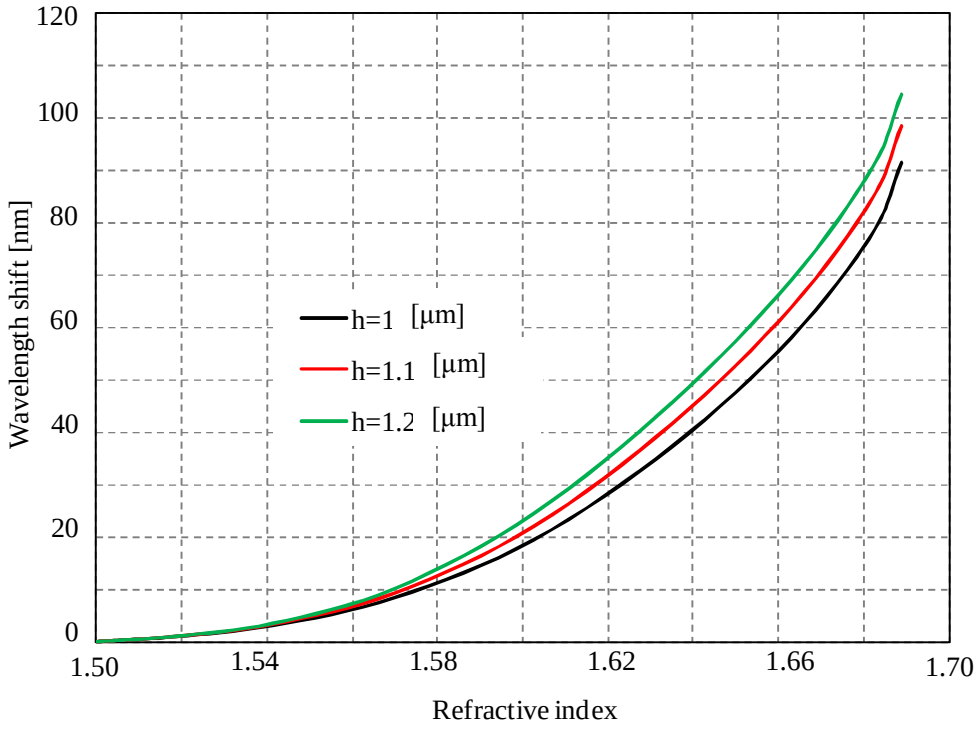

Figure 4.16: Wavelength shift vs NLC refractive index for three values of grating thickness.

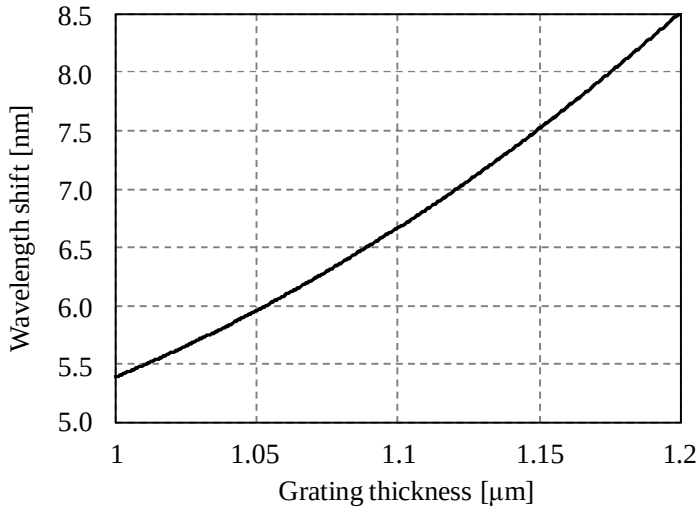

Figure 4.17: Wavelength shift vs grating thickness for NLC index of 1.5655.

As shown in Figure 4.17, where the wavelength shift ($\Delta\lambda_B$) is computed with respect to λ_B for n_{LC}=1.5, we obtained $\Delta\lambda_{B1}$=5.88 nm for h= 1 µm, $\Delta\lambda_{B2}$=7.25 nm for h=1.1 µm and $\Delta\lambda_{B3}$=9.19 µm for h=1.2 µm. An increase of h yields an increase of $\Delta\lambda_B$, for the same value of the NLC refractive index. This is due to a smaller influence of the boundary conditions as h increases. Figure 4.17 shows that $\Delta\lambda_B$ is about 6.6 nm, for h=1.1 µm, which is consistent with the measured shift and gap of our sample. To complete the analysis of the proposed device we also report the experimental results when the temperature of the sample changes.

The sample under investigation is positioned over a heater. The temperature of the sample is controlled by the application of a proper current in the heather. The experimental result of the thermal effect is represented in Figure 4.18.

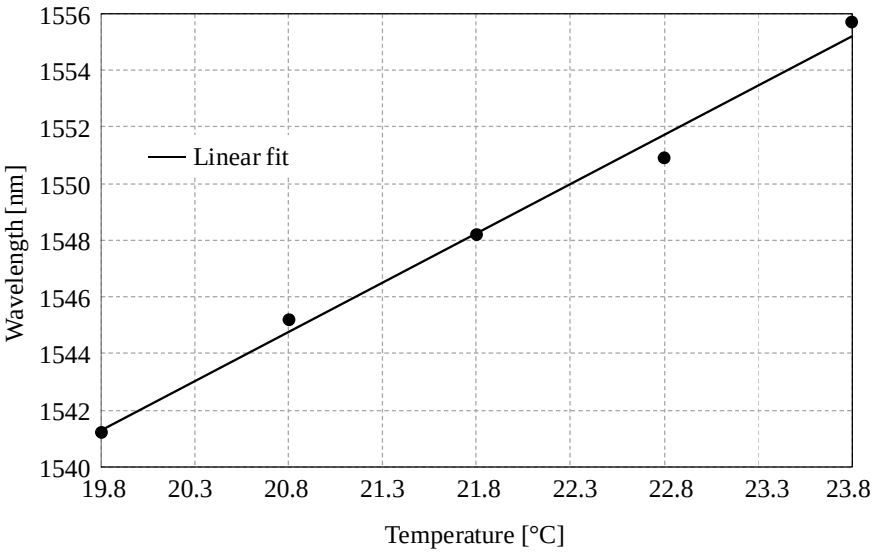

Figure 4.18: Wavelength shift as a function of the temperature with the laser pump OFF.

Figure 4.18 shows that the wavelength shift with the temperature is well described by a linear curve. The resonant wavelength shifts from 1541 nm to 1555 nm, when the sample temperature changes from 19.8°C to 23.8°C.

The temperature variation of all materials involved in the structures implies a change in their refractive index. The bottom glass and the upper glass do not have an important role in the definition of the wavelength shift with the temperature because their low thermo-optical coefficient (about -10^{-6}/°C) [154]. The MR does not influence n_{eff}, due to its relative low percentage in the NLC:MR mixture. The increase of temperature modifies the refractive index difference between the NOA61 and the MR:E7 mixture because they have different thermo-optical coefficients. The thermo-optical coefficient for the NOA61 is about -10^{-3}/°C [151]. In the NLC both $n_{\perp}$ and $n_{||}$ depend on the temperature. When the temperature increases $n_{||}$ decreases while $n_{\perp}$ increases. In this mixture, the long axis of the LC remains parallel to *z*-axes therefore, only $n_{\perp}$ must be considered. The thermo-optical coefficient for $n_{\perp}$ is greater than the NOA61 thermo-optics coefficient and it is also positive [155]. The total effect induced by the temperature increase is the increase of n_{eff} then a red-shift of the resonant wavelength.

4.4. Conclusion

The devices proposed show two possible strategies to implement tunable Bragg reflectors based on liquid crystals. The working principle of the proposed configuration are based on the electro-optical and on the opto-optical effects to obtain the reorientation of the liquid crystal and the desiderate variation of the spectral response of the devices.

The Bragg filter proposed in section 4.2, demonstrates how it is possible to induce a refractive index modulation, with a proper geometrical definition of ITO electrodes, along the propagation direction, which allows a wavelength selective propagation of confined light inside the liquid crystal layer. A conspicuous wavelength tuning combined with an high wavelength selectivity can be obtained in both reflectors by applying low driving voltages. In fact the device provides transverse light confinement and periodic index modulation, yielding high reflectivity in a wide tuning range of

104nm for voltages between 2.5 and 10.2V. This novel geometry provides ease of fabrication and a simple electro-optic control, while ensuring Bragg reflection and spectral filtering over a wide range of wavelengths in the whole C + L band for optical communications.

In section 4.3 it is reported how the isomerization of azo-compunds can be used to obtain the all-optical control of photonic devices. The advantage of all-optical devices is the absence of control electrodes that usually determinates losses in the structures. As effect of an applied green laser pump, the azo-compound modifies mechanically its structures. This effect is used to reorient mechanically the NLC.

We demonstrated a polarization independent all-optical Bragg filter integrated on glass made of ion exchanged channel waveguides and composite holographic gratings. The filter exhibits a signal suppression more than 20 dB at the Bragg wavelength. A tuning range of 6.6 nm is observed by applying an optical pump with a density power of about 1.43 W/cm^2.

5. Optofluidic sensors based on plasmonic structures

5.1. Introduction

As first demonstrated by Ebbesen and co-workers [156], making a periodic arrangement of subwavelength holes in an otherwise optically opaque metal film may induce an extraordinary amount of light transmittance for certain frequencies, the so-called extraordinary optical transmission. The enhanced transmittance is attributed to the excitation of surface plasmon polaritons (SPPs) [157], i.e. surface waves that arise from the interaction between light beams and the collective plasma oscillations of the conduction electrons in the metal. One may intuitively expect that an ultrathin and semi-transparent film would turn even more transparent if it were to be perforated by sub-wavelength apertures. Conversely, analytically and numerically calculations predicted that the transmission of light can be totally suppressed [158], provided that the sub-wavelength holes arranged in a regular and periodic fashion. This was attributed to the sign change at the metal/dielectric interface of the real part of the dielectric permittivity of the metal evanescent SPPs fields, which are highly confined at the boundary of the metal. The manipulation of confined electromagnetic field and tailoring the SPPs resonances in different plasmonic media are crucial for developing negative index materials [159], nanoscale optical switches [160], and label-free chemical and biological sensors [161] [162]. To improve the performance of plasmonic devices, significant effort has been devoted toward optimizing the quality of SPPs as well their tunability. In this paper we present a device based on two-dimensional (2D) arrays of non-touching gold rings and we analyze how to optimize the electromagnetic scattering properties. In order to obtain a better quality of the SPPs we study how the geometrical parameters of the rings affect the SPPs. We illustrate the dependence of substrate effects and tunability of the SPPs, by simulating the impact of covering the samples by a thin fluidic layer of varying height and fluid-refractive index.

5.2. Device geometry and fluid effects

Fig. 1 illustrates the structure under investigation. We focus on two-dimensional arrays of circular gold rings on a quartz substrate. The thickness, internal radius of the rings, external radius of the rings, and period of the structures are denoted by *h*, *a*, *b* and *T*, respectively. The anticipated structures can be fabricated by means of electron-beam lithography (EBL), as discussed in Ref. [163]. In the following, we study the case of a plane wave illuminating the structure at normal incidence. The axes in Figure 5.1(a) indicate the direction of propagation and polarization of the incident plane wave. The scattering spectrum can show pronounced absorption and specific wavelengths, depending on the effective index of the SPP.

The effective index implicitly reflects the optical material properties and geometrical parameters of the device. As a specific example, we consider gold nanostructures deposited on a quartz substrate, which is assumed to be semi-infinite in the *z* direction, for simplicity. In addition to the lattice constant, the internal and external radius of the rings and the gold thickness constitute the key geometrical parameters. For our later analysis we introduce the following function:

$$f_g = f(a,T)\big|_{b=\text{cost}} = \pi(b^2 - a^2)/T^2, \tag{5.1}$$

which quantifies the relative gold-surface coverage and is independent on the gold thickness *h*.

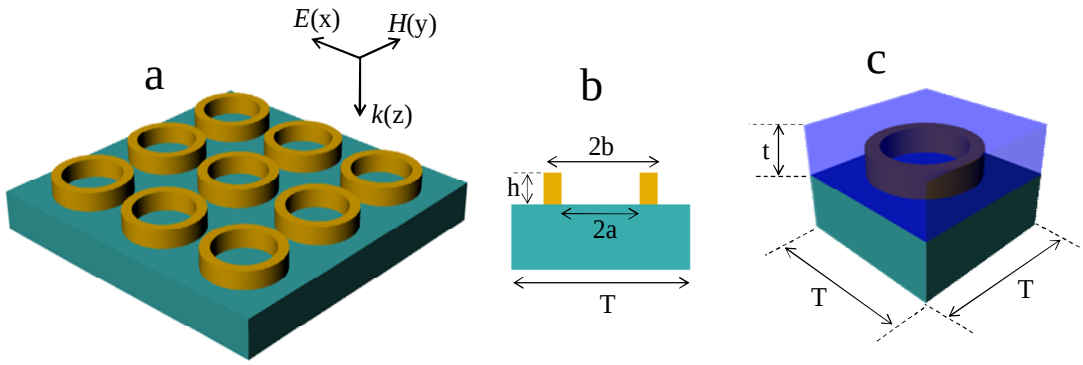

Figure 5.1: (a) Schematic illustration of a two-dimensional periodic array of metal rings on a quartz wafer, (b) cross section of a single unit cell where the thickness, internal radius of the rings, external radius of the rings and period of the structures are denoted by *h*, *a*, *b* and *T*, respectively, (c) a device (with a single unit cell) covered by a fluid layer of thickness *t*.

To further simplify our parameter study we limit our analysis to a fixed external radius b = 300 nm, which is comparable to the dimension of the disc structures fabricated in Ref. [164]. This allows us to verify our numerical model against measured results (analysis not included).
Clearly, for fixed T and b the surface coverage f is a dimensionless parameterization of the changes in the internal radius. In the following, we keep f fixed and vary the thickness of the gold. As shown in Figure 5.2 this thickness strongly affects the spectral response even for the disc limit ($a = 0$) in a unit cell with T = 700 nm, corresponding to a gold-surface coverage of 57%. According to Equation (5.1), the latter choice allows to explore a large range of values for fg while at the same time it suppresses transmission in the technologically interesting wavelength region of the C band of optical communication.

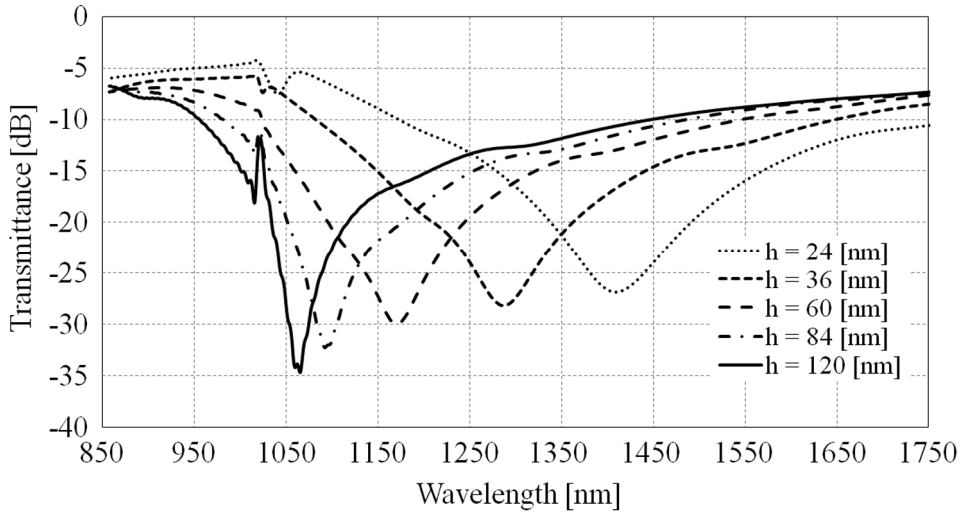

Figure 5.2: Simulated zero order transmittance spectra as a function of the gold thickness *h*, for a = 0 nm, b = 300nm and T = 700nm.

Figure 5.2 illustrates how the resonance is blueshifted when the thickness of the gold disk is increased. To get a deeper insight, we note that for a continuous film, the SPP modes guided by the two interfaces strongly couple in the thin-film limit, on the contrary they are almost decoupled for a thicker film, i.e., h = 120 nm. Under this circumstance, the SPP resonance is related only to the mode for a single interface. The suppressed transmission around 1022 nm is a manifestation of the

Rayleigh-Wood anomaly, or sometimes just referred to as the Rayleigh anomaly (RA). The characteristic wavelength of the first order obeys the relationship:

$$\lambda_{Rayleigh} = n_{substrate} \cdot T \tag{5.2}$$

From the dispersion of the SPP at an interface between a dielectric and a metal, the SPP resonance is very close to the RA. As anticipated for the RA, Figure 5.2 shows that the spectral feature at 1022 nm does not depend on the film thickness.

It is also seen that the transmittance is almost totally suppressed at a resonant wavelength above the RA, with a clear spectral dependence on the thickness of the film. In an effective-index picture, the variation of *h* induces changes in the SPP dispersion relation and its effective index.

We evaluate both the effects of the thickness and internal radius variations as shown in Figure 5.3(a). Each curve in Figure 5.3(a) is well fitted by a quadratic curve, indicating a linear dependence on the gold-surface coverage. In all computations, the depth of the suppressed wavelength is in -25 to -35 dB range, thus effectively giving a total suppression of the transmitted signal. In order to quantify the sensitivity to changes in geometry we introduce the dimensionless parameter *Sg* defined as:

$$S_g = \Delta\lambda / \Delta a \tag{5.3}$$

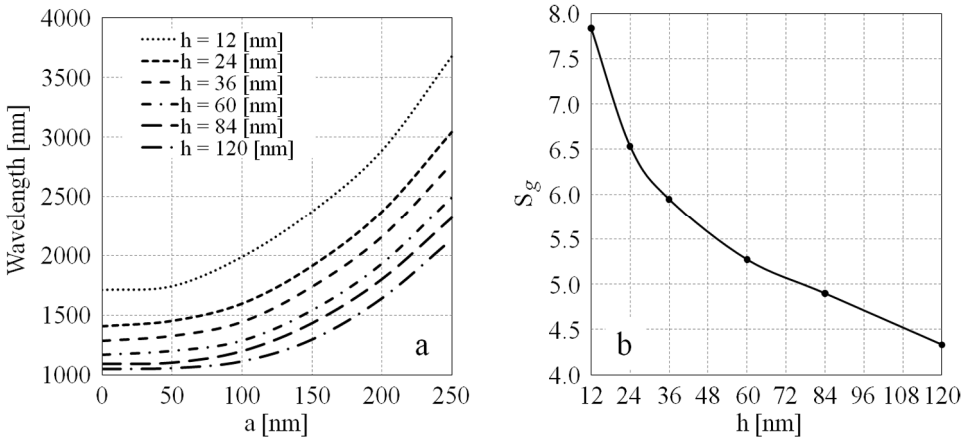

Figure 5.3: (a) Resonant wavelength position as a function of the gold thickness *h*, for *b* = 300 nm and *T* = 700 nm, (b) geometrical sensitivity S*g* as a function of *h*.

Figure 5.3(b) shows the geometrical sensitivity of the device. It suggests that the increase of *h* implies the reduction of the geometrical sensitivity. The analysis of the geometrical sensitivity is interesting because the thickness of gold below 200 nm is well controlled during the fabrication process and the control of the internal radius is limited by the resolution of the EBL.

We also evaluate the effects of an isotropic fluid positioned over the structure for its use as an optofluidic sensor. In particular we investigate the geometry *T* = 700 nm, as mentioned before, and *h* = 120 nm because it ensures a low geometrical sensitivity. The effects of the fluid are quantified in terms of the volume and of the refractive index of the fluid. For a sensor both sensitivity and Q-factor are important, see e.g. [165]. The latter correlates with the accuracy by which one can quantify minute shifts of the resonance wavelength. To evaluate the wavelength shift we study the configuration for which gold and the fluid thicknesses of have the same value *h* = *t* = 120nm.

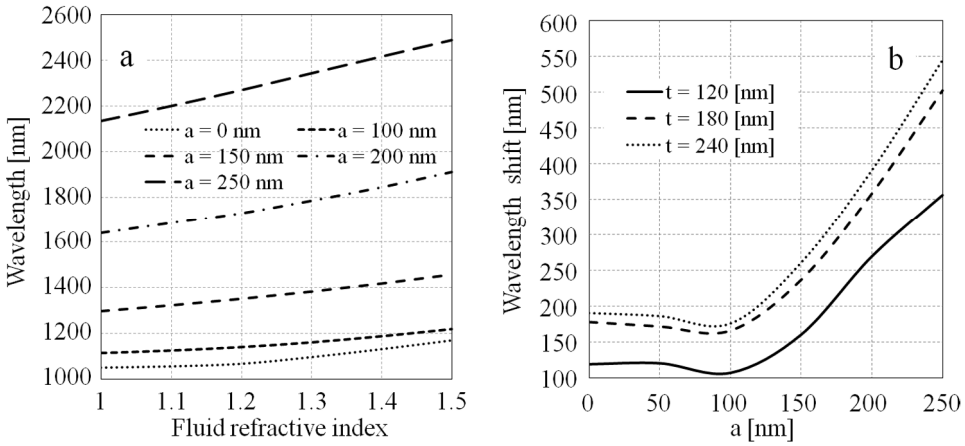

Figure 5.4: (a) Resonant wavelength as a function of fluid refractive index and internal radius of the ring *a*, (b) sensitivity of the device for a refractive index variation Δn from 1 to 1.5.

Figure 5.4(a) shows the resonant wavelength associated with the suppressed transmittance as function of fluid refractive index and inner radius of gold ring. The result illustrates a close-to-linear dependence in agreement with the expectations from lowest-order perturbation theory. As showed in Figure 5.4(b) the wavelength shift increases when the internal radius of the device increases as a larger fluid volume is perturbing the resonance. Along the above discussion, we quantify the fluid-refractive index sensitivity by the dimensionless parameter S_V:

$$S_V = \frac{\Delta\lambda}{\Delta n} \cdot \frac{T^2}{V} \tag{5.4}$$

This is plotted in Figure 5.5(a). The resonance line width is quantified by the Q-factor, which is plotted in Figure 5.5(b). Form the shape of the plots of Figure 5.5 it seems that the structure can be more selective with higher Q-factor but with lower sensitivity with respect to the refractive index as *a* becomes smaller.

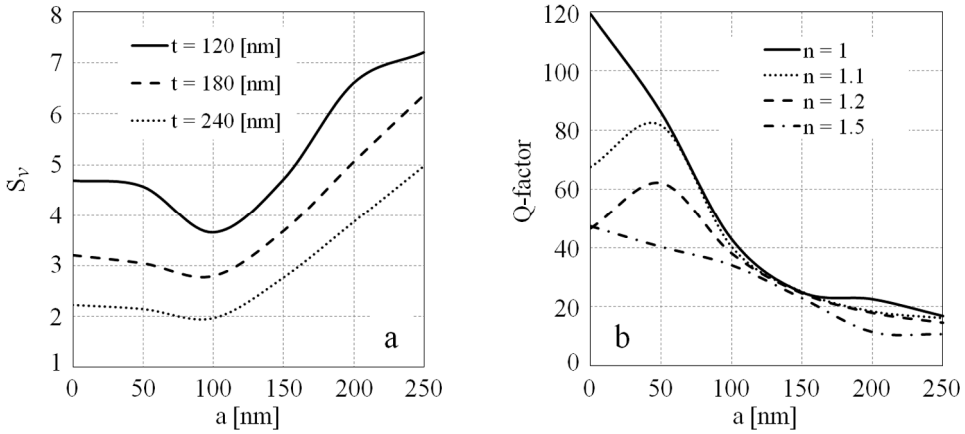

Figure 5.5: (a) sensitivity of the device for refractive index variation Δn from 1 to 1.5 and (b) Q-factor for $h = t = 120$ nm for several values of refractive index.

5.3. Rayleigh anomaly analysis

The presence of a fluid over the substrate allows us to explore the RA in metallic thin-film device, effectively being sandwiched between two different dielectric materials. In the general case, we thus anticipate two independent characteristic wavelengths: one wavelength associated with the SPP supported by the glass/gold interface and another one connected with the fluid/gold interface. The first order of the RA one will obey the relationship mentioned above already.

With a fixed spectral position for a given unit cell size. Along with the same lines, we define also the spectral position λ_{fluid} of the RA related to the interface of the fluid. We consider a particular structure with T = 700 nm, h = 120 nm and Figure 5.6 shows how the two RAs respond quite differently to variations in the fluid-refractive index. Clearly, the RA at 705 nm is blueshifted when fluid-refractive index is increased from n = 1 to 1.2. On the contrary, the RA at 1022 nm, associated with the substrate, is clearly insensitive to the changes in the fluid.

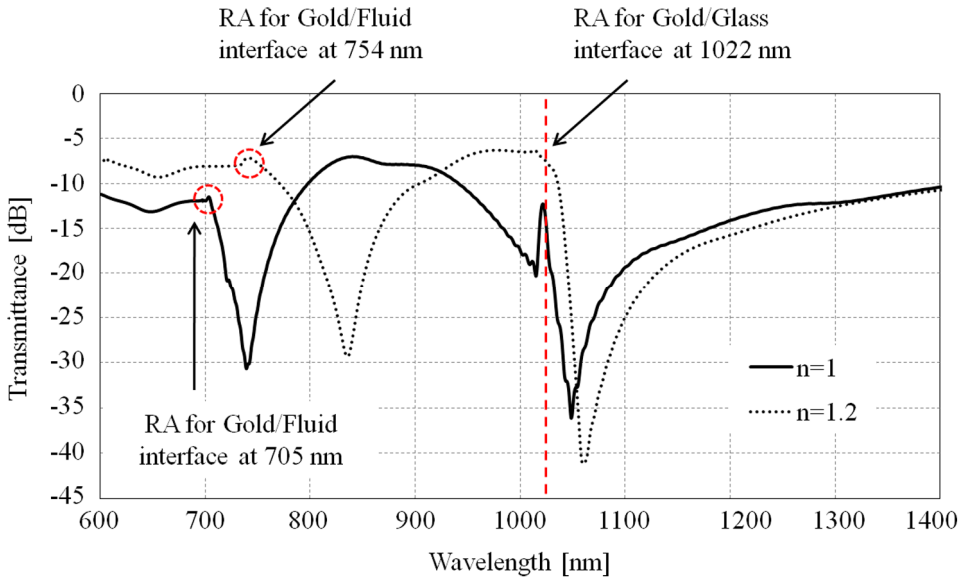

Figure 5.6: Simulated spectra for t = 300 nm, h = 120 nm, a = 0 and T = 700 nm for two values of refractive index. The spectra show a RA for each interface. The RA for Gold/Fluid interface shifts as the refractive of the fluid changes. The RA for Gold/Glass interface does not depend by the fluid refractive index.

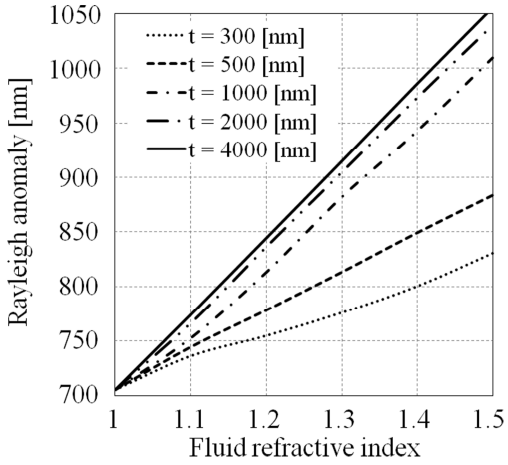

Figure 5.7: Variation of the Rayleigh anomaly for the gold/fluid interface for several value of t.

Figure 5.7 summarizes the results for the shift in the RA for several values for the fluid thickness. As a most interesting result, we see how the RA also depends on the volume of the fluid up to a certain level were the thickness t exceeds the decay length associated with exponential decay of the surface plasmon field intensity away from the interface. The RA will thus in general shift if the thickness of a given fluid is increased, even though the fluid-refractive index remains unchanged.

5.4. Conclusion

The geometrical properties of the rings influence both the suppressed wavelength and the Q-factor. The Q-factor increases when the internal radius decreases with the full metallic disc being the optimal choice if only focusing on the Q-factor. The increase of the metallic film thickness is beneficial for both the Q-factor and for lowering the geometrical sensitivity. Our results show that the RA anomaly associated with the substrate is insensitive to the change in the fluid. The RA anomaly associated with the fluid is linearly blueshifted with fluid refractive index changes. We envisage that the proposed structured thin film may be applied to create mirrors for laser devices and other components for photonic devices. The suppressed transmission results in enhanced absorption, which is potentially interesting in the context of energy harvesting for solar cells and photo catalysis. The variation of the spectral response with the isotropic fluid allows us to consider the proposed structure in the field of optofluidic sensors.

Bibliography

1 M. Papuchon, Y. Combemale, X. Mathieu, D. B. Ostrowsky, L. Reiber, A. M. Roy, B. Sejourne, and M. Werner, *Appl. Phys. Lett.* **27**, 289 - 291 (1975).

2 http://www.intel.com/pressroom/archive/releases/2006/20060918corp.htm

3 D. G. Rabus, Integrated Ring Resonators: The Compendium (Springer, Berlin, 2007).

4 C. Fabry, and A. Perot, *Ann. Chim. Phys.* **16**, 115 (1899).

5 C. Desem, and P. L. Chu, *IEE Proc.* **134**, 145 (1987).

6 C. Desem, and P. L. Chu, *Opt. Lett.* **11**, 248 (1986).

7 K. J. Blow, and D. Wood, *Opt. Commun.* **58**, 349 (1986).

8 A. I. Maimistov, and Y. M. Sklyarov, *Sov. J. Quantum Electron.* **17**, 500 (1987).

9 A. S. Gouveia-Neto, A. S. L. Gomes, and J. R. Taylor, *Opt. Commun.* **64**, 383 (1987).

10 K. Iwatsuki, A. Takada, and M. Saruwatari, *Electron. Lett.* **24**, 1572 (1988).

11 K. Iwatsuki, A. Takada, S. Nishi, and M. Saruwatari, *Electron. Lett.* **25**, 1003 (1989)

12 A. Yariv, *IEEE Photon. Technol. Lett.* **14**, 483–485 (2002).

13 P. Phongsanam, C. Teeka, S. Mitatha, and P. P. Yupapin, *Opt. and Photon. Lett.* **4,** 17–24 (2011).

14 W. J. Wan, S. Honkanen, S. I. Najafi and A. Tervonen, *Electron. Letters*, **28**, 21 (1992).

15 T. Ling, S. Chen, and L.J. Guo, *Opt. Express*, **19**, 2 (2011).

16 C. Lerma Arce, K. De Vos, T. Claes, K. Komorowska, D. Van Thourhout, and P. Bienstman, *IEEE Photon. Technol. Lett.* 23, 13 (2011).

17 P. P. Absil, J. V. Hryniewicz, B. E. Little, P. S. Cho, R. A. Wilson, L. G. Joneckis, P. T. Ho, *Opt. Lett.* **25**, 8 (2000).

18 M. Hamacher, U. Troppenz, H. Heidrich, and D. G. Rabus, Proc. SPIE, 4947, 212-222 (2002).

19 I. Christiaens, D. Van Thourhout, and R. Baets, *16th IPRM*, **40**, 9 (2004).

20 L. J. Kauppinen, S. Abdulla, M. Dijkstra, M. J. de Boer, E. Berenschot, G. J. M. Krijnen, M. Pollnau, and R. M. de Ridder, *Opt. Lett.* **36**, 7 (2011).

21 W. De Cort, J. Beeckman, R. James, F. A. Fernandez, R. Baets, and K. Neyts, *J. Opt. Soc. Am. B*, **28**, 1 (2011).

22 Y. H. Wen, O. Kuzucu, T. Hou, M. Lipson, and A. L. Gaeta, *Opt. Lett*, **36**, 8 (2011).

23 A. Yariv, and M. Nakamura, *IEEE J. Quantum Electron.* **13**, 4, 233–253 (1977).

24 E. A. Swanson, and S. R. Chinn, *IEEE Photon. Technol. Lett.* **7**, 114 (1995).

25 G. Jeong, J. H. Lee, M. Y. Park, C. Y. Kim, S. H. Cho, W. Lee, and B. W. Kim, *IEEE Photon. Technol. Lett.* **18**, 2102–2104 (2006).

26 Y. O. Noh, H. J. Lee, J. J. Ju, M. S. Kim, S. H. Oh, and M. C. Oh, *Opt. Express* **16**, 18194–18201 (2008).

27 M. Kumar, T. Sakaguchi, and F. Koyama, *Appl. Phys. Lett.* **94**, 061112 (2009).

28 R. G. DeCorby, N. Ponnampalam, E. Epp, T. Allen, and J. N. McMullin, *Opt. Express* **17**, 16632–16645 (2009).

29 J. Brouckaert, W. Bogaerts, S. Selvaraja, P. Dumon, R. Baets, and D. Van Thourhout, *Photon. Technol. Lett.* **20**, 309–311 (2008).

30 T. Jalkanen, V. Torres-Costa, J. Salonen, M. Bjorkqvist, E. Makila, J. M. Martinez-Duart, and V. P. Lehto, *Opt. Express* **17**, 5446–5456 (2009).

31 V. Maselli, J. R. Grenier, S. Ho, and P. R. Herman, *Opt. Express* **17**, 11719–11729 (2009).

32 T. E. Murphy, J. T. Hastings, and H. I. Smith, *J. Lightwave Technol.* **19**, 1938–1942 (2001).

33 K. J. Kim, J. K. Seo, and M. C. Oh, *Opt. Express* **16**, 1423–1430 (2008).

34 F. Tian, C. Harizi, H. Herrmann, V. Reimann, R. Ricken, U. Rust, W. Sohler, F. Wehrmann, and S. Westenhofer, *J. Lightwave Technol.* **12**, 1192–1197 (1994).

35 A. Hosseini, and Y. Massoud, *Opt. Express* **14**, 11318–11323 (2009).

36 X. Z. Lin, Y. Zhang, H. L. An, and H.-D. Liu, *Electron. Lett.* **30**, 887–888 (1994).

37 L. Sirleto, G. Coppola, G. Breglio, G. Abbate, G. C. Righini, and M. J. Oton, *Opt. Eng.* **41**, 2890–2898 (2002).

38 F. R. M. Adikan, J. C. Gates, A. Dyadyusha, H. E. Major, C. B. E. Gawith, I. J. G. Sparrow, G. D. Emmerson, M. Kaczmarek, and P. G. R. Smith, *Opt. Lett.* **32**, 1542–1544 (2007).

39 G. Assanto, *J. Mod. Opt.* **37**, 855–863 (1990).

40 S. Honda, Z.Wu, J. Matsui, K. Utaka, T. Edura, M. Tokuda, K. Tsuitsui, and Y. Wada, *Electron. Lett.* **43**, 630– 631

(2007).
41 C. S. Goh, M. R. Mokhtar, S. A. Butler, S. Y. Set, K. Kikuchi, and M. Ibsen, *IEEE Photon. Technol. Lett.* **15**, 557–559 (2003).
42 M. Kumar, T. Sakaguchi, and F. Koyama, *Opt. Lett.* **34**, 1252–1254 (2009).
43 D. Psaltis, S. R. Quake, C. Yang, *Nature* **442**, 27 (2010).
44 D. Erickson, *Microfluid Nanofluid*, **4**, 1-2 (2008).
45 X. C. Li, J. Wu, A. Q. Liu, Z. G. Li, Y. C. Soew, H. J.Huang, K. Xu, and J. T. Lin JT, *Appl. Phys. Lett.* **93** 193901 (2008).
46 D. Sinton D, G. R. Reuven, and A. G. Brolo, *Microfluid Nanofluid*, **4**, 107–116 (2008).
47 W. Chiena, M. Z. Khalida, X. D. Hoab, and A.G Kirka, *Sens. Actuator B.* **138**, 441–445 (2009).
48 Z. Wang, J. Heflin, R. Stolen, and S. Ramachandran, *Appl. Phys. Lett.* **86** 223104 (2005).
49 D. Brennan, P. Lambkin, and P. Galvin, *Meas. Sci. Technol.* **19**, 085403 1–7 (2008).
50 W. Song, X Zhang, A. Liu, C. Lim, P. Yap, and H. Hosseini *Appl. Phys. Lett.* **89**, 203901 (2006).
51 G. Testa, Y Huang, P. M. Sarro, L. Zeni, and R. Bernini, *Opt. Lett.* **35**, 1584-1586 (2010).
52 C. Chao, and L. Guo, *Appl. Phys. Lett.* **83**, 1527-1529 (2003).
53 E. Krioukov, D. Klunder, A Driessen, J. Greve, and C. Otto, *Opt. Lett.* **27**, 512-514 (2002).
54 A. Savchenkov, A. Matsko, M. Mohageg, and L. Maleki, *Opt. Lett.* **32**, 497-499, (2007).
55 M. Ferrara, D. Duchesne, L. Razzari, M. Peccianti, R. Morandotti, P. Cheben , S. Janz, D. Xu, B. Little, S. Chu, and D. Moss, *Opt. Express* **17**, 14098-14103 (2009).
56 H. Li, and X. Fan, *Appl. Phys. Lett* **97**, 011105 (2010).
57 D. K. Armani, T. Kippenberg, S. Spillane, and K. Vahala, *Nature* **421**, 925-928 (2003).
58 A. A. Savchenkov, A. Matsko, V. S. Ilchenko, and L. Maleki, *Opt Express.* **15**, 6768-6773 (2007).
59 Y. Panitchob Y, G. Murugan, M. Zervas, P. Horak, S. Berneschi, S. Pelli, G. Nunzi Conti, and J. Wilkinson, *Opt. Express.* **16**, 11066-11076 (2008).
60 G. Gilardi, D. Donisi, A. Serpengüzel, and R. Beccherelli, *Opt. Lett.* **34**, 3253-3255 (2009).
61 N. J. Harrick, Internal Reflection Spectroscopy, John Wiley and Sons - New York (1967).
62 M. L. Gorodetsky, A. A. Savchenkov, and V. S. Ilchenko, *Opt. Lett.* **21**, 453–455 (1966).
63 F. Vollmer and S. Arnold, *Nat. Methods*, **5**, 591-596 (2008).
64 J. Homola, I. Koudela and S. S. Yee, *Sens. Actuators B.* **54**, 16–24 (1999).
65 A. J. Haes, S. L. Zou, G. C. Schatz, and R. P. Van Duyne, *J. Phys. Chem. B*, **108**, 109–116, (2004).
66 tunable laser con LC
67 A. Sneh, and K. M. Johnson, *J. Lightwave Technol.* **14**, 1067-1080 (1996).
68 D. Vettese, *Nature Photonics*, **4**, 752–754 (2010).
69 A. d'Alessandro, and R. Asquini, *Mol. Cryst. Liq. Cryst.* **398**, 207-221, (2003).
70 W. A. Crossland, I. G. Manolis, M. M. Redmond, K. L. Tan, T. D. Wilkinson, M. J. Holmes, T. R. Parker, H. H. Chu, J. Croucher, V. A. Handerek, S. T. Warr, B. Robertson, I. G. Bonas, R. Franklin, C. Stace, H. J. White, R. A. Woolley, and G. Henshall, *J. Lightwave Technol.* **18**, 1845-1854 (2000).
71 I. C. Khoo, and J. Ding, A*ppl. Phys. Lett.* **81**, 2496-2498 (2002).
72 T. G. Giallorenzi, J. A. Weiss, and J. P. Sheridan, *J. Appl. Phys.* **47**, 1820-1826 (1976).
73 M. Schadt, H. Seiberle, and A. Schuster, *Nature*, **381**, 212-215 (1996).
74 C. P. Chang, MEMS for telecommunications: devices and reliability Custom Integrated Circuits *IEEE Conference, Proc.* 199-206, (2003).
75 F. C. Frank, *Discuss. Faraday Soc.* **25**, 19 (1958).
76 Lien A. *Liquid Cryst.* **22**, 171, (1977).
77 www.merck.com
78 J. Li, S. Wu, S. Brugioni, R. Meucci, and S. Faetti, *J. Appl. Phys.* 97, 073501 1-5 (2005).
79 Y. Zhao, T. Ikeda, Smart Light-Responsive Materials: Azobenzene-Containing Polymers and Liquid Crystal,Wiley (2009).
80 F. Simoni, and O. Francescangeli, *J. Phys. Condens. Matter* **11**, 439-487 (1999).
81 E. Sackmann, *J. Am. Chem. Soc*, ***93***, 7088–7090 (1971).
82 C.-R. Lee, T.-L. Fu, K.-T. Cheng, T.-S. Mo, and A. Y.-G. Fuh, *Phys. Rev. E* **69**, 031704 (2004).

83 L. De Sio, A. Veltri,C.Umeton, S.Serak, and N. Tabiryan, *Appl. Phys. Lett.* **93**, 181115 (2008).
84 T. Ikedaa, T. Miyamotoa, S. Kuriharaa, and S. Tazukea, *Mol. Cryst. Liq. Cryst.* **188**, 223-233 (1990).
85 Lord Rayleigh, *Scientific Papers* (Cambridge U. Press) **5**, 617–620 (1912).
86 A. Ashkin, and J. M. Dziedzic, *Appl. Opt.* **20**, 1803 (1981).
87 C. G. B. Garrett, W. Kaiser, and W. L. Bond, *Phys. Rev.* **124**, 1807–1809 (1961).
88 J. Heebner, R. Grover, and T. Ibrahim, Optical Microresonators, Springer, London, (2007).
89 J. Stratton *et al.*, "Elliptic cylinder and spheroidal wave functions including tables of separation constants and coefficients", Wiley, New York, (1941).
90 S. V. Boriskina, P. Sewell, T. M. Benson, and A. I.Nosich, *J. Opt. Soc. Amer. B* **21**, 393–402, (2004).
91 L. G. Guimaraes and H. M. Nussenzveig, *Opt. Commun.*, **89**, 363–369, (1992).
92 B. R. Johnson, *J. Opt. Soc. Amer. A* **10**, 343– 352, (1993).
93 I. Teraoka, S. Arnold, and F. Vollmer, *J. Opt. Soc. Amer. B* **20**, 1937–1946, (2003).
94 A. B. Matsko, and V. S. Ilchenko, *IEEE Journal of selected topics in quantum electronics*, **12**, 1, (2006).
95 M.L. Gorodetsky, and V.S. Ilchenko, *Opt. Commun.* **113**, 133-143 (1994).
96 J. Cardin, and D. Leduc, *Appl. Opt* **47**, 7, 1337-1350, (1970).
97 M. Cai, O. Painter, and K. J. Vahala, *Phys Rev. Lett.* **8**, 74 -77, (2000).
98 S. M. Spillane, T. J. Kippenberg, O. J. Painter, and K. J. Vahala, *Phys. Rev. Lett.* **91**, 043-902 (2003).
99 I .Ilchenko, X. S. Yao, and L. Maleki, *Opt. Lett.* **24**, 723 (1999).
100 Y. Panitchob, G. Senthil Murugan, M.N. Zervas, P. Horak, S. berneschi, S. Pelli, G. Nunzi Conti, and J. S. Wilkinson, *Opt. Express* **16**, 11066 (2008).
101 S. C. Hill, and R. E. Benner, *J. Opt. Amer. Soc. B*, **3**, 1509–1514 (1986).
102 A. A Savchenkov, A. B. Matsko, V. S. Ilchenko, and L. Maleki, *Opt Express* **15**, 6768-6773 (2007).
103 M. L. Gorodetsky, A. A. Savchenkov, and V. S. Ilchenko, *Opt. Lett.* **21**, 453– 455, (1996).
104 P. Chylek, H. B. Lin, J. D. Eversole, and A. Campillo, *Opt. Lett.* **16**, 1723–1725 (1991).
105 S. Arnold, and L. M. Folan, *Opt. Lett.* **14**, 387–389 (1989).
106 S. Schiller, I. I. Yu, M. M. Fejer, and R. L. Byer, *Opt. Lett.* **17**, 140–142, (1992).
107 M. Ferrara, D. Duchesne, L Razzari, M. Peccianti, R. Morandotti, P. Cheben, S. Janz, D. X. Xu, B. E. Little, S. Chu, and D. J. Moss, *Opt. Express* **17**, 14098-14103 (2009).
108 D. K. Armani, T. J. Kippenberg, S. M. Spillane, K. J. *Nature* **421**, 925-928 (2003).
109 T. Ioppolo, and M. V. Ötügen, **24**, 10, *J. Opt. Soc. Am. B* (2007).
110 Q. Ma, T. Rossmann, and Z. Guo, *Meas. Sci. Technol.* **21** 025310 (2010).
111 Q. Ma, T. Rossmann, and Z. Guo, *J. Phys. D. Appl. Phys.* **41**, 245111 (2008).
112 T. Ioppolo, U. Ayaz1, and M.Ötügen, *Opt. Express*, **17**, 19, 16465- 16479 (2009).
113 G. Gilardi, D. Donisi, A. Serpenguezel, and R. Beccherelli, *Opt. Lett.*, **34**, 21, 3253-3255 (2009).
114 Y. Panitchob, G. Senthil Murugan, M. N. Zervas, P. Horak, S. Berneschi, S. Pelli, G. Nunzi Conti, and J. S. Wilkinson, *Opt. Express*, 16, 15, 11066-11076 (2008).
115 R. V. Ramaswamy, and Srivastava, *J. Lightwave Technol*, **6**, 6 (1988).
116 L. Ross, N. Fabricius, and H. Oeste, presentated at Euro Fiber Optic. Conf. Lan 87, Basel, Switzerland, (1987).
117 http://www. ispoptics.com
118 http://www.mellesgriot.com
119 P. L. Auger, S. I. Najafi, *Appl. Opt.* **33**, 16, pp. 3333-3337 (1994**).**
120 R. G. Walker, C. D. W. Wilkinson, *Appl. Opt.* **22**, pp. 1923-1928, (1983).
121 J. Zou, F. Zhao, and R. T. Chen, *Appl. Opt.* **41**, 7620-7626 (2002).
122 A.Tervonen, and S. Honkanen, *Appl. Opt.* **35**, 6435-6437 (1996).
123 http://www.dowcorning.com/applications/search/default.aspx?r=131en
124 Yung-Pin Chen, Yuet-Ping Lee, Jer-Haur Chang, and Lon A. Wang, *J. Vac. Sci. Technol. B* **26**, 1690 (2008).
125 http://www.microchem.com/pdf/SU-82000DataSheet2000_5thru2015Ver4.pdf
126 A. M. Jalal, G. I. Sergey, B. Ridha, and P. Sullivan, *J. Microelectromech. Syst.* **19**, 110-119 (2010).
127 J. M. Ng, I. Gitlin, A. D. Stroock, and G. M. Whitesides, *Electrophoresis* **23**, 3461-3473 (2002).
128 J. Zhou, A. V. Ellis, and N. H. Voelcker, *Electrophoresis* **31**, 2-16 (2010).
129 G. M. Whitesides, E. Ostuni, S. Takayama, X. Jiang, and D. E. Ingber, *Annu. Rev. Biomed. Eng.* **3**, 335–373

(2001).
130 I. Teroka, and A. Arnold, *J. Opt. Soc. Am. B.* **23**, 1434-1441 (2006).
131 C. Y. Chao, and L. J. Guo, *J. Lightwave Technol.* **24**, 1395-1402 (2006).
132 N. M. Hanumegowda, C. J. Stica, B. C. Patel, I. White, and X.Fan, *Appl. Phys. Lett.* **87**, 201107 (2005).
133 L. J. Kauppinen, H. J. W. M. Hoekstra, R. M. de Ridder, *Sens. Act. B* **139**, 194 (2009).
134 Xu F, Horak P, and Brambilla G, *Opt. Express* **15**, 7888-7983 (2007).
135 D. Donisi, L. De Sio, R. Beccherelli, M. A. Caponero, A. d'Alessandro, and C. Umeton, *Appl. Phys. Lett.* **98**, 151103 (2011).
136 R. Osellame, R. Ramponi, M. Marangoni, G. Tartarini, and P. Bassi, *Appl. Phys. B* **7**3, 505–509 (2001).
137 G. Jeong, J. H. Lee, M. Y. Park, C. Y. Kim, S. H. Cho, W. Lee, and B. W. Kim, *IEEE Photon. Technol. Lett.* **18**, 2102–2104 (2006).
138 J. Brouckaert, W. Bogaerts, P. Dumon, R. Baets, and D. Van Thourhout, *Photon. Technol. Lett.* **20**, 309–311 (2008).
139 M. Kumar, T. Sakaguchi, and F. Koyama, *Appl. Phys. Lett.* **94**, 061112 (2009).
140 G. Gilardi, R. Asquini, A. d'Alessandro, and G. Assanto, *Opt. Express* **18**, 11524–11529 (2010).
141 J. E. Ehrlich, G. Assanto, and G. I. Stegeman, *Appl. Phys. Lett.* **56**, 602–604 (1990).
142 N. Tabiryan, U. Hrozhyk and S. Serak, *Phys. Rev. Lett.* **93**, 113901-113904 (2004).
143 U. A. Hrozhyk1, S. V. Serak, N. Tabiryan1, L. Hoke, and B. R. Kimball, *Opt. Express* **18**, 8697- 8704 (2010).
144 R. Caputo, L. De Sio, A. Veltri, C. Umeton, and A. V. Sukhov, *Opt. Lett.* **29**, 1261-1263 (2004).
145 R. Caputo, A. Veltri, C. P. Umeton, and A. Sukov, *J. Opt. Soc. Am. B.* **21**, 1939-1947 (2004).
146 L. De Sio, S. Serak, N. Tabiryan, S. Ferjani, A. Veltri, and C. Umeton, *Adv. Mater.* **22**, 2316-2319 (2010).
147 L. De Sio - Ph.d dissertation: "Periodic structures in composite materials for photonics applications" (1996).
148 L. De Sio, S. Ferjani, G. Strangi, C. Umeton, and R. Bartolino, *Soft Matter* **7**, 3739-3743 (2011).
149 L. De Sio, S. Serak, N. Tabiryan, and C. Umeton, *J. Mater. Chem.* **21**, 6811-6814 (2011).
150 A. d'Alessandro, D. Donisi, L. De Sio, R. Beccherelli, R. Asquini, R. Caputo, and Cesare Umeton, *Opt. Express* **16**, 9254 – 9269 (2008).
151 https://www.norlandprod.com/adhesives/NOA%2061.html
152 J. Li, S. Gauza, and S. Wu, *J. Appl. Phys.* **96**, 19-24 (2004).
153 http://www.rsoftdesign.com
154 G. Ghosh, *Appl. Opt.* **36**, 1540-1546 (1997).
155 I. C. Khoo, Liquid Crystals (Second Edition) *John Wiley & Sons* (2007).
156 T.W.Ebbsen, H. J. Lezec, H. F. Ghaemi, T. Thio, and P. A. Wolff, *Nature*, **391**, 667-669 (1998).
157 J. A. Porto, F. J. Garcia-Vidal, and P.B. Pendry, *Phys. Rev. Lett.* **83** (14) 2845-2848 (1999).
158 I. S. Spevak, A. Y. Nikitin, E. V. Bezuglyi, A. Levchenko, and A. V. Kats, *Phys. Rev.* B **79**, 161406 (2009).
159 J. Valentine, S. Zhang, T. Zentgraf, E. Ulin-Avila, D. A. Genov, G. Bartal, and X. Zhang, *Nature* **455**, 376 (2008).
160 D. Pacifici, H. J. Lezec, and H. A. Atwater, *Nature Photon.* **1**, 402-406 (2007).
161 M. E. Stewart, C. R. Anderton, L. B. Thompson, J. Maria, S. K. Gray, J. A. Rogers, and R. G. Nuzzo, *Chem. Rev.* **108**, 494-521 (2008).
162 R. Gordon, D. Sinton, K. L. Kavanagh, and A. G. Brolo, *Accts. Chem. Res.* **41**, 1049-1057 (2008).
163 S. Xiao, J. Zhang, L. Peng, C. Jeppesen, R. Malureanu, A. Kristensen and N. A. Mortensen, *Appl. Phys. Lett.* **97**, 071116 (2010).
164 S. Xiao, and N. A. Mortensen, *Opt. Lett.*, **36**, 1, 37-39 (2011).
165 P. S. Pedersen, P. S. Nunes, S. Xiao, and N. A. Mortensen, *Sensors*, **9**, 8382-8390 (2009).